Ligne InterFaces

I. INTRODUCTION

La ligne CRG-Interfaces (IF) a fonctionné normalement tout au long de l'année 2009, et ce dès le redémarrage, du fait d'une réalisation plus rapide que prévu de l'agrandissement de la cabane SUV. En terme d'utilisation de temps de faisceau, l'impact de ces travaux sur l'utilisation de la ligne est nul puisque 22 expériences ont été faite. La répartition du temps de faisceau par contre a été de 60% sur le Goniomètre Multitechnique, réparti pour moitié sur l'installation de microdiffraction, et 40% sur l'instrument SUV. En plus de ces expériences nous avons pu distribuer du temps de faisceau aux équipes locales pour soutenir les programmes de recherche impliquant des thésards.

Les publications listées en fin de ce rapport pour les trois dernières années montrent la qualité des recherches conduites sur la ligne. Une quinzaine d'articles ont été publiés dans des revues de rang A en 2009, dont un Surface Science Report (facteur d'impact 12,8) , 1 Phys. Rev. Lett. (7,2), 3 Appl. Phys. Lett. (3,7), 3 Phys. Rev B (3,32). En 2008, une quinzaine d'articles avaient été publiés, dont une Science (28,1), 2 Phys. Rev. Lett. (7,2), 2 Apl. Phys. Lett. (3.73) et 4 Phys. Rev. B. En 2007, une vingtaine d'articles avaient été publiés dans des revues de rang A, dont un Nano Letters (facteur d'impact 10), 1 Langmuir (4), 1 Appl. Phys. Lett. (3,6), 8 Phys. Rev. B (3,17), 1 J. Appl. Phys. (2,3), 4 Surf. Sci. (1,9) . Plusieurs thèses ont été soutenues, et 2 chapitres de livre publiés.****

Pour l'année à venir, le projet majeur reste l'implémentation de la croissance en phase chimique (UHV-CVD ou CBE) sur l'instrument SUV, couplée à l'agrandissement de la cabane expérimentale réalisé cette année. Le système d'injection de gaz a été commandé, et devrait être installé début 2010.

Tobias Schülli, embauché il y a trois ans au CEA pour développer ce projet, va partir à l'ESRF au 1er décembre 2009 pour prendre la responsabilité de la ligne ID01. Afin de conduire ce programme tout en continuant d'assurer le rôle de « local contact » sur l'instrument, il est indispensable de remplacer Tobias Schülli, par exemple par un post-doc récurrent.

En outre, si un technicien a pu être embauché en CDD au CEA pour un an sur l'instrument SUV, il serait très souhaitable de transformer son contrat en CDI, assurant ainsi la permanence du support technique.

Nous présentons d'abord les développements instrumentaux, puis l'activité sur les instruments Goniomètre Multitechnique, GMT, suivi de l'instrument de surfaces/croissance de nanostructures en ultra-vide, SUV, ainsi qu'une compilation des publications.

II. Développements instrumentaux

II.1. Optimisation du 1er cristal monochromateur et monochromateur Germanium collé

Les travaux sur les cristaux monochromateur sont toujours en cours. La société ACCEL est toujours en attente d'une première commande d'un monochromataur à double cristaux incluant notre premier cristal. Il est convenu avec eux qu'un accord de licence sera fait s'il y a une commande ferme.

Les cristaux en Germanium collés sur Silicium ne sont pas encore testés dans un monochromateur. Le collage du bloc de Ge au poli optique sur un bloc de Si est validé ainsi qu'une procédure de découpe par électro-érosion du Si dopé. Cette technique nous offre un procédé alternatif à l'usinage mécanique des cristaux de Si. Pour le système de test nous utiliserons encore l'usinage standard pour usiner le premier et second cristaux du monochromateur.

II.2. Détecteurs

La caméra CCD utilisées pour toutes les expériences de GISAXS tant sur SUV que sur GMT a maintenant 8 ans et présente des signes de faiblesse. Le phosphore faisant la conversion X visible s'est décollé du réseau de fibres optique démagnificateur et a dû être réparé à plusieurs reprises. D'autre part l'électronique est obsolète et une panne sur un des modules ne pourrait être réparée. C'est pour cela que nous avons établi le cahier des charges d'un système pouvant remplacer avantageusement cette caméra, et permettrait de gagner un facteur 5 dans les durées d'acquisitions pour un rapport signal sur bruit amélioré.

De même pour remplacer les électromètres utilisés pour lire les diodes servant de moniteur de faisceau à différents endroit de la ligne, nous avons acquis pour des tests un nouveau système développé au synchrotron italien, et permettant la lecture simultanée de 4 voies. L'intégration de cet appareil dans notre système de contrôle commande est faite et il sera utilisé très prochainement pour remplacer les anciens électromètres.

II.3. Agrandissement cabane diffractomètre SUV

L'évolution majeure sur la ligne IF en 2009 est l'agrandissement de la cabane SUV en vue de l'installation début 2010 du système de CBE. Cette transformation à a eu lieu fin 2008 / début 2009 en neutralisant 8 semaines de faisceau pour permettre les opérations de construction de la cabane en plomb, travaux d'infrastructure lourds, incluant les fluides, l'électricité, et nécessitant un démontage complet du diffractomètre SUV et de sa chambre ultravide afin de libérer l'espace durant les travaux.

Le planning de l'intervention a été parfaitement maîtrisé, avec même une anticipation de la date de fin et une reprise effective du faisceau mi-Janvier sur les deux autres instruments de la ligne; GMT et la microdiffraction. Parallèlement, nous avons poursuivi l'opération de remontage de l'instrument SUV, pour une reprise du faisceau sur cet appareil à partir de fin mars 2009. Ce remontage a été l'occasion d'une remise à plat de l'ensemble de contrôle commande de cet instrument.

L'installation de la caméra CCD utilisée pour les expériences en GISAXS a pu être faite en éloignant le détecteur pour gagner en résolution.

Finalement conformément aux prévisions le faisceau a pu être remis sur l'instrument SUV à partir de fin mars 2009.

Au cours de l'année, lors d'arrêts courts, et sans rogner sur le temps de faisceau les derniers aménagements pour accueillir l'installation CBE ont été faits. Il s'agit principalement de l'installation d'un système d'extraction spécifique pour cette installation, rejetant les effluents directement à l'extérieur du hall expérimental par une canalisation spécifique, avec système d'extraction dédié, et contrôle des débuts volumiques, et sécurité.

Les deux autres projets en cours sur cet instrument et présentés dans le rapport 2008 n'ont pas avancé de manière significative faute de moyens en personnel. Il reste à faire quelques câblages électriques sur la tête porte échantillon et à tester les précisions et les reproductibilités des mouvements. Les micro-fentes de précision sont aussi en cours de câblage et là aussi nous devons faire la métrologie pour valider les ensembles mécanique et l'électronique de pilotage. Nous espérons que la présence depuis mi-septembre d'un technicien pour un CDD d'un an nous permettra de mener ces projets à terme en 2010.

II.4. Développements microdiffraction

Les développements techniques pour cet instrument ont porté sur la spécification des nouveaux miroirs focalisant à courbure fixe permettant une taille de faisceau plus petite de 400x200nm pour une densité de flux augmentée d'un facteur 10. Ces miroirs sont commandés ils seront livrés en septembre 2010. Nous attendons les plans de l'interface pour lancer l'étude des supports optimisés pour réduire la sensibilité aux vibrations extérieures.

Parallèlement nous avons défini les nouveaux détecteurs, rédigé les cahiers des charges, faits les appels d'offre et passé les commandes sur le budget ANR MiDiFaBl. La livraison est prévue pour la fin de l'année. Des premières campagnes de mesures, il est apparu clairement que nous avions deux problématiques bien différentes demandant des réponses spécifiques en termes de détecteurs. Soit il s'agit de mesurer de très faibles signaux demandant des temps de pause relativement longs de l'ordre de la dizaine de secondes, soit de mesurer des signaux de diffraction très forts saturant le détecteur en 1 à 2 secondes. Actuellement le détecteur que nous utilisons présente un temps de lecture de 2.5 s auquel il faut rajouter un temps de post-traitement (background, flat-field, correction géométrique) ramenant un temps mort d'environ 5 s. Pour des pauses courtes ceci devient le facteur limitant rallongeant inutilement les durées d'acquisition. C'est pour cela que nous avons choisi d'acquérir 2 détecteurs complémentaires, qui permettront de faire le meilleur compromis entre sensibilité et temps d'acquisition. De plus le détecteur rapide possède un système évitant que la saturation du signal dans un pixel ne se propage sur les pixels voisins. Actuellement des cartographies de l'échantillon de 25x25µm au pas de 0.5µm en pausant 2s par point prennent 5h. Avec le nouveau détecteur rapide nous passerons à 40min, et avec celui ayant une meilleure sensibilité nous passerons à 3h. Ces 2 détecteurs seront livrés en fin d'année. Leur mise en place avec le développement logiciel requis sera faite début 2010.

III Goniomètre Multi-Techniques (GMT)

III.1. Introduction

La station GMT abrite, outre les expériences « traditionnelles » de diffraction réalisées à l'aide du goniomètre multitechnique, les expériences de microdiffraction. Le personnel intervenant sur ces expériences comprend un ingénieur de recherche CNRS (J.S. Micha) ainsi que des ingénieurs-chercheurs CEA (F. Rieutord (responsable), O. Robach, O. Ulrich, X. Biquard). Ils accueillent les utilisateurs et assurent le fonctionnement, la maintenance et le développement des instruments. L'instrument reçoit fréquemment les étudiants de Master 2 et d'Hercules pour des travaux pratiques de réflectivité, diffraction de surface et micro-diffraction Laue.

Les expériences de « commissioning » (micro-diffraction, optique de ligne, performances monochromateur) utilisent pour des raisons pratiques les moyens instrumentaux de GMT. En outre, la cabane GMT et son équipement accueillent les expériences de micro-diffraction demandant un déplacement et une immobilisation du goniomètre pour laisser place au châssis supportant l'ensemble miroirs focalisants, échantillon et caméra CCD.

Les disciplines scientifiques concernées par les expériences conduites dans la cabane instrumentale sont comme les années précédentes: la matière condensée molle et la matière condensée dure (en majorité). Les trois expériences de matière molle avaient pour objet de 1) comprendre le comportement mécanique générale d'une membrane (T. Charitat *et al.*), 2) étudier la morphologie et la super-structure de films de silicium mésoporeux (S. Dourdain *et al.*) et 3) reconnaitre les phases mis en jeu au cours de cycle électrochimique in situ (S. Peulon *et al.*). Les expériences en matière dure ont employé le *goniomètre multitechnique*: F. Rieutord *et al.* ont étudié les mécanismes d'adhésion et de fragilisation de wafers de silicium collés. M.C. Saint-Lager et al. ont réalisé des expériences de diffusion centrale en incidence rasante (GISAXS) sur dépôts de catalyseurs modèles effectuées in situ dans leur réacteur monté sur le goniomètre. D'autres expériences ont employé la technique de *microdiffraction*, à l'aide de microfaisceaux blancs et/ou monochromatiques. D'une part, des chercheurs spécialistes de la mécanique des matériaux polycristallins et/ou de la métallurgie pratiquent des expériences pour déterminer localement les grandeurs physiques (déformation, orientation, contraintes) permettant d'expliquer, d'un point de vue fondamental, le comportement macroscopique des matériaux (O. Castelnau *et al.* et T. Hoc *et al.*). D'autre part, O. Perroud *et al.* ont étudié les contraintes dans des MEMS dans le but de calibrer les jauges de contraintes employées par les industriels de la microélectronique. P. Gergaud *et al.* ont suivi in situ l'évolution des contraintes lors de l'électromigration des atomes de cuivre dans une ligne 100nm, la plus fine observée à ce jour sur BM32. P. Bleuet, post-doc (ANR MiDiFaBI) sur l'instrument de microdiffraction, *et al.* ont établi les premières étapes vers l'extension de la présente technique à des cartographies 3D.

Grâce à la rapidité d'achèvement des travaux d'extension de la cabane SUV, nous avons pu bénéficier du faisceau dans la cabane GMT pendant plus d'un mois, durant l'aménagement de SUV. Ce temps additionnel a été employé en très grande partie pour l'instrument de microdiffraction pour se préparer à répondre à la forte demande des utilisateurs. En s'appuyant sur des échantillons adaptés à l'optimisation des procédures opératoires (UO2, H. Palancher et al., ZrO2 J. Villanova et al.), nous avons notamment facilité l'emploi du mode monochromatique, permettant de déterminer le tenseur complet des déformation de la maille cristallographique. Ce mode complémentaire a pris une part importante dans les propositions d'expériences des utilisateurs. La transition d'un mode à l'autre prend maintenant moins d'une demi-heure et peut être réalisée par un utilisateur peu initié.

Le développement de l'instrument de microdiffraction bénéficie jusqu'en février 2010 du soutien financier de l'Agence Nationale de la Recherche par l'intermédiaire du projet PNANO de

métrologie/instrumentation MiDiFaBl, alloué aux trois partenaires CEA-INAC, CNRS- Institut Néel et CEA-Institut LETI. Grâce à ce soutien très important, nous avons entrepris différentes actions d'optimisation des performances et d'équipements de cette expérience notamment : achat d'un détecteur 2D haute performance (pixel ou CCD à anti-blooming), achat et réalisation d'équipements annexes (four, mécanique etc…). L'ANR finance également un postdoc sur la thématique dans ce cadre (Pierre Bleuet). Le mode de financement du fonctionnement ultérieur de l'instrument doit être anticipé compte tenu de la quantité d'instrumentations coûteuses et fragiles mises en œuvre sur laquelle repose la microdiffraction.

Nous donnerons à la suite un descriptif d'expériences réalisées avec le goniomètre multitechnique et l'instrument de microdiffraction. Les expériences décrites par la suite correspondent à du temps alloué par le comité français (FR) et international (ESRF).

Un atelier sur la microdiffraction intitulé "Microdiffraction en faisceau blanc : des mesures vers une analyse physique" a été organisé sur deux jours en septembre 2009, avec l'appui financier du GdR MECANO, et l'appui logistique de l'ESRF et du bureau des CRG. Cet atelier s'inscrit dans une démarche de structuration de la communauté des utilisateurs de la station de microdiffraction, de formation des utilisateurs à l'analyse des données, et de développement des outils logiciels pour l'analyse.

L'atelier a rassemblé une quarantaine de participants, dont environ deux tiers avaient déjà utilisé la technique. Il s'articulait autour de deux objectifs :

–préciser les conditions d'application d'une analyse automatisée des données (cartographies), restreinte à une analyse élastique des déformations locales à l'échelle du micron.

–examiner les processus physiques de déformation plastique, et évaluer les méthodes existantes pour extraire de l'information sur les déformations plastiques à partir des formes des pics de diffraction, dans une analyse plus "manuelle" et prospective.

Les présentations sont disponibles sur le site du GdR MECANO.
http://www.im2np.fr/GDR-Mecano/grenoble2009/index.html "

III. 2. Faits marquants sur GMT

Electrochemical and Solid-State Letters, **12** (10) H373-H375 (2009)
1099-0062/2009/12(10)/H373/3/$25.00 © The Electrochemical Society

Mechanism of Thermal Silicon Oxide Direct Wafer Bonding

C. Ventosa,[a] C. Morales,[a] L. Libralesso,[a] F. Fournel,[a] A. M. Papon,[a] D. Lafond,[a] H. Moriceau,[a,*] J. D. Penot,[b] and F. Rieutord[b,z]

[a]*Commissariat à l'Energie Atomique, LETI, Minatec, 38054 Grenoble Cedex 9, France*
[b]*Commissariat à l'Energie Atomique, Institut Nanoscience et Cryogénie, Service de Physique des Matériaux et Microstructures, Nanostructures et Rayonnement Synchrotron, 38054 Grenoble Cedex 9, France*

Thermal silicon oxide-to-oxide bonding was investigated at the nanometer level using X-ray reflectivity, transmission electron microscopy, and infrared absorption spectroscopy. The measurements reveal the stages of the closure mechanism, which are different from standard silicon bonding. Upon annealing, interface water pockets are formed, the contents of which are further dissolved into the oxide, demonstrating that the buried thermal oxide–silicon interface acts as a barrier against water reaction with silicon.
© 2009 The Electrochemical Society. [DOI: 10.1149/1.3193533] All rights reserved.

Manuscript submitted March 31, 2009; revised manuscript received July 11, 2009. Published August 4, 2009.

Direct wafer bonding consists in joining two wafers at room temperature without any adhesive or additional materials, followed by annealing. Despite a wide technological interest, the detailed mechanism of the sealing of such model solids is poorly known due to the lack of experimental tools to investigate a nanometer-wide interface buried under millimeter-thick materials. Yet, the bonding technology is increasingly used in microelectronics, e.g., for silicon-on-insulator mass production, microelectromechanical systems manufacturing, or in three-dimensional level integration. In many cases, it represents an alternative to deposition for building heterostructures with additional capabilities. For most applications, high quality bonding is required, driving many studies on bonding interfaces.[1-4] Water removal has been widely described in the literature through H_2 outgassing due to a low temperature oxidation occurring through the native oxide. We show here that although macroscopically oxide/oxide, silicon/oxide, and silicon/silicon bondings show similar behavior, the interface evolutions at the nanometer scale are entirely different. We used interfacial X-ray reflectivity (XRR),[5] high resolution transmission electron microscopy (HR-TEM), and Fourier transform infrared spectroscopy in multiple internal reflection (FTIR-MIR)[6] to demonstrate our point. The results of similar techniques applied to silicon/silicon or silicon/oxide bonding can be found for comparison in Ref. 7.

The wafers used were 100 mm in diameter (001)-oriented Czochralski-grown Si wafers. HF-etch was first performed on the wafers to remove the native oxide from the surface. Then the oxide films were thermally grown on the Si–H terminated wafers at 800°C in dry O_2 flow. The typical SiO_2 thickness used in this study was 10 nm. Wafers were then cleaned in sulfoperoxide mixture (H_2SO_4,H_2O_2) and rinsed in deionized water. An RCA cleaning treatment was then performed, followed by a deionized water rinse and spin-drying. Finally, hydrophilic wafers were bonded at room temperature in a clean room atmosphere and annealed at various temperatures in the range from room temperature to 400°C for 2 h.

Figure 1 presents the evolutions of (a) bonding interface density and (b) width as a function of the annealing temperature, obtained from XRR analyses. Above 100°C, together with the bonding energy, our data show that the interface density sharply increases corresponding to interface closure. This mechanism of interface sealing in wafer bonding has been described using rough surface adhesion models.[8] The increase in interface density from 100 to 300°C is driven by the formation of siloxane bonds through the reaction

$$\text{Si–OH} + \text{Si–OH} \rightarrow \text{Si–O–Si} + H_2O \quad [1]$$

The formation of the covalent bonds between the two wafers increases the local adhesion energy, and contact points tend to spread, closing the interface in analogy to a ziplock mechanism. Being a reaction product, water concentration is of course important in this mechanism. In silicon bonding, water is eliminated via silicon oxidation after diffusion through the thin native oxide.[7,9] In the thermal oxide case, the evolution is completely different.

This is already evident considering w (width), the second parameter extracted from the XRR experiment. w is the interface width, i.e., the width of the interwafer zone where the two asperity systems overlap (Fig. 1b). We can observe that, contrary to the silicon bonding case where it stayed constant, the width increases from 1 to 4 nm at 300°C. This increase is coincident with the density rise at the interface. Considering then the product $P = w\Delta\rho$, where $\Delta\rho$ is the difference of the bonding interface density with the silicon density (Fig. 1c), this value is quite constant (P represents the total electron deficit at the interface per unit area). Therefore, during sealing, a volume-conservative mechanism is to be considered, where wider unbonded (pockets) zones are created to store water on a reduced surface area (Fig. 2).

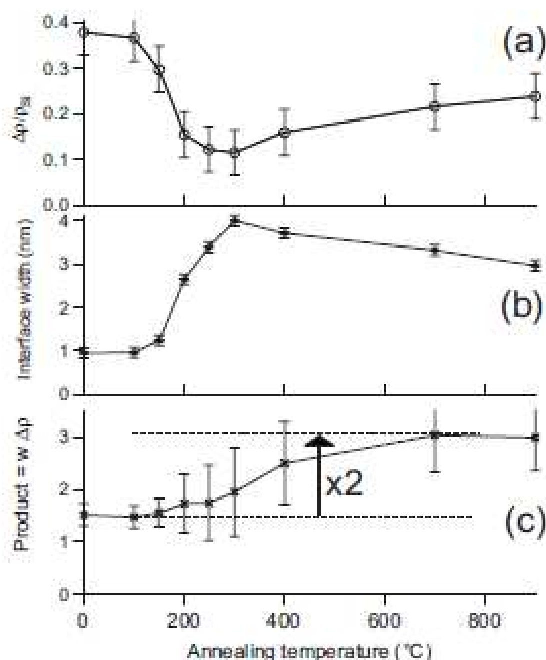

Figure 1. Parameters of the electron density profile obtained from XRR results: (a) Evolution of the bonding interface density $\Delta\rho$, (b) evolution of the bonding interface width w, and (c) P, product of w and $\Delta\rho$, as a function of the postbonding annealing temperature.

* Electrochemical Society Active Member.
z E-mail: francois.rieutord@cea.fr

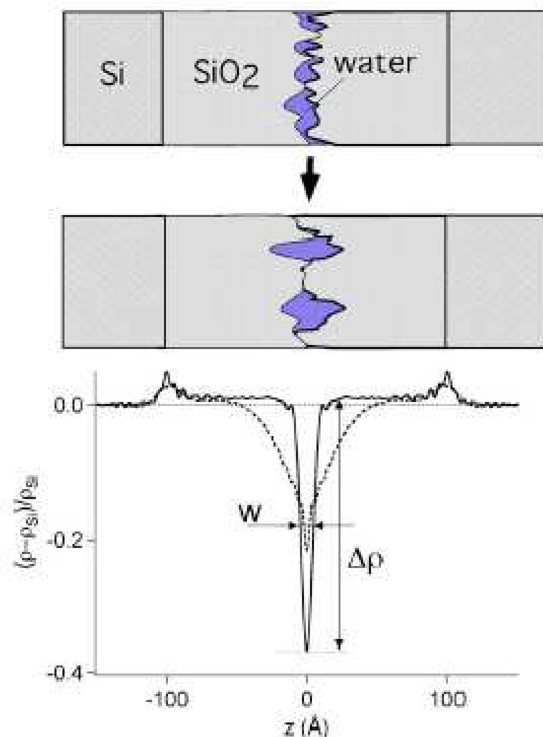

Figure 2. (Color online) Sealing mechanism of the oxide–oxide bonding (top). The electron density profiles are shown on the bottom curve, at room temperature (solid line) and after annealing at 400°C for 2 h (dashed line).

The higher temperature behavior of the interface can be similarly studied. Considering again the *P* value, an increase is visible at $T > 300°C$. The ratio between high and low temperature *P* values is close to 2, a value consistent with the removal of water (the electron density of water is half that of silicon or silicon oxide). One can consider that water leaves the 4 nm high pockets, diffusing into the oxide. The driving forces for this diffusion are the water concentration gradient and the possibility for water to hydrolyze siloxane bonds according to the reverse Reaction 1 taking place in the oxide bulk. That two opposite reactions take place at the same temperature is just a matter of the concentration of the reacting species: The large amount of interface silanols tends to favor the creation of interwafer siloxane bonds, while water diffusing in a silanol-poor oxide (thermal oxide) tends to favor siloxane hydrolysis in the oxide bulk.

The location of the Si/SiO_2 buried interfaces for each initial wafer is clearly visible on the electron density profile presented in Fig. 2 as small humps in electron density (due to some denser structure of the oxide close to the silicon). Hence the total thickness of the oxide can also be accurately measured from the data. These data show no thickness increase, whatever the initial thermal oxide thickness. This indicates that, contrary to silicon/silicon or silicon/oxide bondings where the native oxide growth was clearly visible, the Si/SiO_2 buried interface remains watertight up to 400°C. This result is also confirmed by measuring the hydrogen release when mechanically opening the interface in a vacuum vessel connected to a mass spectrometer. Contrary to the standard silicon bonding, oxide–oxide bondings show no released hydrogen for interfaces annealed up to 400°C.

To assert these XRR results, structures with various oxide thicknesses were stacked and observed by HRTEM. Cross section observations were performed using a 200 keV Akashi 002B transmission electron microscope (TEM). The observation of a 4 nm $SiO_2 \parallel 7$ nm SiO_2 bonded structure is shown in Fig. 3. A mean 11

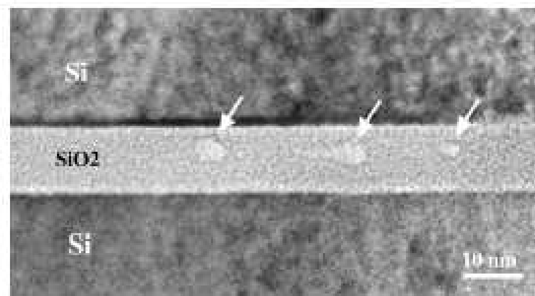

Figure 3. TEM image of a 4 nm $SiO_2 \parallel 7$ nm SiO_2 bonded structure. Unbonded zones (white arrows) are clearly visible in this cross section observation.

nm buried oxide total thickness can be measured. The bonding interface is only lightly visible. It can be located thanks to the thinnest, flat unbonded areas. Its location agrees with the initial thickness values of each oxide layer (i.e., 4 and 7 nm). The predicted increase in unbonded zone heights has been put into evidence. These pockets extend symmetrically relative to the bonding interface. Their height is up to 4.3 nm (Fig. 3), which is very consistent with the values obtained by XRR measurements (Fig. 1).

To confirm this mechanism, FTIR-MIR spectroscopy experiments were performed on different samples after postbonding anneal to investigate water evolution at the bonding interface. For this, we focused our study on the O–H stretching absorption band ($3200–3700$ cm^{-1}), which is composed of two regions: molecular water ($3225–3400$ cm^{-1}) and hydroxyl groups (–OH) ($3500–3700$ cm^{-1}). Figure 4 shows the O–H absorption spectra of the samples before and after annealing at different temperatures. First, we observe that from room temperature to 250°C, the O–H absorption band remains almost unchanged. However, the contribution of O–H vibrations in the molecular water region is less intense. This decrease in molecular water contribution comes with the apparition of a shoulder at 3640 cm^{-1} attributed to Si–OH vibrations in silica glass. This evolution is not comparable to the behaviors of the Si–Si and $Si–SiO_2$ structures, where the O–H absorption band has disappeared from room temperature to 250°C because of water consumption necessary for silicon oxidation.[7] Here, most of the water

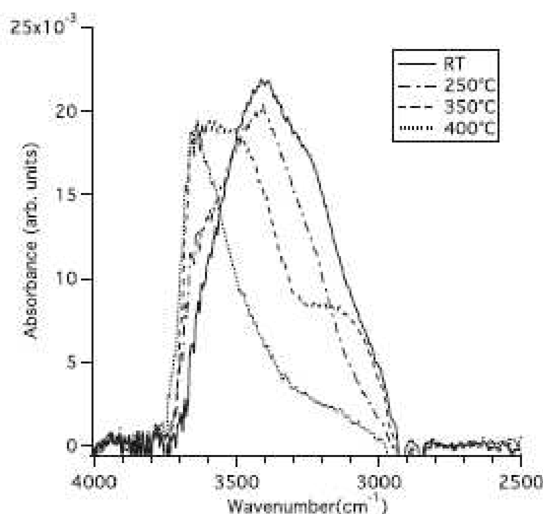

Figure 4. Evolution of the O–H absorption band in FTIR-MIR experiments measured after postbonding anneal at different temperatures.

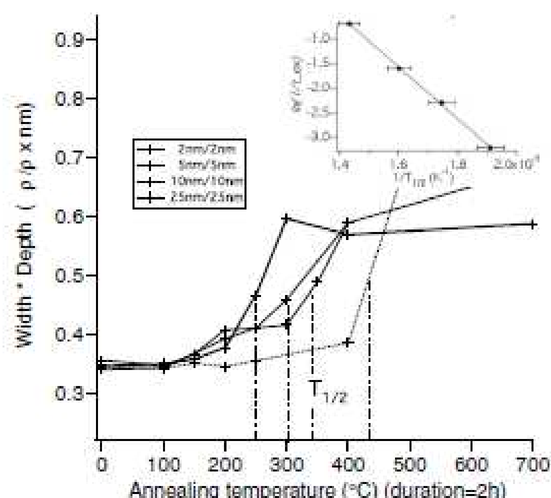

Figure 5. Interface electron deficit as a function of temperature for different oxide thicknesses. The temperature $T_{1/2}$ corresponds to water departure from the interface. Insert: Arrhenius plot of concentration vs $T_{1/2}$.

stays trapped into the bonding interface while the bonding interface closes up. From 250 to 350°C, the 3640 cm^{-1} shoulder becomes more intense and is finally the main component of the O–H absorption band after annealing at 400°C. The molecular water contribution drastically decreased in the same temperature range. It means that above a critical temperature T_e, molecular water could diffuse into the thermal silicon oxide volume and be stored under Si–OH form.

The process of diffusion/reaction of water into silicon oxide was studied by Rigo et al.[10] and Doremus et al.[11] The order of magnitude of both diffusion coefficients and reaction rates given in Ref. 11 is in accordance with our observations of an interface that is still full of water after 2 h at 200°C while nearly empty at 400°C.

The hydrolysis rate of siloxane bonds into silanols decreases with increasing silanol concentration. We observed that higher temperature anneals T_e were necessary to empty the interfaces of thinner oxides (Fig. 5). Assuming from the room temperature X-ray data that the same amount of interfacial water is diluted into different oxide thicknesses t_{ox} and plotting the concentration $[\ln(1/t_{ox})]$ as a function of the inverse T_e (insert of Fig. 5), we could observe a linear dependence with an activation energy of 0.88 eV/mol, which agrees with the activation energy of the siloxane hydrolysis reaction.[12]

To summarize, bonding mechanisms in the SiO_2–SiO_2 structure can be separated in two steps. The first one is a standard sealing phase ($T < 300°C$) where bonding interface closes up through the enlargement of contact points, which explains the interface density increase. Contrary to Si–Si and Si–SiO_2 bondings, there is no water evacuation from the bonding interface in this phase, leading to a wider profile with a higher density. Most of the water stays at the bonding interface trapped in higher unbonded zones. A more important surface area is bonded, and thus the bonding energy increases.

Then, at higher temperatures, the interface density decreases, which is associated with water diffusion out of the interface and reaction into thermal oxide films, leading to the formation of Si–OH groups within the oxide. There is no increase in the oxide thickness, suggesting that the Si/SiO_2 interface (which exhibits a high density oxide layer) remains impermeable to water diffusion.

Acknowledgment

We thank Dr. I. Radu for fruitful discussions and Soitec for financial support.

The Commissariat à l'Energie Atomique (CEA) assisted in meeting the publication costs of this article.

References

1. J. B. Lasky, *Appl. Phys. Lett.*, **48**, 78 (1986).
2. D. Feijoó, Y. J. Chabal, and S. B. Christman, *Appl. Phys. Lett.*, **65**, 2548 (1994).
3. H. Takagi, K. Kikuchi, R. Maeda, T. R. Chung, and T. Suga, *Appl. Phys. Lett.*, **68**, 2222 (1996).
4. Q.-Y. Tong, G. Fountain, and P. Enquist, *Appl. Phys. Lett.*, **89**, 042110 (2006).
5. F. Rieutord, J. Eymery, F. Fournel, D. Buttard, R. Oeser, O. Plantevin, H. Moriceau, and B. Aspar, *Phys. Rev. B*, **63**, 125408 (2001).
6. C. Maleville, O. Rayssac, H. Moriceau, B. Biasse, L. Baroux, B. Aspar, and M. Bruel, in *Semiconductor Wafer Bonding 4; Science, Technology, and Applications*, U. Gösele, H. Baumgart, T. Abe, C. E. Hunt, and S. Iyer, Editors, PV 1997-36, The Electrochemical Society Proceedings Series, Pennington, NJ (1997).
7. C. Ventosa, F. Rieutord, L. Libralesso, C. Morales, F. Fournel, and H. Moriceau, *J. Appl. Phys.*, **104**, 123524 (2008).
8. F. Rieutord, H. Moriceau, R. Beneyton, L. Capello, C. Morales, and A.-M. Charvet, *ECS Trans.*, **3**(6), 205 (2006).
9. M. K. Weldon, V. E. Marsico, Y. J. Chabal, D. R. Hamann, S. B. Christman, and E. E. Chaban, *Surf. Sci.*, **368**, 163 (1996).
10. S. Rigo, F. Rochet, B. Agius, and A. Straboni, *J. Electrochem. Soc.*, **129**, 867 (1982).
11. R. H. Doremus, *J. Mater. Res.*, **10**, 2379 (1995).
12. J. K. West and L. L. Hench, *J. Mater. Sci.*, **29**, 5808 (1994).

III. 3. Résultats scientifiques importants sur GMT

Protrusion modes in single supported lipid bilayers

T. Charitat, J. Daillant, G. Fragneto, L. Malaquin
CEA-DSM/IRAMIS/SCM/LIONS Saclay - Inst. Ch. Sadron Strasbourg – Inst. Laue Langevin, Grenoble
ESRF - SC2748

The physics of fluid membranes is intrinsically a multiscale phenomenon. At the molecular scale, single phospholipids display translational, rotational and vibrational motion. In turn, the collective motion of the membrane at larger length scales reveals the constitutive parameters of the membrane as its elasticity. A wide variety of physical phenomena, like phase transitions, equilibrium and non-equilibrium fluctuations, or destabilization and topological changes involve complex mechanisms in a range of length scales going from nanometer scale to hundreds of microns. In particular, lipid protrusions which are molecular-scale fluctuations of the molecules protruding out of the membrane play a key role in short-range potential and are essential for many biological properties. Nevertheless, this molecular-scale fluctuations are difficult to access experimentally, and have essentially been studied theoretically [1] and numerically [2].
The aim of the experiment was to investigate the cross-over between collective fluctuation modes and the individual protrusion modes. In order to achieve this goal, we extended a recent experimental work [3] to investigate strongly adsorbed or grafted bilayers. Experiments were carried out on single supported bilayer (DSPC and DMPC in both gel and fluid phase (see figure 1 left)) deposited on silicon substrates. All samples, including bare silicon wafers and first grafted layers, were characterized by specular reflectivity measurements.

These experiments clearly show that the single bilayer interaction with the silicon substrate is strong enough to suppress the collective fluctuation modes, and we observe a q^{-2} fluctuation spectrum, associated to a large surface tension ($\gamma \sim 70$ mN.m−1). This observation is in good agreement with theoretical paper [2] and recent numerical simulations [1] (see Fig. 1 right). As far as we know, this is the first direct experimental observation of this short wavelength spectrum. We could also investigate the effect of chain length by performing experiments on shorter molecules (DMPC). The interpretation of this experiment is still in progress. We were also able to record the off-specular scattering from fully charged phospholipid bilayer (100 %). These preliminary experiments show interesting correlated fluctuations of the double bilayer, and a possible effect of charges on protrusion modes.
The beamline BM32 was working well (although the 16-bunch lead to a doubling of the acquisition time, as expected) and the beamtime was used at 100%. Sample preparation was also satisfactory, according to both quantitative (transfer rates reproducibly > 95%) and qualitative criteria.

[1] Lipowsky, R. and Grotehans, S., Hydration vs. protrusion forces between lipid bilayers, Europhysic Letters 23, 599-60 (1993).
[2] Lindahl, E. and Edholm, 0., Mesoscopic Undulations and Thickness Fluctuations in Lipid Bilayers from Molecular Dynamics Simulations, Biophysical Journal, 79, 426-433 (2000).
[3] J. Daillant, E. Bellet-Amalric, A. Braslau, T. Charitat, G. Fragneto, F. Graner, S. Mora, F. Rieutord, B. Stidder Structure and fluctuations of a single floating lipid bilayer, PNAS 102 11639-11644 (2005).

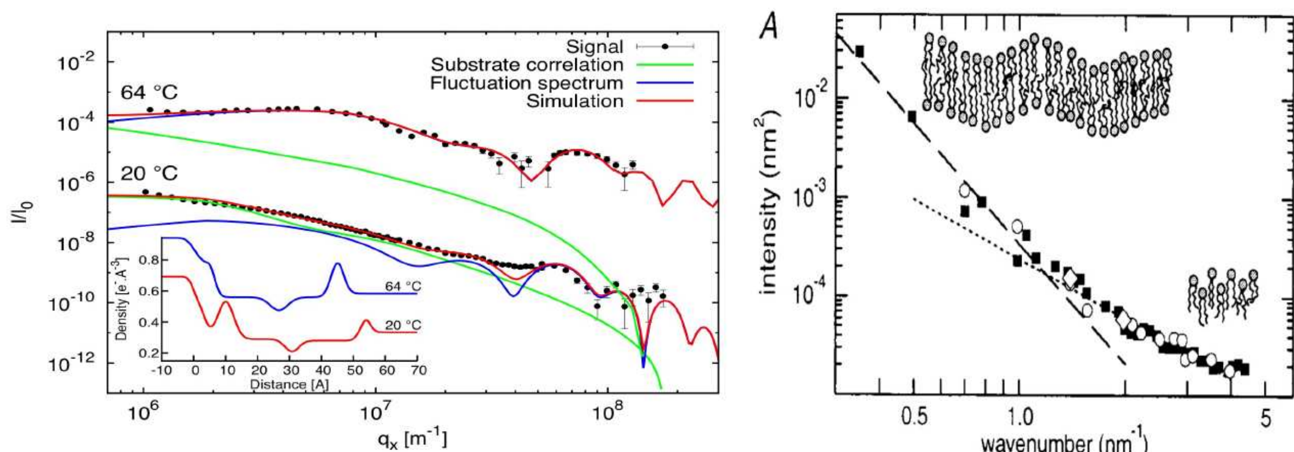

Fig.1: (left) Off-specular reflectivity experiments of a single supported DSPC bilayer in gel an fluid phase and best fit (in insert electronic density profile). (right) Results from numerical simulation showing the cross-over between collective fluctuation modes (small wave number) and individual protrusion modes.

Silicon and Copper solid/solid interfaces studied by hard X-rays

F. Rieutord, J.D. Penot, R. Feilleux, C. Ventosa, S. Vincent
CEA-DSM/INAC Grenoble, CEA-DRT/LETI Grenoble, SOITEC Bernin
FR 32-02-707

One of the key assets of the CRG-IF beamline at ESRF is the availability of a large flux of hard X-ray photons (up to 30keV for focused beams), suitable to study interfaces located under large thickness of materials. We have developed in the recent years the interface reflection technique, which allows the direct inversion of the scattering signal to obtain the interface structure, with no fit procedures or phase loss problems.
Important types of such interfaces are the interfaces obtained by direct bonding, i.e. the spontaneous adhesion of two flat materials when pressed against each other. This assembling technique is developing rapidly as it allows the fabrication of heterostructures that can not be manufactured by the standard epitaxy techniques. In particular, it allows the assembling of bulk crystals or materials that have been grown separately, under conditions that may be very different for the two materials. Among the key applications of direct bonding, let us mention the fabrication of Silicon-On-Insulator substrates (assembling silicon to silicon oxide) or the so-called 3D integration (to increase the density of microelectronic components) involving metal to metal bonding.
We present below examples of the hard X-ray scattering surface techniques to two problems relating to these two applications.

1-Effect of thermal silicon oxide films on bonding [2]

We demonstrated in several papers the role of the water layers trapped at the interface on the bonding mechanisms. In the standard situation, water crosses one of the native oxide films to react with silicon. This produces additional silicon oxide and hydrogen, which have to be managed in subsequent technological processes. We have investigated here the case of the bonding of two thermal oxide covered wafers. Our previous studies had shown that at low temperatures, water can not cross thermal oxide [3,4]. The interface density profile evolution in the oxide-oxide bonding case is shown figure 1.

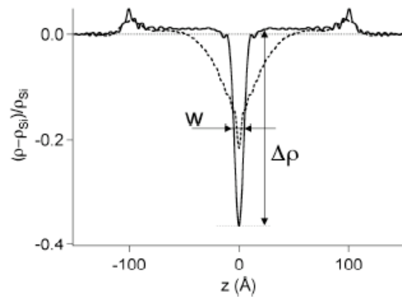

Fig.1 Interface density evolution between ambient and 250℃ annealing temperatures. The broadening of the interface is clearly visible

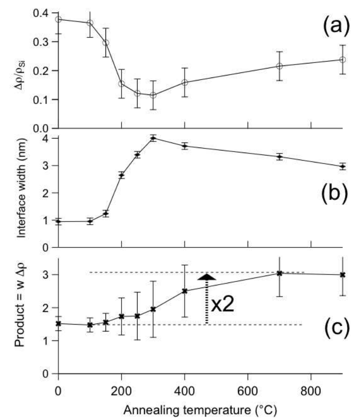

Fig.2 Evolution of depth (a) , width(b), and surface area (c), of the interfacial density profile as a function of annealing temperature.

It can be seen that the interface broaden considerably compared to the standard Si/SiO2 case. Measuring the product of the depth times the width of the interface (which is the overall electron interface density deficit) , we can show that it remains constant in a first stage, then increases. This means that the interface closure occurs without water departure from the interface, along a “ziplock” mechanism that has been already proposed. Upon closure, water will form pockets that have been subsequently researched and finally observed using TEM. (fig.3).

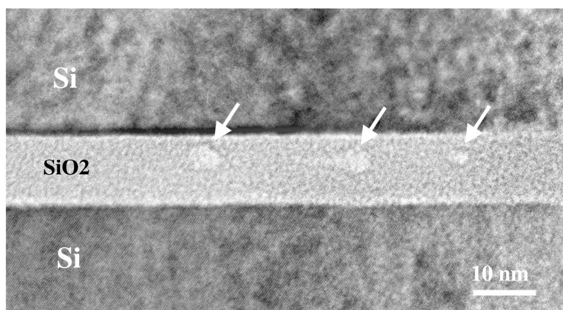

Fig.3 TEM view of a SiO2/SiO2 bonding interface showing the water pockets evidenced previously by X-ray reflection

Only at higher temperature will water finally leave the interface pockets it has formed, diffusing into the silicon oxide , then in silicon.
These results not only confirm several interface closure mechanisms that were proposed in other cases but also give quantitative values for the parameters at play in these mechanisms (amount of material, distances, diffusion coefficients, activation energies…) and have interesting practical consequences on the strategy to reduce the number of interfacial defects [1].

2-Copper-copper interface evolution upon annealing

3D integration is a key current issue in the microelectronics roadmap to increase component densities in integrated circuits. The possibility to perform the assembling of materials under little thermal budget by bonding is thus very attractive. In order to understand the mechanisms of metal/metal bonding (used to connect different part of a circuit), we have studied the temperature evolution of a copper/copper bonding interface, in-situ. For that two wafers covered by a copper blanket films were bonded and annealed in situ. Compared to silicon and silicon compounds bonding, the strong absorption of copper and the presence of many additional interfaces in this

Si/SiO2/TiN/Cu//Cu/TiN/SiO2/Si stack makes the interface study more difficult. However the different periods of the interference structures allow the separation of the copper/copper interface contribution. An example of the density profile evolution upon thermal annealing is shown Fig.4.

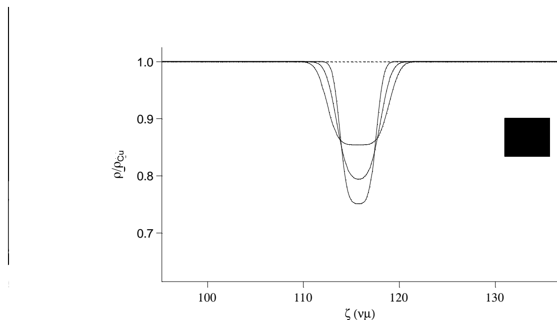

Fig.4. (left) Density profile of a Cu/Cu interface bonding. (right) Central part corresponding to the Cu//Cu interface at different temperature.

The interpretation of the observations is still under progress but it seems already clear that different mechanisms have to be considered compared to Si/Si bonding. Note that in addition to interface profile measurements, in-situ scattering on different Bragg line of the copper could be performed which allows the determination of the strain and stress level in this system.

[1] *S. Vincent, I. Radu, D. Landru, F. Letertre, and F. Rieutord, "A model of interface defect formation in silicon wafer bonding " Applied Physics Letters, vol. 94, pp. 101914, 2009.*

[2] *C. Ventosa, C. Morales, L. Libralesso, F. Fournel, A. M. Papon, D. Lafond, H. Moriceau, J. D. Penot, and F. Rieutord, "Mechanism of thermal silicon oxide direct wafer bonding," Electronic and Solid State Letters, vol. 12, pp. H373, 2009.*

[3] *C. Ventosa, F. Rieutord, L. Libralesso, F. Fournel, C. Morales, and H. Moriceau, "Effect of Pre-bonding Thermal Treatment on the Bonding Interface Evolution in Direct Si-Si Hydrophilic Wafer Bonding," ECS Transactions, vol. 16, pp. 361-368, 2008.*

[4] *C. Ventosa, F. Rieutord, F. Fournel, C. Morales, L. Libralesso, and H. Moriceau, "Hydrophilic low temperature direct wafer bonding," Journal of Applied Physics, vol. 104, pp. 123524, 2008.*

Stress heterogeneities measurements on i*n situ* loaded polycrystalline W

O. Castelnau, C. Le Bourlot, R. Chiron, O. Robach

LPMTM Villetaneuse, CEA-DSM/INAC Grenoble

FR 32-02-693

The goal of this experiment was to quantitatively estimate the accuracy of the Laue microdiffraction setup recently installed on BM32, in particular the absolute accuracy of the strain tensor. This is in view of using the setup later for the study of plastically deformed polycrystalline materials. The long term aim of our research is to understand the way polycrystalline materials deform in the plastic regime, with emphasis on the link between microstructure (dislocation structure, crystallographic texture), activated deformation mechanisms at the grain scale (dislocation glide, dislocation climb, twinning), and overall behaviour. When polycrystals are deformed plastically, since individual grains exhibit an anisotropic plastic behaviour, they react differently to the prescribed load, and this gives rise to strong mechanical interactions between grains, with substantial redistribution of stress between "hard" and "soft" grains. Current theoretical efforts aim at predicting quantitatively the effect that these interactions have on the effective strength of a material, and on the evolution of the microstructure during mechanical testing. However there is still lack at present of precise analysis of the corresponding stress heterogeneities in the deformed grains, at the relevant (i.e. micron) scale. This is

a severe limitation for a deeper understanding of many issues in Materials Sciences, e.g. resistance under fatigue loading, crack propagations, phase transformations, etc.

A new setup for white-beam microdiffraction, partly similar to the one developed at the ALS [4], was recently installed at beamline BM32 (ESRF). In principle, it allows 2D mapping of local stress in polycrystalline specimens with a (sub)micron spatial resolution. The white beam (energy range 5-30 keV) is focused down to a 0.8 x 1.5 µm2 cross-section with Kirkpatrick-Baez (KB) mirrors. The specimen is mounted on an x-y-z translation stage at 40° from the incident microbeam, thus allowing scanning microdiffraction with micron spatial resolution. Laue diagrams are recorded on a 2D detector (MAR CCD) positioned at 90° from the incident beam and a few centimetres away from the specimen. After having indexed the Laue pattern and found the local orientation, deviatoric strain can in principle be obtained by a careful analysis of the distortions of the experimental Laue diagram. Local stress is then derived from lattice strain using the elastic constants of the scanned grain.

However, for this analysis, advanced image processing is needed to reach the desired accuracy of ~10^{-4} on the lattice parameters, which typically translates into ~0.1 pixel accuracy on the positions of the Laue spots. It is worth noting that the required resolution is far not attained with available softwares, such as XMAS developed at the ALS (and broadly distributed among the community), owing to the use of unadapted image processing procedures. Indeed, XMAS requires a fit of Laue spots by simple analytical functions (such as Gaussian) although those spots exhibit most of the time a much more complex shape. As a consequence, one classically obtains stress levels of the order of GPa even in very soft materials (such as pure Cu) for which stresses larger than ~50 MPa are obviously unrealistic. One also finds very few quantitative data analysis in the literature (and in that case with only few details concerning the evaluation procedure), although the setup at ALS and APS are operational since about a decade. Furthermore, we do not know any publication providing a realistic estimation of uncertainties on the obtained stress levels, as well as the dependence of the accuracy on the experimental conditions. This matter of fact motivates the development of a new open source analysis software at BM32 (J.S. Micha), and the present experiment.

The purpose of this particular experiment was to collect a number of scans on a pure W specimen, elastically deformed in situ under uniaxial tension, in both white beam and monochromatic microdiffraction setup. For doing this, we have mounted a tensile machine with a load capacity of 10.000 N, developed at LPMTM, on the translation stage of the microdiffraction setup. The choice of W was justified by its high yield stress (~500MPa) and its well known elastic isotropy at the grain scale, so that any macroscopic loading gives rise a uniform stress field increment inside grains. The measured stress field is therefore exactly known in advance. We take advantage of this property to estimate the accuracy of the method: one should obtain, throughout the scans, uniform stress maps which value matches the stress increment applied between two successive loading steps of the specimen.

Furthermore, as for the processing of Laue image, we are testing a completely new method, based on image correlation. For this, we have developed a procedure in two steps.

First, it is necessary to be able to superimpose, with a resolution of ~1 micron, two successive scans measured at two load levels. For this, a software has been developed and tested for a careful analysis of some specific regions of the Laue diagrams. Figure 1 shows two Laue patterns measured at the same position (within the 1 micron accuracy) for specimen loadings of 5 MPa and 500 MPa. One clearly recognizes the very strong similarity of both pattern.

(ii) Next, we have adapted and made use of an image correlation method to calculate the relative displacements of Laue spots on the camera, for increasing loading of the specimen (figure 2). First tests are in very good agreement with the solution (analytical in this case). There is still some ongoing work on those data, but we are now confident that the developed procedure will provide an accuracy adapted to that required for micromechanical studies, with many potential applications.

To develop the method few steps further, and in view of its latter implementation of the new software developed at BM32, we have applied very recently for funding for a one-year post-doc, and we got success. The post-doc will start hopefully before the end of the current year.
This work will be presented at a national (french) workshop focussed microdiffraction techniques that will be held at ESRF in sept. 2009. A publication is planned for 2010.

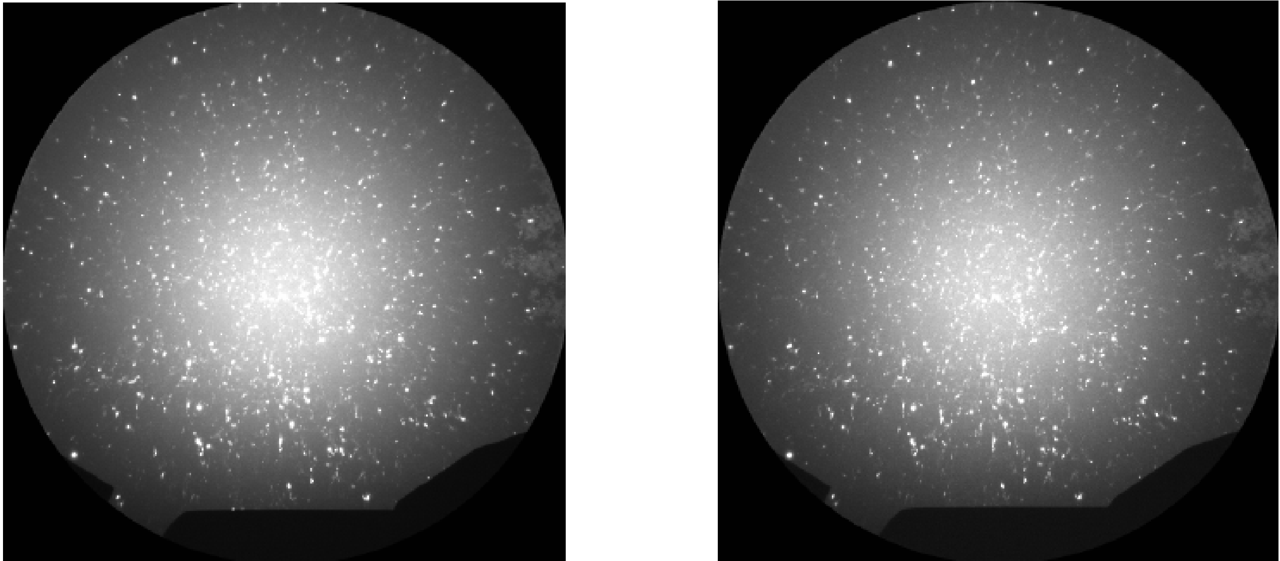

Figure 1. Laue Patterns measured on the tensile deformed W polycrystalline specimen at 5 MPa (left) and 500 MPa (right) macroscopic loading. The displacement of Laue spot is small (of the order of 1 pixel) but visible.

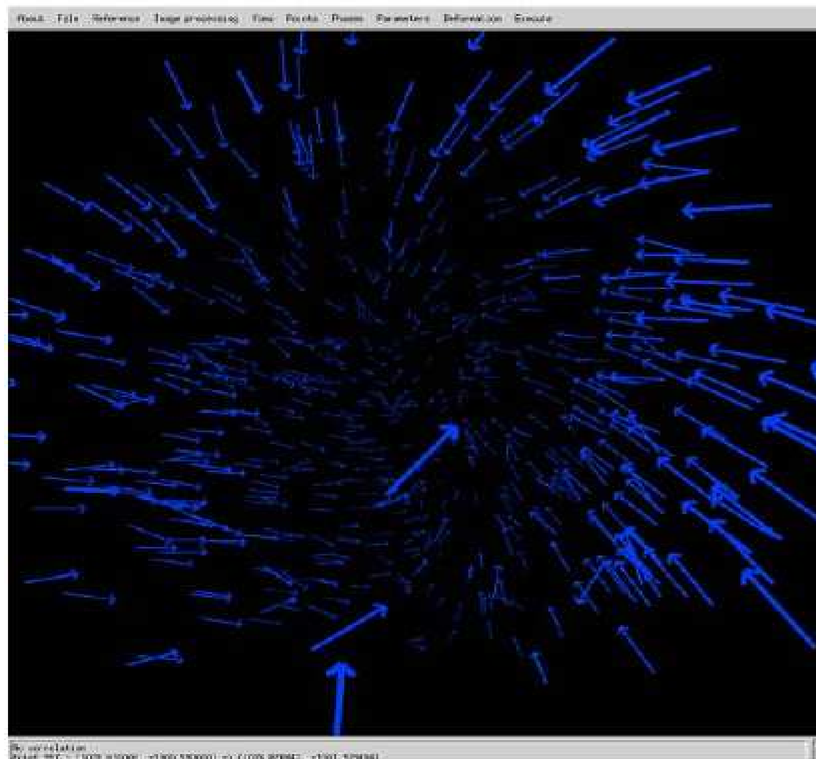

Figure 2. Displacement of Laue spots on the X-ray camera obtained by the proposed image processing procedure. The displacement has been calculated between the two Laue diagrams shown in figure 1. Except for few spots for which the

image processing apparently does not work well, most of the 500 spots on this image exhibit a cooperative movement toward the center of the camera, in good agreement with the theory.

Stress tensor determination and crystal orientation evolution during uniaxial loading of a copper bicrystal

T. Hoc, B. Devincre, G. Daveau, O. Robach
Ec. Centrale Paris&Lyon, ONERA Chatillon, CEA-DSM/INAC Grenoble
ESRF- MA555

A copper bi-crystal was mounted in the compression-loading machine shown in Figure 1, with an additional stress-sensor (not shown). The grain boundary (GB) is perpendicular to the axis of loading. The machine was installed using a specially made plate into the BM32 microdiffraction setup. The working plane was 3 mm downstream of the ideal KB-focussing plane along the beam, in order to avoid collisions between the machine and the KB enclosure.

Figure 1: copper bi-crystal in the compression machine. The loading electric motor on the left side is unmounted here.

The bi-crystal deformation was investigated, using both white beam (for orientation and deviatoric strain mapping) and monochromatic beam (for lattice expansion mapping). Four states of strain were studied in a centered area including the GB: (1) before loading, (2) at yield, (3) in the plastic domain at ~2% strain, and (4) after unloading.
For each deformation step, the compression machine was removed from the microdiffraction setup to mount the electric motor and monitor the local deformation qualitatively (e.g. appearance of slip lines) and global deformation quantitatively (macroscopic strain) with a large-field optical microscope. The latter measurement is performed with the help of accurate photographs of two widely spaced lines of nano-indentation prints made on the top surface of the sample (see figure 2).
The experimental geometry was calibrated in the white beam mode using a Ge(111) single crystal.
Three sets of measurements were collected at each loading step (with the grain boundary perpendicular to the x axis): using white beam (1) a large map of 500 x 500 microns in x and y, with a step of 5 microns in x and 10 microns in y and (2) three x-lines centered on the grain boundary, of 100 microns along x with a 1 micron step. Also, using monochromatic beam (3) one energy scan at 8 points along a x-line around the centre of the large map, at (-250, -125, -10, -5, +5, +10, +125, +250) microns in x from the grain boundary.

Data analysis shows correlation between the glide system, visible on the microscopic view, and the microdiffraction results, particularly in term of local lattice rotation. Figure 2 shows the sample surface before and during compression. The area studied with x-rays is marked with a red square. The orientation maps (i.e. local rotation of the lattice) are reproduced for the right grain. These maps were obtained from Laue patterns analysis with the XMAS program. The optical microscope view (fig 2-A) reveals slip traces after compression, in particular on the bottom of the grains, which are well correlated with the areas of high otation plotted in fig 2-B. The effect of the GB on the local lattice rotation and on the slip patterns is clearly shown in this figure. Work is in progress to calculate the stress maps corresponding to the figure 2.

As a preliminary step to the micro plastic strain calculation, which affects the shape and width of the Laue spots, maps of the spot-width (as fitted with a Lorentzian shape function) are reproduced in figure 3. Additional data analysis and theoretical work is needed to calibrate the Laue peak shapes evolution in terms of orientation / strain distribution and dislocation density.

These results will be used to develop a physically justified crystal plasticity constitutive law accounting

for the influence of grain boundaries during deformations. Results of this study were selected as an oral presentation in the TMS symposium "Neutron and X-ray studies of advanced materials" (February 2010, Seattle).

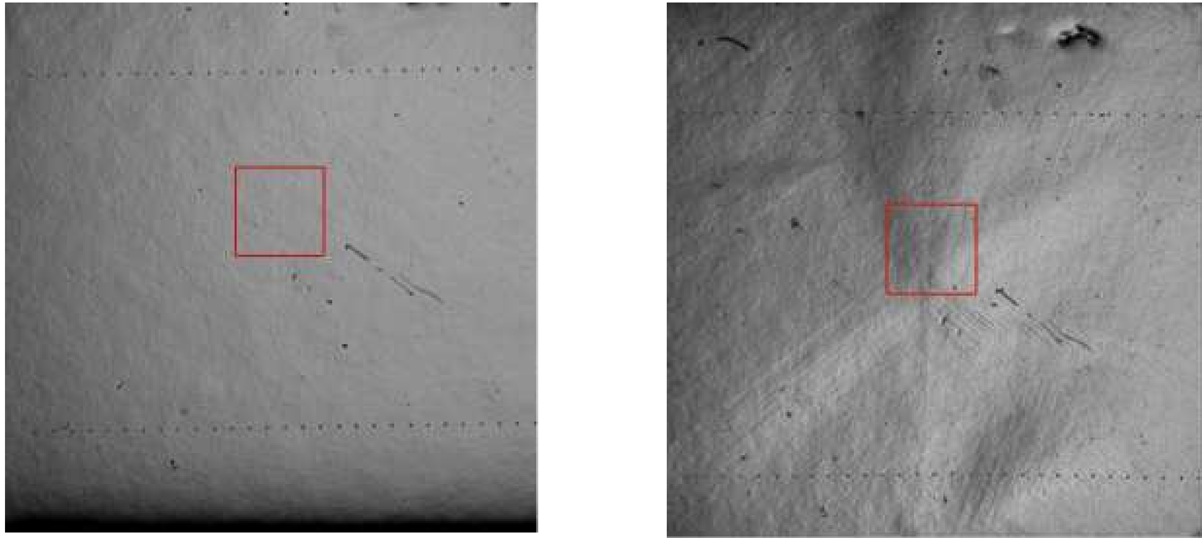

Figure 2.A) Optical microscope view (spacing of indentation points = 100 microns (before loading state 1 and loading at 423N state 3)

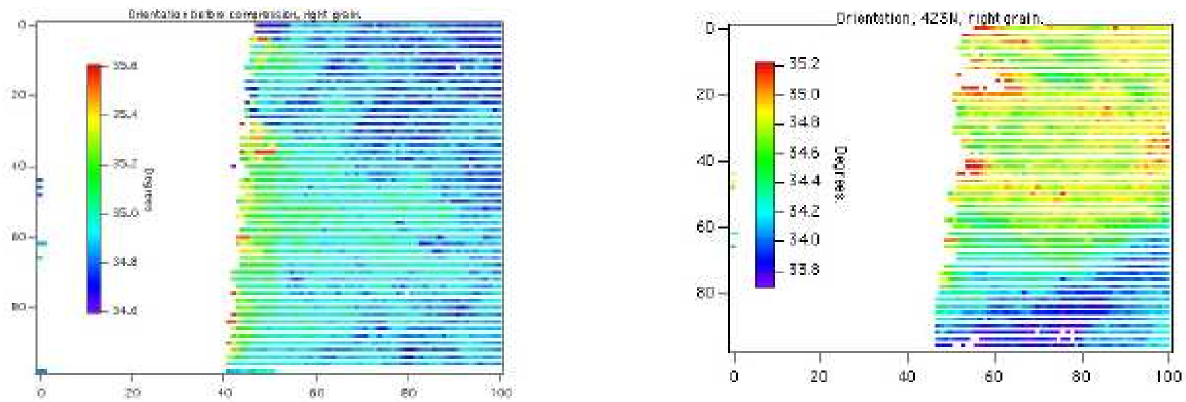

Figure 2.B) Local orientation maps 500 x 500 microns2 (before loading state 1 and loading at 423N state 3)

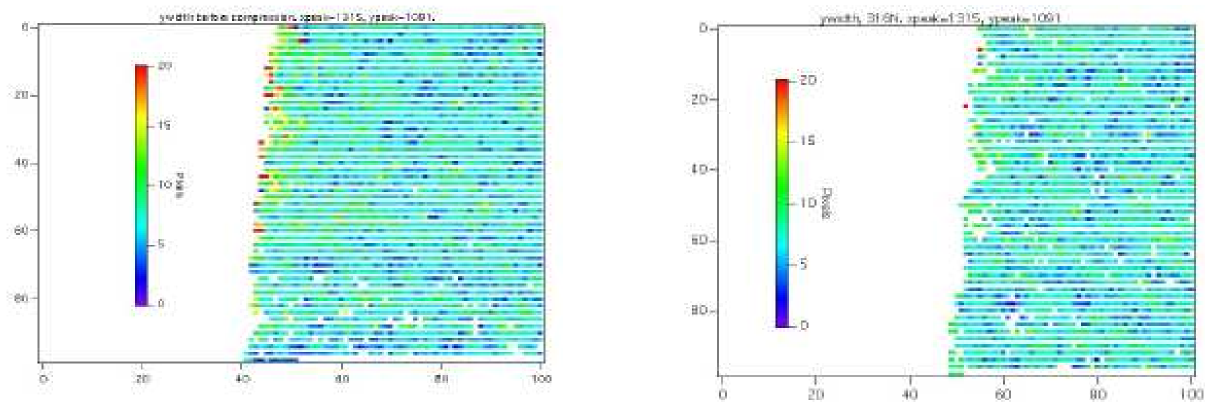

Figure 3: Map of the width (along the y axis) of a characteristic Laue peak, before compression and at F=316N

Détermination des contraintes locales dans des objets de cuivre de taille micrométrique

O. Perroud, O. Thomas, S. Labat, C. Kirchlechner, J. Keckes
IM2NP Marseille, Leoben Univ Autriche
FR 32-02-694

L'équipe a étudié deux types d'échantillons. La majeure partie du temps de faisceau a été consacrée à déterminer les contraintes locales dans des jauges de contraintes (MEMS). Le reste a été employé avec succès à lever des ambiguïtés d'interprétation des données collectées sur un micro pilier.

Dimensions du faisceau

A l'occasion de cette expérience, l'extension des queues du faisceau dans les directions horizontales et verticales a été mesurée. Avec une forme assez proche d'une gaussienne, la taille du faisceau incident est caractérisée par la largeur du front de montée du signal de fluorescence lors du passage sur un bord abrupte de cuivre. Cette largeur à mi-hauteur est inférieure au micromètre lorsque les miroirs de ligne peuvent être suffisamment courbés (sinon inférieure à 2 microns). Le signal de diffraction Laue d'un plot d'Au (fort diffuseur) de 1x1 micron est encore visible alors que le faisceau est à plus de 10 microns de ce dernier. Cette faible extension latérale de la sonde de diffraction n'est très généralement pas une difficulté lors des expériences ou de l'analyse. Ce plot a servi aussi à caractériser le micro-faisceau X de l'installation de microdiffraction de l'ALS. L'installation de BM32 a montré de meilleures performances: les pics de diffraction demeurent à des positions fixes durant le déplacement de l'échantillon.

Jauges de contraintes

La réduction de taille des éléments de la microélectronique amène l'industrie à s'intéresser aux contraintes dans les objets de petite dimension. Les mesures de contrainte moyenne dans les matériaux montrent une influence de la taille sur leur limite élastique. Au niveau local, des gradients de contrainte inter ou intra granulaire très importants sont observés. Le lien entre le comportement macroscopique des microstructures et la contrainte locale des matériaux reste difficile à analyser.
Les jauges de contrainte développées à STMicroelectronics Rousset (ci-dessous) peuvent servir à une meilleure compréhension du lien entre ces deux grandeurs dans les interconnexions de cuivre. La microdiffraction de Laue en faisceau blanc permet d'avoir une cartographie des orientations et des contraintes déviatoriques locales dans les polycristaux.

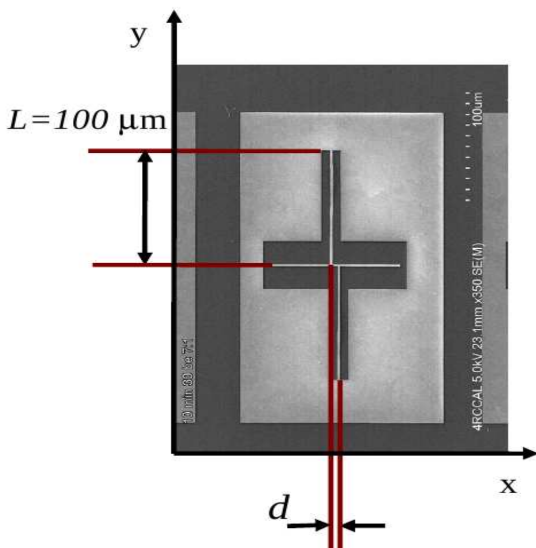

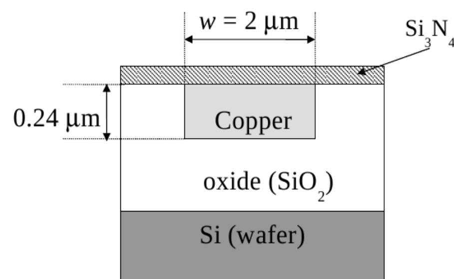

après désoxidation

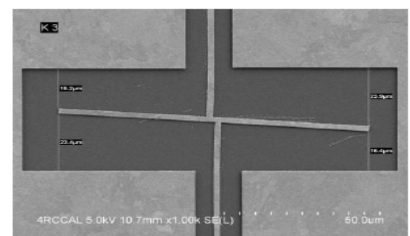

Des cartographies des orientations et des déformations ont été effectuées autour du centre du MEMS avant et après désoxydation. Cette expérience a combiné l'emploi du faisceau blanc et monochromatique. Après désoxydation (à l'acide fluorhydrique), l'oxyde de silicium disparaît laissant des poutres de cuivre déformer la croix afin de la relaxer les contraintes dans le cuivre. Il a été possible de travailler sur plusieurs MEMS après l'attaque chimique effectuée ex situ.

L'analyse des données est rendue difficile non pas par la taille latérale de sonde un peu plus importante en raison de la courbure des miroirs de ligne défaillants, mais par le recouvrement de pics de diffraction dans les diagrammes de Laue collectés. En effet, la présence de grains voisins en relation de macles produit des pics de diffraction qui ne sont pas nettement séparés car les déformations ne sont pas suffisamment importantes. La détermination des contraintes dans ce cas très délicate en raison de la forme dédoublée des pics, chacun étant allongé en raison de défauts liés aux contraintes, et du traitement très fastidieux nécessaire pour ne considérer que les pics dont le grain d'origine et les indices de Miller correspondant sont absolument certains.

Micro piliers

L'équipe de J. Keckes de l'université autrichienne de Leoben (groupe de G. Dehm) a complété ses mesures pour achever un article à paraître sur l'étude de la mécanique de déformation d'un pilier de Cu sous traction (ex-situ). Plusieurs systèmes de glissement sont activés pour accommoder la forte élongation. La rotation du cristal entre les différentes régions sondées ayant tourné les unes par rapport aux autres est clairement visible par le déplacement de la raie (111) mesurée sur tout le pilier. L'analyse de la direction d'allongement des pics de diffraction révèlent la nature des dislocations et la quantité de système de glissement activée après traction.

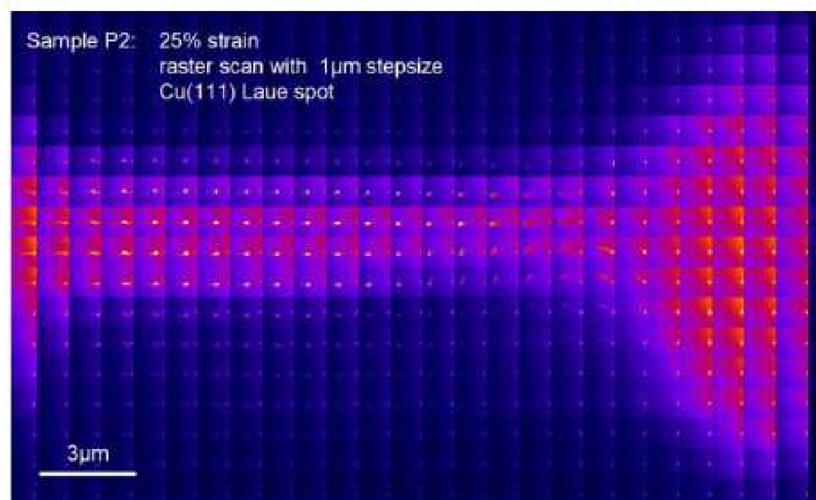

Evolution de la raie de diffraction Laue Cu (111) en fonction de la position sur l'éprouvette. Le déplacement de la raie et le changement de sa forme sont principalement donnés par respectivement la désorientation et la densité de défauts (dislocations)

Cette expérience a permis de valider l'analyse des données en vue d'une expérience acceptée par le comité de programme international sur l'étude semblable du comportement mécanique d'un micro pilier en traction uniaxiale in situ avec une machine construite par leur laboratoire. L'intérêt d'une telle démarche est de comprendre la mécanique et la métallurgie de microdispositifs avec une éprouvette de dimensions comparables à celles des objets qu'elle est censée représenter.

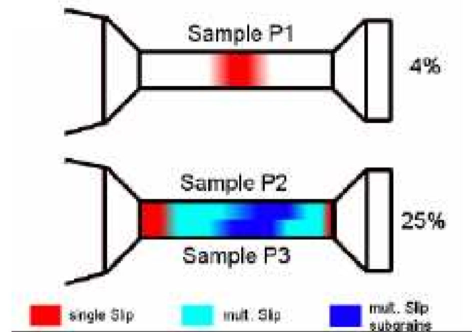

Localisation des zones d'activation simple ou multiple de systèmes de glissement

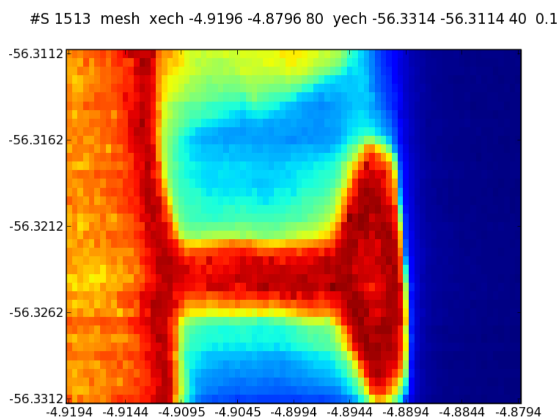

Cartographie de fluorescence du pilier (pas de 0.1µm)

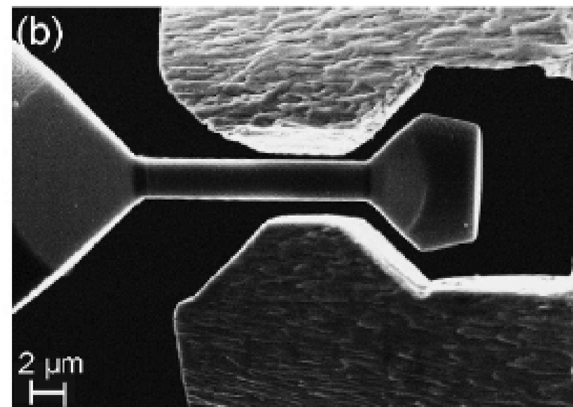

Principe de micro-traction envisagée pour la prochaine expérience acceptée par le comité de programme international

Depth-resolved Laue Imaging

P. Bleuet, O. Ulrich, O. Robach, X. Biquard, J.S. Micha, P. Gergaud

CEA-DSM/INAC Grenoble, CEA-DRT/LETI Grenoble

FR 32-02-700

La présente technique de microdiffraction consiste à réaliser une cartographie 2D du signal de diffraction Laue, comme n'importe quelle technique de microscopie. Il apparaît que l'approximation de ramener le signal provenant de volume sondé par les rayons X durs de l'ESRF, à un signal de surface conduit à 1) évidemment une incertitude sur la localisation en profondeur de l'origine du signal de diffraction mais aussi 2) à réduire la précision sur la détermination des déformations. En effet, la pénétration des rayons dans la matière implique que la profondeur moyenne d'émission d'un pic de diffraction collecté sur le détecteur varie d'un pic à l'autre pour un même grain. La calibration du

détecteur (distance, tilts, etc.) étant effectuée sur un cristal parfaitement connu (wafer de Ge non contraint), les paramètres de calibration sont obtenus de manière approchée à partir d'une source de pics de diffractions enfouie à une profondeur moyenne. Pour atteindre des résolutions de 10^{-4} sur les déformations, il est requis d'utiliser les paramètres de calibration correspondant à une profondeur donnée. Cette profondeur n'est malheureusement pas accessible expérimentalement à ce jour.
Pour localiser la source d'émission de pics de diffraction provenant de matériaux polycristallins, une méthode reposant sur un masquage différentiel par un fil des pics sortant de l'échantillon a été développée à l'APS (Differential Aperture X-ray Microscopy, Larson *et al.* Nature (2002)). Les premiers essais d'implémentation de cette méthode sur BM32 devraient être effectués au cours de l'année 2010. Elle nécessite un développement instrumental et logiciel approprié.
Une démarche alternative proposée par P. Bleuet, qui a acquis une longue expérience en tomographie et dans la reconstruction en 3D d'objets éclairés par rayons X, consiste à utiliser une rotation motorisée de l'échantillon (et non plusieurs pour s'affranchir de la sphère de confusion). Cette rotation de précision (excentricité limitée) a été développée sur ID22 à l'ESRF pour des expériences de tomographie par signal de fluorescence. Pour chaque point de l'échantillon on collecte le diagramme de diffraction Laue de l'échantillon à plusieurs angles (une trentaine). Cette méthode ne s'applique cependant qu'à des échantillons de taille micrométrique de manière à ce que l'absorption permette toujours de collecter le signal provenant d'un grain quelque soit l'angle. Cela restreint le champ d'application de la méthode (nécessité de préparation de l'échantillon par FIB, collage,...)

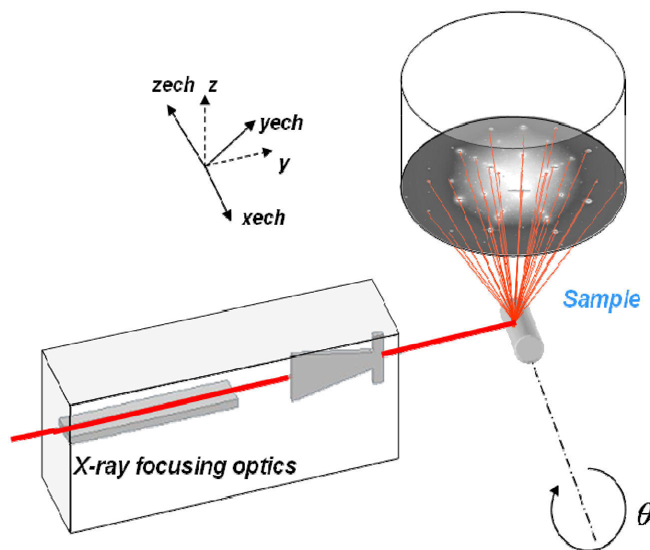

Principe de la Tomographie Laue.

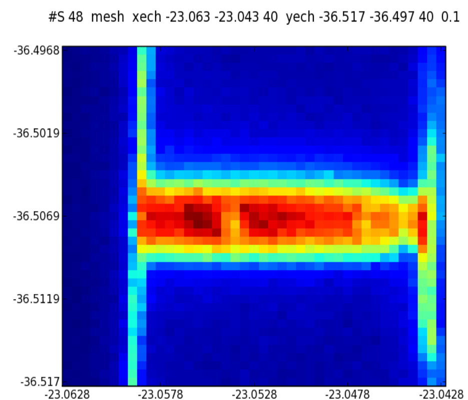

Carte de fluorescence d'un via de cuivre dans un substrat de silicium. La diminution du rendement de fluorescence correspond à l'absence de cuivre (void) nuisant au transport électronique à travers le via.

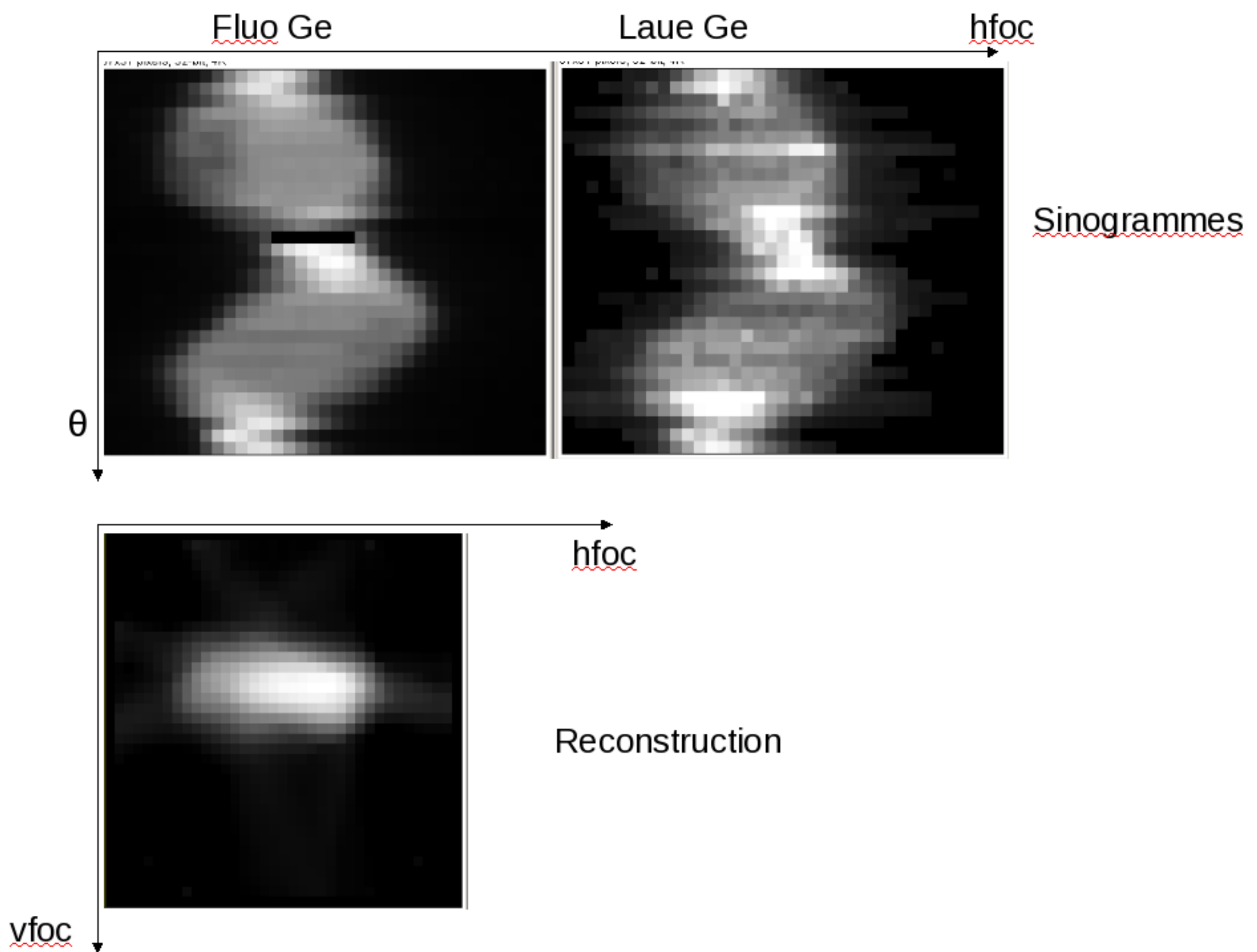

Pour un plan de coupe donné (à x fixé), le signal de fluorescence ou de diffraction lors d'un balayage combiné de l'échantillon (z et angle θ) permet à partir des sinogrammes de reconstruire la forme et l'intensité du signal (fluo ou diffraction) dans chaque voxel (x,y,z).

Cette première expérience a confirmé les conditions requises pour qu'une reconstruction 3D et la détermination du tenseur déviatorique des déformations soient réalisables. Il est impératif de réaliser une calibration du détecteur pour plusieurs profondeurs de pénétration et d'améliorer encore l'excentricité de la rotation. Des méthodes de corrections dans ce sens lors du traitement de données sont donc envisagées. L'emploi d'une future caméra au temps de lecture très court devrait permettre de plus d'améliorer le développement de cette technique ainsi que son attrait pour les utilisateurs.

Size and structure dependences on the catalytic activity for CO oxidation of gold nanoparticles supported on an unreducible α–Al_2O_3(0001) substrate

Marie-Claire Saint-Lager, Issam Laoufi, Pierre Dolle, Stéphanie Garaudée, ***Institut Néel-MCMF CNRS- Grenoble***

Rémi Lazzari, Jaques Jupille, Gregory Cabailh, Hervé Bruckel ***Institut des NanoSciences de Paris – CNRS-Université Paris 6-7***

FR 32-02-696

The goal of this experiment was to approach the role of the substrate on the correlation between the size and the catalytic activity of supported gold nanoparticles.

A preliminary study of the real-time growth mode of Au/Al_2O_3(0001) in ultra-high vacuum has been undertaken as function of substrate temperature and evaporation rate. Calcium contamination of the surface due to segregation from the bulk was observed. We spared the beamtime to conclude our study on the gold nanoparticles on TiO_2.

Indeed, all our reactivity measurements, in the frame of carbon monoxide (CO) oxidation, at the laboratory exhibit a maximum of activity as a function of the deposited gold amount (see figure 1). GISAXS measurements allow the correlation of this maximum to particles with a diameter of about 3 nm.

So, the aim of these experiments, with our setup mounted on the BM32 beamline, was to collect data to understand this maximum. This corresponds to equivalent gold thicknesses below 0.5 monoatomic planes.

For such low coverage the nanoparticles are not stable, and we showed that their distribution is strongly anisotropic.

This is illustrated by the GISAXS patterns on figure 2. The upper patterns are in UHV and at room temperature. Changes were not observed at room temperature even under gas pressure. At 473 K, particles become bigger and their density decreases. This is probably due to the thermal activation. When CO is added to Argon, no change is observed. But when it is added to oxygen a new sintering occurred. This can be linked to the local heating induced by the CO oxidation reaction itself.

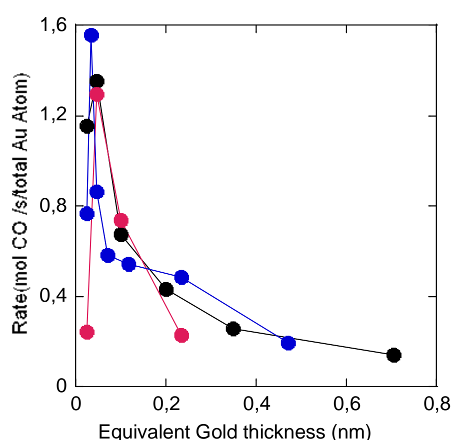

Figure 1 *: CO Conversion rate as a function of the deposited gold amount deposited on TiO_2(110) during 3 series of measurements at 473 K and when 20 mbar of oxygen + 0.2 mbar CO are introduced in the x-ray reactor-chamber*

We also observed that the GISAXS patterns and their evolution are direction dependant as also shown on figure 2. The distance between particles is initially higher along the dense rows of the TiO_2(110) surface than perpendicularly. The effect of gases is also stronger in this direction, indicating a larger mobility of the gold atoms along the rows.

Quantitative analysis is under progress to determine in each situation the size of the particles, their density to correlate them to the activity for CO oxidation.

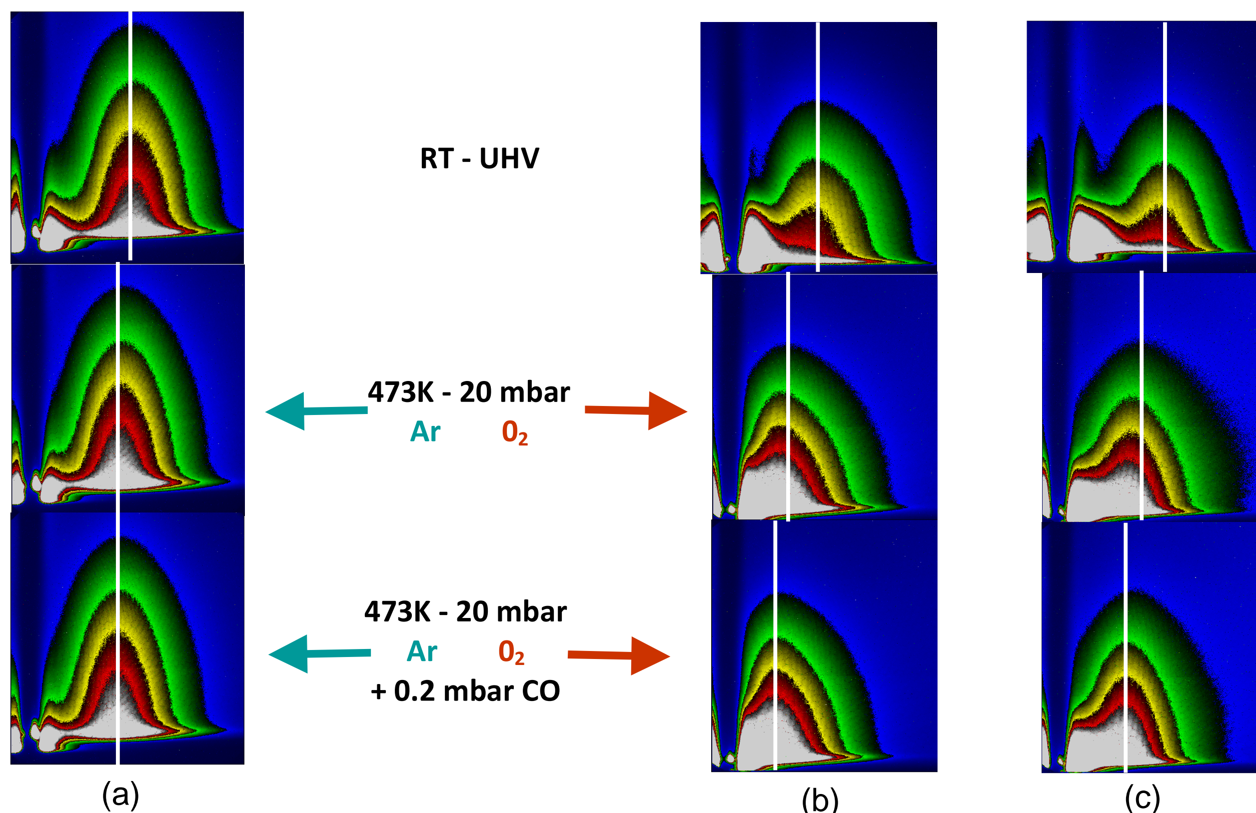

Figure 2 : *Evolution of the GISAXS patterns of a 0.04nm gold equivalent thicknesses, (a) and (b) in the direction parallel to the dense TiO_2 rows and (c) perpendicularly. In (a) Oxygen was replaced by the inert Argon.*

Together with GISAXS, we also collected diffracted intensity. This is illustrated on Figure 3 which shows its evolution along an azimuth scan through an in-plane gold peak. We observed three peaks : the central one, corresponding to the (111) epitaxy of gold with its dense rows parallel to the one of the TiO_2(110) substrate, and two satellites at ±4.5° which are attributed to rotational gold epitax y.

For the highest diameter the satellites are small relatively to the central one. The diffracted intensity does not evolve significantly under oxygen and during reaction conditions. For the smallest particles, in UHV the peaks are broad and weak; but under reaction the lonely satellites grow up. For intermediate diameter the three directions have roughly the same importance.

Regarding the lattice parameters, deduced from a preliminary analysis, those for the smallest particles with the rotational epitaxy, are deformed compared to the gold bulk ones with a dilatation in one direction and a small contraction in the two others. Such a result must be founded by a systematic quantitative analysis to determine if it can be correlated to the high catalytic activity of the supported gold nanoparticles.

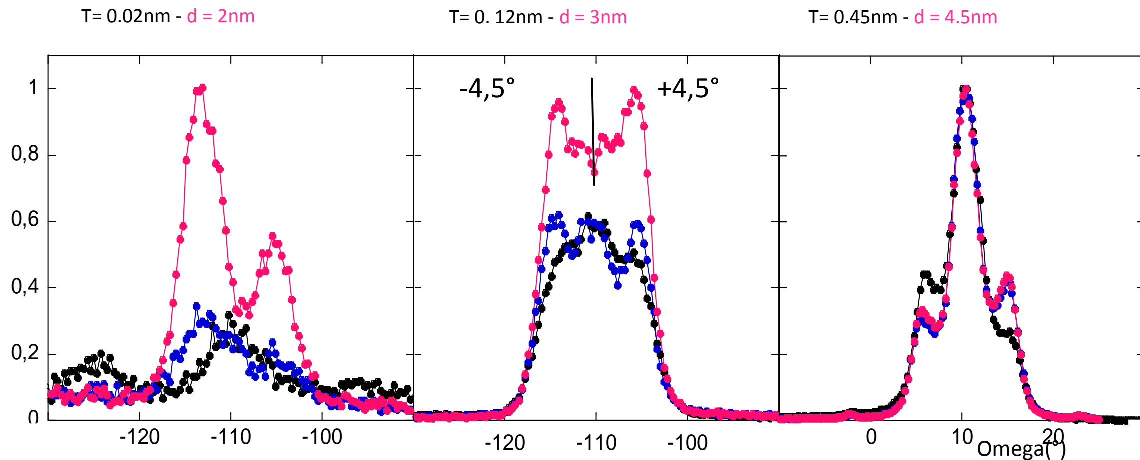

Figure 3 : Evolution of the diffracted intensity for an azimuth scan around an in-plane gold peak,(i) black curve : in UHV at Room temperature, (ii) blue one: under 20 mbar O_2 at 473K and (iii) pink : 20 mbar O_2 + 0.2 mbar CO at 473K .T is the equivalent gold thickness and d the diameter under the reactive mixture as deduced from GISAXS.

Electromigration dans des lignes de cuivre de 100nm : mesure in-situ par diffraction Laue

P. Bleuet, P. Gergaud, P. Lamontagne, Lise Doyen
CEA-DRT-LETI Grenoble, ST Microelectronics
MA-794

Le développement de lignes de cuivre de plus en plus fines conduit à des densités de courant de plus en plus fortes qui favorisent le transport de matière d'un bout à l'autre des lignes. Cette électromigration peut engendrer des défauts voire des ruptures dans les lignes de cuivre. Nous présentons ici les premiers résultats in-situ en diffraction Laue obtenus sur des lignes de cuivre fournies par St Microelectronics et dont la largeur est 100nm. Afin de favoriser l'électromigration et de la rendre compatible avec des temps de mesure raisonnables, les lignes ont été maintenues à une température constante (utilisation d'un four in situ) et ont été soumises à une circulation de courant également constante. Compte-tenu des dimensions, le signal reçu par la CCD est très faible, néanmoins nous avons pu mettre en évidence un décalage des tâches de Laue au fur et à mesure du temps qui pourrait être du à une rotation des grains sur eux-mêmes. Cette observation, spécifique aux lignes de cuivre très fines, est en accord avec de précédents travaux publiés par l'ALS. La faiblesse du signal rend particulièrement difficile le traitement des données en série ainsi que la détermination quantitative des déformations.
La prochaine campagne d'expériences acceptée par le comité de programme portera sur des mesures complémentaire en faisceau monochromatique. La mesure du tenseur de déformation complet permettra de déterminer les gradients de contraintes hydrostatiques à l'origine des ruptures de lignes.

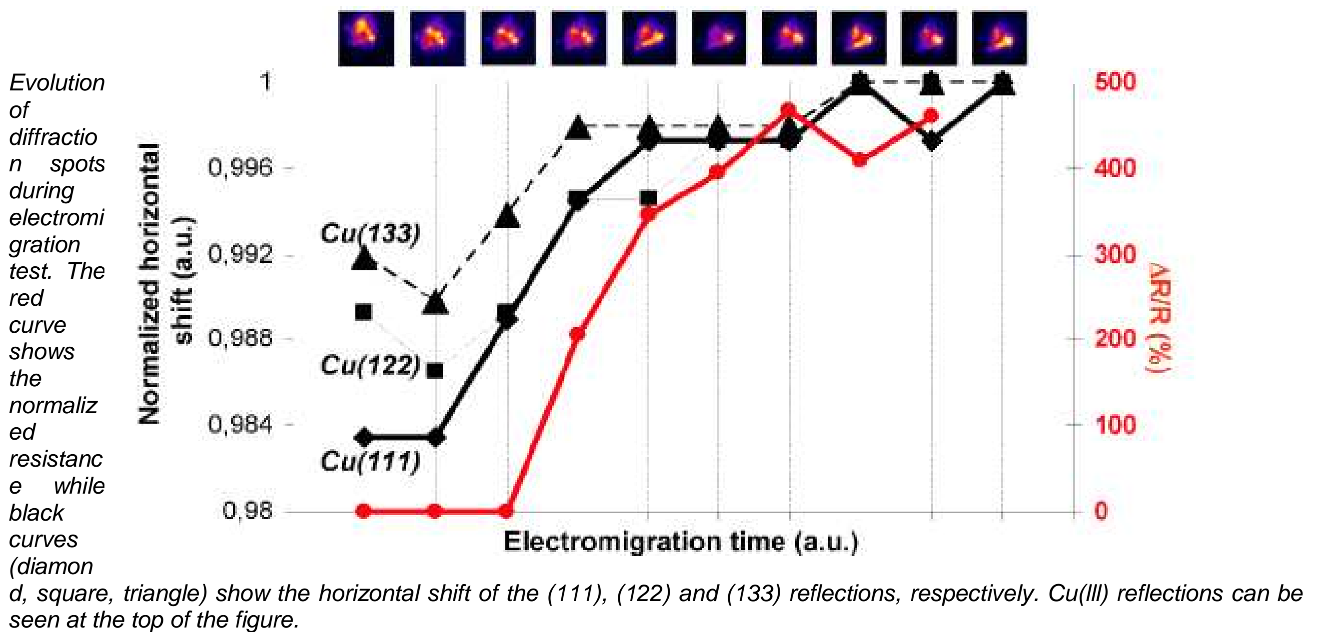

Evolution of diffraction spots during electromigration test. The red curve shows the normalized resistance while black curves (diamond, square, triangle) show the horizontal shift of the (111), (122) and (133) reflections, respectively. Cu(lll) reflections can be seen at the top of the figure.

Reference: P. Bleuet, L. Arnaud, X. Biquard, P. Cloetens, L. Doyen, P. Gergaud, P. Lamontagne, M. Lavayssière, J.-S. Micha, O. Renault, F. Rieutord, J. Susini and O. Ulrich
" Towards synchrotron-based nanocharacterization "
Proceeding of International Conference on Frontiers of Characterization and Metrology for Nanoelectronics, , AIP Conf. Proc. 1173, 181 (2009)

Determination of global and local residual stresses in SOFC by X-ray diffraction

J. Villanova, J.S. Micha, O. Sicardy

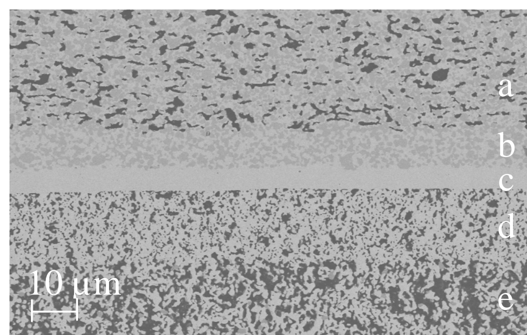

figure 1 : Scanning Electron Micrograph (SEM) of the section of a cell after manufacturing. (a) Anode-support: NiO + YSZ (Yttria-Stabilized Zirconia), (b) Anode Functional Layer: NiO + YSZ, (c) Electrolyte: YSZ, (d) Cathode Functional Layer: LSM (Sr-doped Lanthanum Manganite) + YSZ, (e) Cathode: LSM.

Solid Oxide Fuel Cell (SOFC) is a high-performance electrochemical device for energy conversion. A single cell is composed of 5 layers made of different ceramic materials: anode support, anode functional layer, electrolyte, cathode functional layer and cathode. The mechanical integrity of the cell is a major issue during its lifetime, especially for the electrolyte layer. Damage of the cells is mainly due to the high operating temperature, the “redox” behaviour of the anode and the brittleness of the

involved materials. Since residual stresses are known to play a significant role in the damage evolution, it is important to determine them.

For this purpose, residual stresses in an anode-supported planar SOFC were measured by X-ray diffraction. Firstly, macroscopic stresses in each phase of each layer were studied using the $Sin^2\psi$ method on a laboratory X-ray goniometer at room temperature. The electrolyte has been found under bi-axial compressive stress of -920 MPa. Secondly, X-ray measurements controlling depth penetration were made in the electrolyte using grazing incidence method. The results show that the stress is not homogenous in the layer. The first five micrometers of the electrolyte have been found less stressed (-750 MPa) than the complete layer, suggesting a gradient of strain in the electrolyte from the interface with the Anode Functional Layer to the free surface.
Local stress measurements were then made on the electrolyte layer by X-ray synchrotron radiation that allows high accuracy measurements on the (sub-) micrometer scale. These X-ray techniques at different scales will contribute to a better understanding of the residual stress in the electrolyte layer and thus to the involved damage mechanisms.

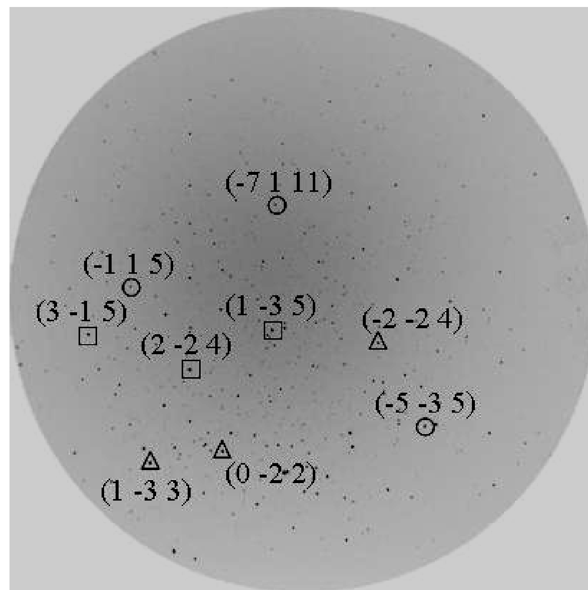

Figure 5: Laue pattern of a point scanned on electrolyte in white beam mode: open squares (resp. triangles and circles) represent reflexions indexed for the grain n°1 (resp. 2 and 3).

To analyze Laue patterns obtained with white beam measurements, calibration has been performed by using the Laue pattern of a reference sample, e.g. a <001> stress free Si single crystal. The deviatoric strain tensor values found using XMAS after calibration are lower than 10^{-4}. Taking into account the sensitivity of the method, the deviatoric strain tensor can be considered as equal to zero. These results are in agreement with the stress-free reference crystal hypothesis and validate the obtained calibration parameters for the next steps of the analysis.
The electrolyte and the anode are polycrystalline materials. The high energy part of the white beam crosses the electrolyte and reaches the AFL. The recorded CCD images contain bright spots due to diffraction by well crystallized electrolyte grains and numerous tiny spots coming from the AFL grains. A threshold image processing has been applied to eliminate these small peaks. A reliable methodology was set up to find the orientation of different grains in the CCD images. In each image, at least three grains have been identified (Fig.5). Since the scanning step was 1µm and the electrolyte grain size was around 5µm, each grain appears on several consecutive CCD images. Each grain probed at different locations was found to have the same orientation corresponding to the absence of

internal micro-misorientation in grain. Analysis over the entire area confirms that the electrolyte is a non-textured material.
The obtained stress tensors are consistent with global measurements i.e. grains are under strong compression state. For example, the stress tensor of a <-1 -3 5> oriented grain (along sample z axis) has been determined by combining of white and monochromatic measurements. The obtained stress tensor, expressed in the sample frame, is the following (Mpa):

$$\begin{pmatrix} -986 & -35 & 30 \\ -35 & -878 & 25 \\ 30 & 25 & -209 \end{pmatrix}$$

This preliminary study has been made on two targeted measurement points where four different stress tensors corresponding to four different grains have been calculated, showing that the stress state is not the same for each one. Additional measurements have been carried out to get more details on strain heterogeneities from grain to grain.

IV Surfaces/Interfaces/Croissance de Nanostructures *in situ*, en ultra-vide (SUV)

IV.1. Introduction

Personnel

L'équipe SUV (Surfaces Under Vacuum) était composée de deux chercheurs CEA (T. Schülli et G. Renaud), d'un chercheur CNRS (M.de Santis) et d'un ingénieur de recherche CNRS (H. Tolentino). Depuis le départ de Marion Noblet-Ducruet, le support technique sur SUV a été très insuffisant. L'aide trés active d'Olivier Geaymond et l'embauche pendant 9 mois d'un technicien à mi-temps en contrat de professionnalisation puis son embauche récente sous forme de CDD d'un an ont néanmoins permis de réaliser le plus gros du travail technique. L'instrument SUV, techniquement très complexe et demandant un suivi quotidien, nécessite le travail d'un technicien dédié, à plein temps ; il serait donc hautement souhaitable de stabiliser ce technicien sur un contrat CDI.

En outre, Tobias Schülli part à la fin de l'année 2009 à l'ESRF, pour prendre la responsabilité de la ligne ID01. Il est donc indispensable de prévoir un poste de chercheur (postdoc, CDD, CDI ?) pour le remplacer afin d'assurer d'une part le rôle de « local contact », d'autre part de poursuivre le projet de CBE in situ qu'il a lancé.

Développements

Les développements techniques déjà en cours l'année dernière, celui d'une nouvelle tête goniométrique et de nouvelles fentes, développées au SERAS, ont dû être mis en « stand-by » du fait d'un support technique insuffisant, et du remontage de SUV qui a mobilisé tout le personnel existant. Ces deux projets redémarrent seulement cette fin d'année, et devraient pouvoir être menés à bien au cours de l'année 2010, comme les travaux prévus d'amélioration de la chambre de caractérisation et ceux du support de la chambre principale.

IV.2. Scientific activities of the in situ instrument SUV 2009

In 2008/2009 the instrument was closed down for 6 months in order to increase the experimental hutch and prepare the installation of the UHV-CVD gas distribution system.
The reduced number of experiments nevertheless reflects the instruments user community and topics, confirming its importance as a unique in situ growth facility at the ESRF. On the contrary to other beamlines equipped with UHV sample preparation chambers, the SUV endstation comes closest to a full scale, versatile MBE system and thus is mainly claimed by user groups seeking to realize the growth of nanostructures, thus necessitating the (co-)deposition of several elements.

Furthermore, the instrument's success is guaranteed combining Grazing Incidence Small Angle X-ray Scattering (GISAXS) and Diffraction (GIXD) to access structural parameters on a vast length scale from subatomic distances to particles of 100 nm. It is especially the optimized mechanical elements inside the UHV chamber that allow for low noise GISAXS recording and

the extreme versatility of the chamber to connect multiple deposition sources that make the instrument attractive to our users.
The following experimental reports and the examples of two publication highlights of the recent months underline clearly the trend of growth of complex nanostructures and the in situ tracking of their functionality.

IV. 2. SUV highlights :

-1- A comprehensive review of the GISAXS technique used to probe the morphology and organization of surfaces, interface, thin films and nanostructures, has just appeared in Surface Science Reports. This invited review article presents the principles, the experimental aspects and a complete theoretical treatment of GISAXS, as well as all published results to date, including the in situ work in UHV during growth, developed by the authors.

Surface Science Reports 64 (2009) 255–380

Contents lists available at ScienceDirect
Surface Science Reports
journal homepage: www.elsevier.com/locate/surfrep

Probing surface and interface morphology with Grazing Incidence Small Angle X-Ray Scattering

Gilles Renaud [a,*], Rémi Lazzari [b], Frédéric Leroy [c]

[a] Commissariat à l'Energie Atomique, Institut Nanosciences et Cryogénie, Service de Physique des Matériaux et Microstructures, Nanostructures et Rayonnement Synchrotron, 17 Avenue des Martyrs, F-38054 Grenoble, Cedex 9, France
[b] Institut des NanoSciences de Paris, Université Pierre et Marie Curie (Paris 6), CNRS UMR 7588, Campus Boucicaut, 140 Rue de Lourmel, 75015 Paris, France
[c] Centre Interdisciplinaire de Nanoscience de Marseille, CNRS - UPR 3118, Campus de Luminy Case 913, 13288 Marseille Cedex 9, France

ARTICLE INFO

Article history:
Accepted 12 July 2009
editor: G. Thornton

Keywords:
X-ray scattering
Grazing incidence
Synchrotron X-rays
GISAXS
Grazing Incidence Small Angle X-Ray Scattering
Distorted Wave Born Approximation
DWBA
Local Monodispersed Approximation
Decoupling Approximation
Size-Spacing Correlation Approximation
Scaling Approximation
Theory of X-ray scattering
Form factor
Interference function
Assemblies of nanoparticles
In situ
Nano-particles
Nano-structures
Growth modes
Growth laws
Molecular beam epitaxy
Ultra-high-vacuum
Catalysis
Semi-conductors
Metal surfaces
Reconstructions
Self-organized growth
Patterned substrates
Polymers
Metal on oxide surfaces
Quantum dots

ABSTRACT

Nanoscience and nanotechnology are tremendously increasing fields of research that aim at producing, characterizing and understanding nanoobjects and assemblies of nanoobjects. Their new physical or chemical properties, which arise from confinement effects, intimately depend on their morphological properties, *i.e.* their shapes, their sizes and their spatial organization. This calls for dedicated morphological characterization tools, among which is the Grazing Incidence Small Angle X-Ray Scattering (GISAXS). This reciprocal space technique has emerged in the last two decades as a powerful tool that allows investigating in a non-destructive way the morphological properties from one to billions of nanoparticles, either on a surface, or embedded in a matrix, with sizes ranging from 1 nm to several microns. The advantages of the technique are that it is non-destructive; it yields statistical information averaged on a large number of nanoparticles; it allows probing both the surface or deep below it, by changing the incident angle of the X-ray beam; it can be used in very different sample environments, in particular *in situ* in the course of a given process such as growth, annealing, gas exposure; and it may be given chemical sensitivity by use of anomalous scattering.

This report presents a review of the GISAXS technique, from experimental issues to the theories underlying the data analysis, with a wealth of examples. The physical morphological information contained in GISAXS data and its analysis are presented in simple terms, introducing the notions of particle form factor and interference function, together with the different cases encountered according to the size/shape dispersion. The theoretical background of X-ray diffuse scattering under grazing incidence is presented in a general way, and then applied to the particular case of grazing incidence small angle X-ray scattering from assemblies of particles either on a substrate, or buried below it.

Most of the GISAXS measurements published to date are reported, covering the fields of *ex situ* studies of embedded metallic nanoparticles, granular multilayered systems, implanted systems, embedded or stacked or deposited semi-conductor nanostructures, porous materials and copolymer thin films. A special emphasis is brought on *in situ* experiments, performed either in ultra-high vacuum during nanoparticle growth by molecular beam epitaxy, or in gas-reactors during catalytic reactions. This covers a very broad field, from (i) the 3D island (Volmer–Weber) growth of metals on oxides surfaces to (ii) the organized growth of metals on surfaces that are nanopatterned either by surface reconstruction or by underlying dislocation networks or by deposit-induced nanofacetting, to (iii) the *in situ* investigation of the self-organized Stranski–Krastanow hetero-epitaxial growth of semi-conductor quantum dots on semi-conductor surfaces, or (iv) the *in situ* surface nanopatterning by ion bombardment. Many examples are discussed in detail, to illustrate the large diversity of systems and morphologies that can be addressed as well as the different analysis issues and the conclusions of the technique in terms of growth mode.
© 2009 Elsevier B.V. All rights reserved.

Contents

1. Introduction 258
2. X-ray techniques to probe density fluctuations near surfaces and buried interfaces 260

* Corresponding author. Tel.: +33 4 38 78 35 58; fax: +33 4 38 78 51 97.
E-mail addresses: grenaud@cea.fr (G. Renaud), lazzari@insp.jussieu.fr (R. Lazzari), leroy@cinam.univ-mrs.fr (F. Leroy).
URL: http://grenaud@cea.fr (G. Renaud).

0167-5729/$ – see front matter © 2009 Elsevier B.V. All rights reserved.
doi:10.1016/j.surfrep.2009.07.002

-2- A combined experimental-theoretical approach has been used to determined the complete 3D map ot strain and composition in 3D Ge sialnds grown on Si(001), nominal and patterned by lithography. This new approach has led to a publication in the Physical Review Letters.

PRL 102, 025502 (2009) PHYSICAL REVIEW LETTERS week ending 16 JANUARY 2009

Enhanced Relaxation and Intermixing in Ge Islands Grown on Pit-Patterned Si(001) Substrates

T. U. Schlllli,[1,*] G. Vastola,[3] M.-I. Richard,[1,2] A. Malachias,[2] G. Renaud,[1] F. Uhlík,[3] F. Montalenti,[3] G. Chen,[4] L. Miglio,[3] F. Schäffer,[4] and G. Bauer[4]

[1]CEA Grenoble, INAC/SP2M, 17 rue des martyrs, F-38054 Grenoble, France
[2]ESRF, Grenoble 6 rue J. Horowitz, F-38043 Grenoble, France
[3]L-NESS and Materials Science Department, University of Milano-Bicocca, Via R. Cozzi 53, I-20125 Milano, Italy
[4]Johannes Kepler Universität Linz, A-4040 Linz, Austria

(Received 24 October 2008; published 16 January 2009)

We compare elastic relaxation and Si-Ge distribution in epitaxial islands grown on both pit-patterned and flat Si(001) substrates. Anomalous x-ray diffraction yields that nucleation in the pits provides a higher relaxation. Using an innovative, model-free fitting procedure based on self-consistent solutions of the elastic problem, we provide compositional and elastic-energy maps. Islands grown on flat substrates exhibit stronger composition gradients and do not show a monotonic decrease of elastic energy with height. Both phenomena are explained using both thermodynamic and kinetic arguments.

DOI: 10.1103/PhysRevLett.102.025502 PACS numbers: 81.16.Nd, 61.46.−w, 71.15.Pd, 81.07.−b

Ordering, shape and size uniformity of epitaxial Ge (or SiGe) islands on Si(001) is very important whenever microelectronic applications based on such nanostructures are concerned [1]. Island formation is known to follow the Stranski-Krastanow (SK) growth mode [2], allowing for partial elastic energy relaxation. Significant intermixing between Si and Ge within the islands has been reported [3–8], and the role of alloying for growth has been theoretically investigated [9–13]. Since on flat substrates islands tend to nucleate randomly, substrate patterning can be used to achieve controlled positioning [14]. Remarkably, patterning was also shown to increase size uniformity, possibly because of a more regular distribution of capture areas [15]. The growth of ordered nanometric islands with a narrow distribution in shape and size is already exciting *per se*, but recent results [15,16] indicate that the influence of patterning can be even more far reaching. Self organized patterning in ultrahigh vacuum (UHV) may also be used in the future, in order to control size and relaxation in SiGe islands [17]. We recall that SiGe islands on Si are coherent up to a critical volume V_c, characteristic for the onset of the formation of misfit dislocations [18]. In Ref. [15], it was demonstrated that patterning of Si(001) extends the allowed volume range for coherent islands. According to atomistic and finite element method (FEM) calculations reported in the same paper, this can be explained by an extra relaxation, caused by the pit, which lowers the substrate or island misfit. The possibility of controlling also the relaxation level of the islands by growth on patterned substrates appears extremely intriguing. In this Letter, we report an experimental proof of the abovementioned effect, and we show that the pits influence both, average relaxation and distribution of Ge within the islands.

Pit-patterned substrates were prepared by lithography, following the procedure used in [19]. Seven ML of Ge were deposited at 650Å °C on a Si(001) substrate with a 900 × 900 μm^2 part of it being patterned with pits at a periodic spacing of 495 nm. The growth of a Si buffer prior to Ge deposition leaves periodic downward pyramid-shaped {1110} pits [19]. The sample was transferred under N_2 atmosphere into the UHV chamber of beam line BM32 at the ESRF in Grenoble. AFM analysis shows that Ge islands nucleate at the bottom of these pits and form dome-shaped islands with identical facets as on the flat part of the substrate. The average island density per surface unit area is 5 μm^{-2} for the patterned part and 20 μm^{-2} for the flat one. The domes on the patterned (flat) part have an average height of 28 nm (23 nm) and a diameter of 130 nm (110 nm).

The islands were characterized by grazing incidence x-ray diffraction (GIXD) at an x-ray energy of 11.04 keV. The incident beam and the collimation on the detection side were translated in order to select between patterned and flat regions. Reciprocal space maps in the vicinity of the (400) Bragg reflection were recorded, as shown in Figs. 1(a) and 1(b) together with corresponding AFM images (insets). The intensity distribution along the radial direction clearly extends to higher lattice parameters for the patterned region. The islands grown on the flat have their main lattice parameter around 5.465 Å (in reciprocal lattice units of $H = 3.975$) whereas for the patterned part, the lattice parameters are stretched in reciprocal space, showing a maximum at ∼5.51 Å ($H = 3.943$).

To understand the observed differences, we related the lattice-parameter to the local Ge content inside the islands by exploiting anomalous x-ray scattering. By monitoring the scattered intensity when varying the x-ray energy in the vicinity of the Ge K edge ($E_e = 11.103$ keV) at a fixed momentum tranfer Q, the corresponding average Ge concentration can be determined, so that in-plane lattice parameter $a_\parallel$ vs Ge content (c_{Ge}) data are extracted without any model assumption [5,20]. It is found that for the islands

 © 2009 The American Physical Society

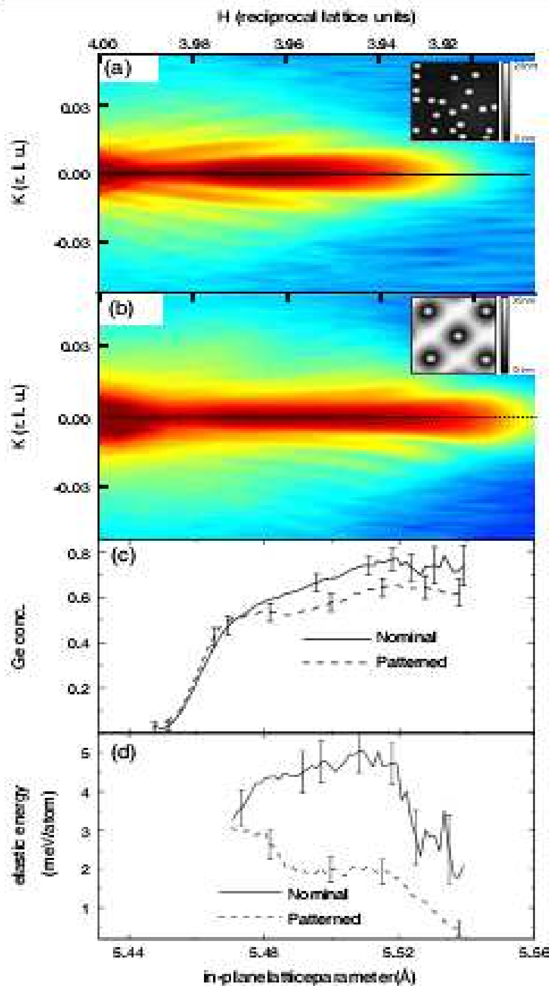

FIG. 1 (color online). Logarithmic intensity distribution in the vicinity of the (400) Bragg reflection for Ge islands grown on the flat (a) and patterned (b) sample part. Corresponding AFM images (1 μm^2 in size) are shown as insets. (c) Ge content inside the islands as a function of lattice parameter for growth on the flat (full line) and on the patterned part (dashed line). (d) elastic energy as a function of lattice parameter as extracted from the x-ray data. All figures correspond to the same lattice-parameter scale.

grown on the flat, the maximum Ge concentration for highest lattice parameters is slightly higher than for the patterned case [Fig. 1(c)]. However, as visible from the intensity distribution in Figs. 1(a) and 1(b), these relaxed regions contribute little to the total diffracted intensity. The combined analysis of the x-ray size oscillations, and the island shape as resolved by AFM, yield that the major part of the island volume is situated at lattice parameters below 5.48 Å for islands on the flat. Combining x-ray diffraction and AFM, the mean Ge content is determined to be $c_{Ge} \simeq (60 \pm 5)\%$ for both island types. Hence, the presence of the pits does neither influence the shape nor the mean SiGe composition of the islands. Let us see where, instead, differences exist. Figure 1(c) shows c_{Ge} vs $a_{\parallel}$ for the flat (full lines) and the patterned region (dashed lines). The continuous broadening of H-constant profiles for lower H values points to a monotonic lattice parameter increase as a function of height in the islands [21]. The flatness of the dashed curve indicates lower gradients for c_{Ge} inside the islands grown in pits in comparison to the flat case. It is thus clear that the elastic energy at comparable c_{Ge} must be significantly lower for islands nucleating in the pits, as the intensity in reciprocal space stretches out to much higher lattice parameters. The volumetric elastic energy can be extracted from these data, as performed in Refs. [7,20]. It is plotted as a function of lattice parameter in Fig. 1(d). In the narrow region that forms the interface between island and substrate, and hence the region where the in-plane strain $\epsilon_{\parallel}$ changes sign from expansive to compressive nature, our method does not allow for a precise determination of the elastic energy since regions with similar lattice parameter and slightly different composition will have a mean $\bar{\epsilon}_{\parallel}$ that amounts to zero. However, with the elastic energy $E_e \propto \epsilon_{\parallel}^2$, its mean value does not average to zero. In the region of validity, our method yields a remarkable decrease of elastic energy throughout the islands grown on the pit-patterned part. One has to state that such x-ray measurements carry information on the in-plane lattice parameter, but effects of local hydrostatic compression cannot be taken into account when determining the elastic energy directly from the data.

More insights can be gained by extracting the actual 3D Ge distribution and the elastic-energy profile throughout the island. Over the last ten years, x-ray methods have been developed, coupling lattice parameter with lateral size [21] and chemical composition of an object, to reconstruct a concentration profile inside nanostructures [4,5,22]. These methods are limited, however, by model assumptions concerning the shape of the considered isostrain regions. A combination of x-ray methods and FEM calculations is thus necessary in order to overcome the lack of experimentally accessible information. We have used a fitting procedure that exploits a FEM-based treatment of nonuniform concentration profiles, to determine the local Ge content without any constraint. After the island and substrate geometry is created based on AFM images, nonuniform concentration values are assigned on a discrete mesh [13]. The elastic problem is then solved exploiting linear interpolation, (c_{Ge}, $a_{\parallel}$) data are extracted, and the statistical χ^2 is evaluated by comparison with the corresponding x-ray data. Using an iterative procedure based on local concentration exchanges, χ^2 is minimized. Technical details on the way we handle nonuniform distributions within FEM can be found in [13] where the elastic energy was

minimized. In the present work, the deviation from the experimental data is minimized. It is important to emphasize that particular care is required in assigning the correct statistical weight to the data. During the fit, (c_{Ge}, $a_{\|}$) pairs from the FEM grid were computed from the island interior and from a surrounding region in the substrate with a lateral extension inferred from the experimental island density, and a depth of 12 nm, i.e., the estimated penetration depth of the x-rays in our setup. This allowed us to filter out the substrate contribution from the experimental data which, as shown in Fig. 1(c) for the flat case, causes a sudden drop of the average Ge content at low lattice parameters, due to the strong scattering contribution from the Si-substrate. From the x-ray data, it is thus difficult to analyze the region of the substrate-island interface. Another difficulty stems from the vanishing experimental scattering volume of the regions with lattice parameters close to bulk Ge. In the fit shown in Fig. 2, the local value of c_{Ge} was extrapolated from experiments, assigning a large error bar in order not to bias the region where real data were present. Finally, a satisfactory fit (requiring $\sim 10^4$ iterations) is obtained, the full solution of the elastic problem being required at each step. The FEM fitted data (small dots in Fig. 2) show that several concentration values can be associated with a single value of lattice parameter, which is not obvious from the experimental curve which averages them out.

The 3D compositional maps corresponding to our best fits are displayed in Figs. 3(a)–3(d) together with their horizontally averaged values [Fig. 3(e)], while the elastic energy per atom is reported in Fig. 3(f), where a comparison with the uniform composition case is also shown. In the flat case—Figs. 3(a) and 3(b)—an almost pure Si region is found close to the base edges, a result fully compatible with selective-etching data [23]. From Figs. 3(c) and 3(d), one sees that Si enrichment at the base is less evident in the pit case where the overall Ge distribution is more uniform, but for more localized irregularities. This is particularly evident from the horizontally averaged c_{Ge} values displayed in Fig. 3(e). The different Ge distribution of the island apex along the [100] and [110] cross sections is due to the fact that the island boundary is composed by a set of facets and edges which is different for the two sections. It has thus a direct influence on the local elastic relaxation and hence the Ge concentration profile [24]. The above observations can be justified using both thermodynamic and kinetic arguments. The edges of the islands grown on flat substrates are the most compressed regions in case a uniform Ge distribution is considered [25], so that replacing Ge with Si atoms produces significant relaxation. Comparing the elastic energy in flat vs pit-patterned substrates [Fig. 3(f)] in the case of a uniform distribution, one sees that the driving force for Si segregation at the island base is weaker in pits, since the energy difference between base and top is smaller. Entropy of mixing could then prevail over elastic relaxation, forcing enhanced intermixing. While this thermodynamic argument supports our

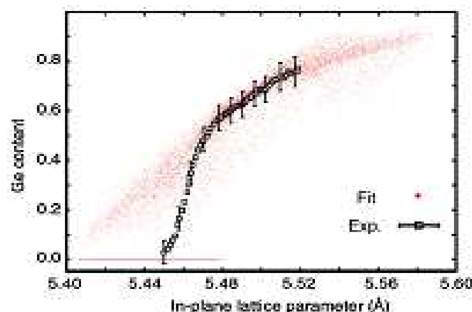

FIG. 2 (color online). Experimental data of the Ge-content as a function of lattice parameter together with FEM fitted data after proper separation of the Si substrate contribution (flat case).

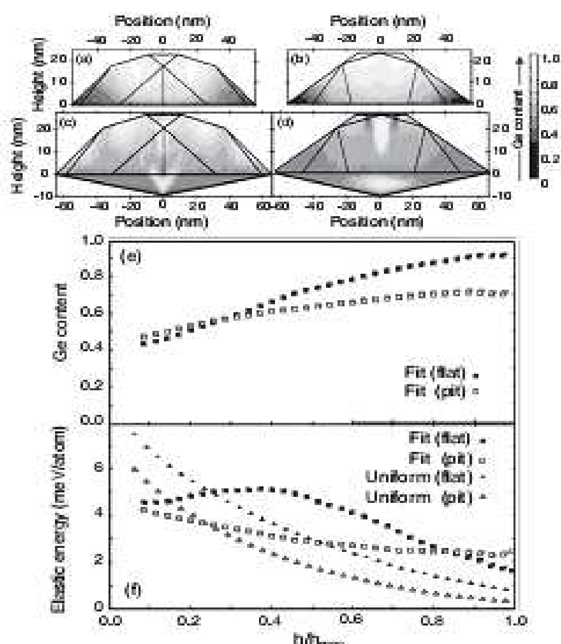

FIG. 3. Cross section map of the 3D-reconstructed Ge content profile for islands grown on flat (a), (b) and patterned (c), (d) samples. Sections are shown along the [100] (a), (c) and the [110] (b), (d) crystallographic directions. Panel (e) displays the average Ge content as a function of height. Panel (f) reports the elastic energy profile corresponding to the fitted Ge distribution on flat (filled box) and patterned (empty box) substrates. Plots made for the case of uniform concentration are analogously displayed for flat (filled triangles) and pit (empty triangles) case. The quantity h/h_{max} is a normalized height to allow the proper comparison between both island types at every height h.

results, it is important to consider that during growth, kinetic limitations are present, so that one should always check whether the proposed scenario is favored or simply made possible by plausible kinetic paths. On flat substrates, large amounts of Si become available during growth when the strong compressive stress at the edges produces trenches penetrating the Si substrate [26]. These Si atoms coming out close to the island periphery could easily be incorporated in the regions which are most favorable from the energetic point of view. As a result, the final profile resembles the minimum-energy one [13]. In the initial stages of growth, trenches are not yet present, providing a kinetic justification for the limited lateral extension of the external Si-rich region. Our results do not confirm the formation of a central Si-rich region ([4,7]), whose presence seems to be difficult to explain from both the thermodynamic and kinetic point of views. In pits, the Si-supply mechanism could be different. In Ref. [27], data collected on pit-patterned samples similar to ours indicated that the condition of a perfect WL completed prior to island formation is not fulfilled. Since preliminary results on the present samples confirm this observation, we believe that in pits, enhanced Si supply prior to trench formation is possible, i.e., from detachment of uncovered Si atoms from the steps of the pits' facets. These could reach the growing islands by surface diffusion, leading to a more uniform intermixing profile.

Let us now analyze quantitatively the main differences between the flat and the patterned case in terms of elastic energy. From Fig. 3(f), one sees that the presence of the pit allows for a significant decrease ($\sim 30\%$ on average) in elastic energy. Since this effect is confirmed also for uniform Ge distributions [triangles in Fig. 3(f)], the key role must be played by the different geometry. Before island formation, the pit is filled by Ge forming an inverted pyramid. This redistributes the load between Ge and the surrounding Si resulting in better strain relaxation with respect to a flat WL so that islands on pits nucleate on a substrate with a lower effective misfit. This relaxation mechanism was demonstrated in [15]. Additionally, the behavior of the elastic energy shows that the usual picture of a base-to-top stress relaxation breaks down in the case of a flat substrate [25]: the curve displayed in Fig. 3(f) clearly displays a maximum. Combining this with Fig. 3(e), one sees that Si enrichment at the base guarantees a lowering of the elastic energy. As soon as c_{Ge} approaches its average value (at around $h/h_{max} = 0.3$), elastic-energy lowering becomes less efficient: the strong elastic load determined by the high Ge content cannot be relieved by the limited deformation in regions still close to the base. In the proximity of the island top, instead, the elastic energy is nicely lowered in spite of the maximum Ge content in the island.

If prepatterning is already seen as a powerful tool to control positioning and homogeneity of heteroepitaxial islands, we have shown that it also allows one to control elastic-energy release and thus to grow islands with the desired relaxation. The kinetics of Si supply seems to be also influenced by the pit, calling for further studies for achieving full control.

Financial support by the EU-funded project "D-DotFET" and the FWF (Vienna, project SFB025) and GMe (Vienna) are gratefully acknowledged, together with technical help received from R. Gatti.

*schulli@esrf.fr

[1] F. Schäffler, Semicond. Sci. Technol. 12, 1515 (1997).
[2] V. A. Shchukin and D. Bimberg, Rev. Mod. Phys. 71, 1125 (1999).
[3] G. Capellini, M. De Seta, and F. Evangelisti, Appl. Phys. Lett. 78, 303 (2001).
[4] A. Malachias et al. Phys. Rev. Lett. 91, 176101 (2003).
[5] T. U. Schülli et al., Phys. Rev. Lett. 90, 066105 (2003).
[6] G. Medeiros-Ribeiro et al., Appl. Phys. A 80, 1211 (2005).
[7] G. Medeiros-Ribeiro and R. S. Williams, Nano Lett. 7, 223 (2007).
[8] A. Rastelli et al., Nano Lett. 8, 1404 (2008).
[9] C. Lang, D. J. H. Cockayne, and D. Nguyen-Manh, Phys. Rev. B 72, 155328 (2005).
[10] G. Hadjisavvas and P. C. Kelires, Phys. Rev. B 72, 075334 (2005).
[11] Y. Tu and J. Tersoff, Phys. Rev. Lett. 98, 096103 (2007).
[12] N. V. Medhekar, V. Hegadekatte, and V. B. Shenoy, Phys. Rev. Lett. 100, 106104 (2008).
[13] R. Gatti, F. Uhlík, and F. Montalenti, New J. Phys. 10, 083039 (2008).
[14] Z. Zhong and G. Bauer, Appl. Phys. Lett. 84, 1922 (2004).
[15] Z. Zhong et al., Phys. Rev. Lett. 98, 176102 (2007).
[16] H. Hu, H. J. Gao, and F. Liu, Phys. Rev. Lett. 101, 216102 (2008).
[17] G. Katsaros et al., Phys. Rev. Lett. 101, 096103 (2008).
[18] A. Marzegalli et al., Phys. Rev. Lett. 99, 235505 (2007).
[19] G. Chen et al., Phys. Rev. B 74, 035302 (2006).
[20] R. Magalhaes-Paniago et al., Phys. Rev. B 66, 245312 (2002).
[21] I. Kegel et al., Phys. Rev. Lett. 85, 1694 (2000).
[22] A. Letoublon et al., Phys. Rev. Lett. 92, 186101 (2004).
[23] G. Katsaros et al., Phys. Rev. B 72, 195320 (2005).
[24] In Figs. 3(c) and 3(d), the calculations show Ge rich regions of the pit bottoms which do not appear in 3(e). In this figure, we make the comparison between the average composition between islands on flat and patterned substrates. Since the material at the bottom of the pit is of course not present in the island on flat substrate, the averaged compositions of Fig. 3(e) do not take into account this volume.
[25] G. Vastola, R. Gatti, A. Marzegalli, F. Montalenti, and Leo Miglio, *Detailed Analysis of the Shape-Dependent Deformation Field in 3D Ge Islands on Si(001)* (Springer, Berlin, 2008), pp. 421–438.
[26] S. A. Chaparro, Y. Zhang, and J. Drucker, Appl. Phys. Lett. 76, 3534 (2000).
[27] T. Stoica et al., Nanotechnology 18, 455307 (2007).

IV. 3. SUV : selected scientific results

-Dewetting dynamics of strained-silicon on insulator (sSOI) by GISAXS and GIXD

F. Leroy, F. Cheynis, T. Passanante, E. Bussmann, P. Müller and J. Eymery

The purpose of this experiment was to study *in situ* the dewetting kinetics of thin Si(001) films on SiO_2. Dedicated samples based on the SOI (silicon on insulator) technology have been studied. The key parameters of this dewetting transition are temperature and film thickness. More particularly it has been proposed that Si nanocrystals agglomeration during dewetting is a stress-driven morphological instability caused by the thermal expansion mismatch between Si and SiO_2. In order to put in evidence the potential role of interfacial stress we used samples fabricated on the basis of the recent strained silicon-on-insulator (sSOI) technology. This technology allows tuning the lattice parameter of the Si film from 0 to +1.2% on the same SiO_2 amorphous material. Grazing Incidence Small Angle X-ray Scattering and Grazing Incidence X-ray Diffraction (GIXD) measurements have been performed in real-time in order to characterize the structure and the morphology of the Si thin film before and during dewetting.

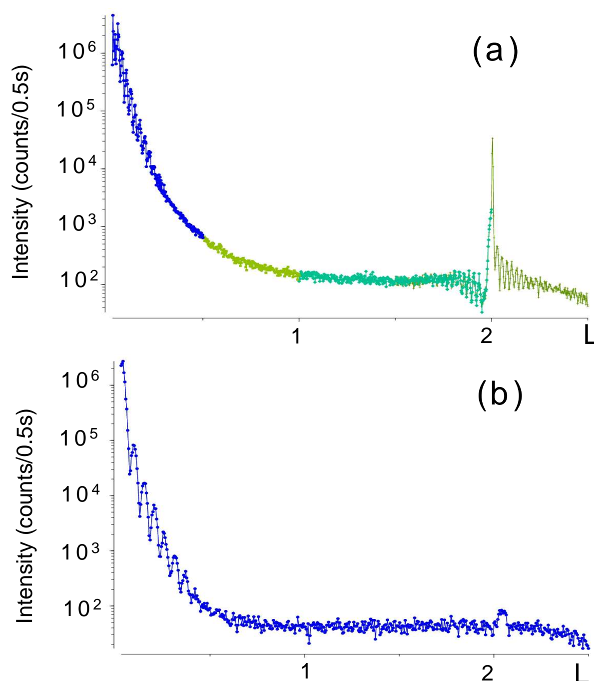

Fig.1 (22L) scans for (a) unstrained and (b) 0.8%-strained Si thin films. Kiessing fringes provide an accurate value of the Si thickness (resp. 20.6 and 9.2 nm.)

First the Si(100) surface of SOI and sSOI substrates have been cleaned *ex situ* by standard chemical etching ('shiraki' cleaning) followed by a final cleaning (mixture of $HCl:H_2O_2:H_2O$, 3:1:1) to protect the surface with a thin (1-2 nm) oxide layer before introducing the sample in UHV. Then the thin oxide layer has been removed in the main chamber increasing slowly the temperature up to 900℃. This desoxydiza tion procedure has been checked in real-time by RHEED looking at the appearance of the Si(1x2) surface recontruction. This has been confirmed by GIXD showing a clear in-plane signal from the (1x2) reconstruction typically observed in the case of a flat Si surface.

After desoxydization we have characterized the Si film on the different SOI samples (thickness, strain state). Out-of-plane scans have been performed giving rise to Kiessing fringes nearby Bragg peaks providing an accurate measurement of the thickness of the Si films before dewetting (see Fig.1). The mean strain state of strained Si samples could also be obtained with great precision from the in-plane and out-of-plane position of the Bragg peaks. The Bragg peaks are not only shifted compared with the underlying Si wafer but also broader showing that the strain state of the film is not homogeneous.

The kinetics of dewetting has been studied alternating GISAXS and GIXD measurements on three different samples: unstrained Si (20 nm thick), 0.8%-strained Si (9 nm thick) and 1.2%-strained Si (10 nm thick). Fig.2 displays for instance the evolution of GISAXS and GIXD as function of time for the 1.2% strained Si film.The appearance of tilted scattering rods on GISAXS patterns is a clear indication of the agglomeration of the film into Si nanocrystals exhibiting extended (113) facets and smaller (111) facets. Changing the sample azimuth by 45° it has been

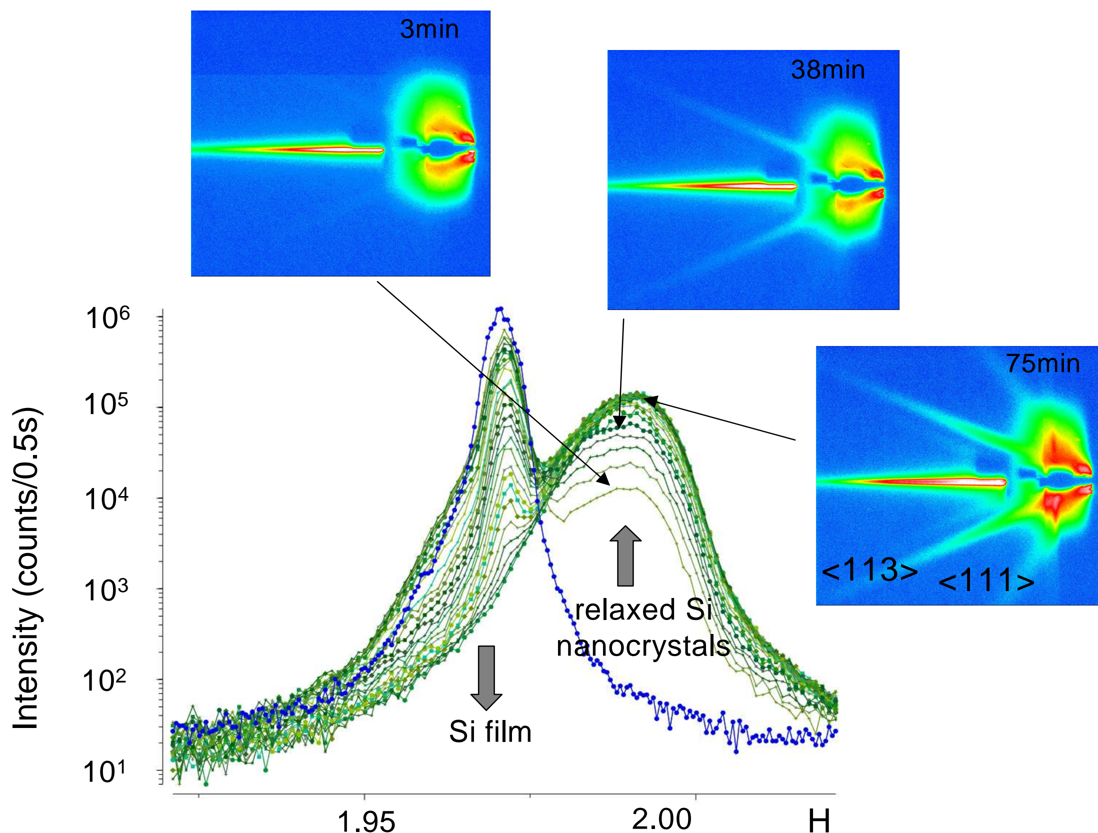

Fig. 2. Overview of the evolution of GISAXS (beam aligned along <110>) and GIXD (scan along (hh0)) as function of time during dewetting of a 1.2%-strained Si film at 950°C. The dewetting starts by the appearance of a bump at (220) corresponding to relaxed Si nanocrystals. Simultaneously, extended strikes arising from <113> and <110> facets appear on the GISAXS patterns. The intensity of this bump from Si nanocrystals increases while the Si film Bragg peak decreases. The time scale for complete dewetting is about 1h.

shown that nanocrystals exhibit also (110) facets. Simultaneous measurements of radial scans by GIXD indicate that the Si film stress relaxes immediately and completely as nanocrystals are formed during dewetting. At the end of dewetting we completed the GIXD and GISAXS results by mapping in-plane the reciprocal space around (220) Bragg peak and by measuring the full 3D reciprocal space around (000) by GISAXS rotating the sample by step of 1° over 90°. No other facets have been detected.

Interestingly out-of-plane scans reaveled that forbidden reflexions like (222), (442) and (420) are measurable (see for instance Fig.1a at L=2). This effect is usually asigned to an asymmetric charge distribution of Si due to covalent bonding of valence electrons or anharmonicity of the thermal vibrations. However in our case additional effects should be considered arising from the Si/ SiO_2 interface and from the strain state which can break the symmetry of the nearest neighbour boundings. Qualitative understanding of the Si thin film structure and interface can be gained from this data set. More quantitative measurements of the CTRs should be necessary to characterize precisley the Si thin film and interface structure.

In summary sample preparation and dewetting of SOI and sSOI have been well reproduced on the SUV apparatus. GISAXS and GIXD measurements have been alternatively performed *in situ* and in real time (steps of 3 min) providing a detailed characterization of the evolution of Si nanocrystal facets and internal relaxation. Dewetting of Si/SiO_2 gives also rise to very anisotropic organization of the nanocrystals as observed by *ex situ* AFM. However, this could not be observed by GISAXS due to the large length scale of the dewetted structures (100nm - 1µm). From GIXD we have also obtained a qualitative characterization of the interface structure for unstrained and strained Si samples. Detailed calculation of the interface structure must now be performed to compare with our results. This is part of our ANR-PNANO DEFIS project in collaboration with theoreticians of CINaM (P. Ganster, G. Tréglia). From the GISAXS and GIXD characterizations after dewetting we can fully determined the morphology (facets) and the internal relaxation of the nanocrystals. The broadness of the Bragg peaks of the nanocrystals is a clear indication that Si nanocrystals are completely relaxed on average but many different strain states still exist after complete dewetting.

- In-situ nucleation of Si-wires, MBE growth and liquid Au-catalysts

T. U. Schülli, G. Renaud

Following first publications on the x-ray investigation of nanowires, fundamental questions on their growth as the formation of defects or twinning, maybe addressed by in situ investigation of early nucleation stages. We have followed the deposition of a thin Au film and the formation of catalytic droplets during annealing, as well as the nucleation of si nanowires bi subsequent MBE deposition of Si.
After the deposition of a thin Au-film on Si(111), its crystallinity was studied and a preferential orientation, parallel to the cubic axes of Si was found. Upon annealing, islands are formed prior to melting. This could be followed in situ by monitoring the width of the Au(113) as shown in Fig. 1: for a thin layer, and scanning in q_z direction in reciprocal space (here q_z is parallel to the substrate's surface normal), broad size oscillations are visible. Their spacing can be attributed to the 1.8 nm thick film as deposited at room-temperature. Upon annealing at 350℃, Islands were formed, witnessed by the narrowing of the Au (113) peak as visible in Fig. 1 (b). At 360° C, all crystalline signals from Au disappear and a eutectic AuSi liquid is formed.

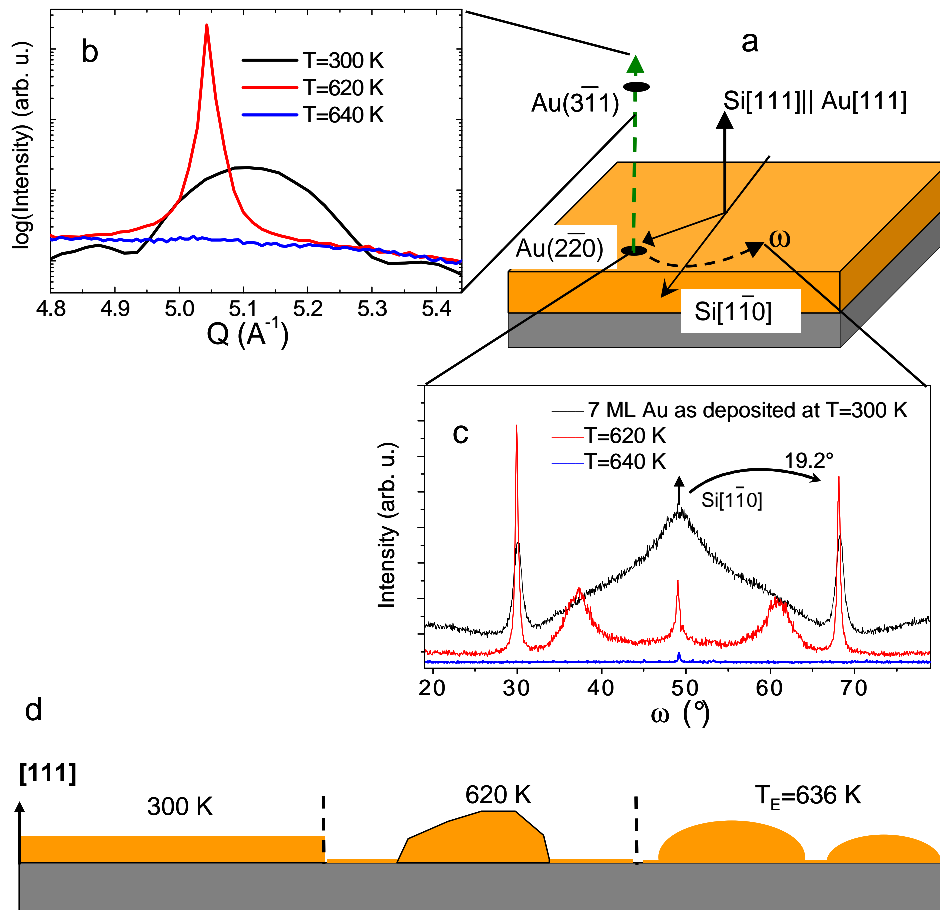

Figure 1: **a**, Sketch of different characterization scans that where used to follow the evolution of the Au crystal structure during annealing.

b, Scan along the surface normal of the film, crossing the $(3\bar{1}1)$ Bragg point. Its half width is inversely proportional to the thickness of the regarded crystallites. After deposition at room temperature size oscillations confirm the film thickness to be ~1.6 nm, as calibrated. Upon annealing at 620 K, 20 nm high crystalline Au islands form. At 640 K all crystalline signals disappear.

c, The crystallographic orientation in the plane was studied by rocking scans on the Au$(2\bar{2}0)$ peak, proving that the $[1\bar{1}0]$ axis of Au is oriented preferentially along the Si$[1\bar{1}0]$ direction. Upon annealing, an in-plane rotation of 19.2º is found, to the preferred epitaxy $[1\bar{1}0]$Au(111)||$[2\bar{3}1]$Si(111), as well as a growth of these crystallites in size. Above the eutectic temperature of 636 K, the islands "melt" *via* the formation of the $Au_{81}Si_{19}$ eutectic.

d, Graphical representation of the different annealing steps followed in (B) and (C). The formation of islands happens prior to melting.

Surface induced giant supercooling in AuSi catalysts

T. U. Schulli, R. Daudin, G. Renaud, A. Vaysset, A. Pasturel

The rapidly developing field of vertical Semiconductor nanowire growth makes use of metal catalysts combined with chemical vapour deposition. It is essentially the formation of low temperature eutectics between semiconductors and metal that drives the nucleation and growth of these structures. For Silicon nanowires, previously deposited metallic nanoparticles, Au as the most commonly used, serve as catalysts and offer unique growth conditions and restrictions due to their capacity of transporting Si even at low temperatures in the eutectic liquid $Au_{80}Si_{20}$. As research is focusing on alternative catalysts, an atomistic understanding of the outstanding transport properties of Si in AuSi even at massive Si overpressure in the growth chamber remains unresolved.

We have the melting behavior and the liquid state of these AuSi droplets on a Si(111) surface by Grazing Incidence X-ray Scattering on the BM32 beamline. It is found that in case of the formation of a complex Si(111)-(6x6) surface reconstruction, supercooling down to 120 K below the melting point (of only 636 K) is observed. A detailed analysis of the surface structure shows that more then 50 % of the surface atoms form pentagonal structures, incompatible with the fcc solid state of Au, but corresponding to the theoretical atomic arrangement and distances present in a calculated icosahedral AuSi "molecule" as it could exist in a liquid. Modification of the thermal history leaves a (3x $\sqrt{3}x\sqrt{3}$ R30° surface reconstruction and does not reveal the same supercooling effect. We state that this is the first observation of stabilization of a liquid in interaction with a surface. It confirms the theory that supercooling of metals is induced by local five fold symmetry. Figure 1 (a) shows the atomic positions of the Au atoms in the surface unit-cell obtained from the analysis of 976 measured reconstruction peak intensities. The red lines are a guide to the eye for the deformed pentagonal atomic arrangement of Au atoms around a threefold center. The atomic distance of the Au atoms in these pentagons is 0.284 nm, corresponding to the atomic distances observed in e.g. an icosahedral $Au_{12}Si$ molecule. Our findings are of fundamental interest in the understanding of liquid-solid interaction, as well as on the stabilities of liquids and the local arrangement of binary liquids. The solid-liquid transition could be observed by the appearance/disappearance of Bragg peaks of the Au fcc structure as well as by the observation of the liquid structure factor. Figure 1(b) shows the hysteresis opening due to the supercooling of the melt. Depending on the interface structure, the solidification temperatures differ by 40 K.

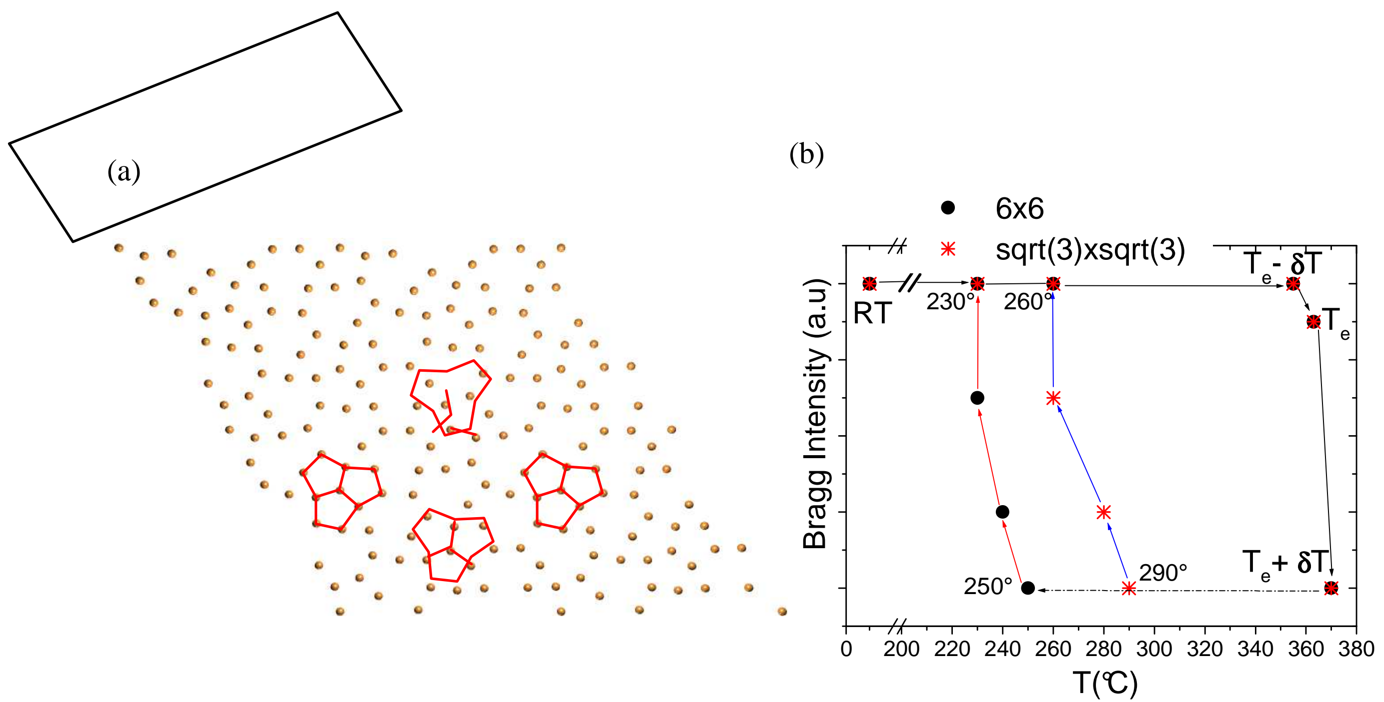

Fig. 1(a): Arrangement of the Au atoms on the Si(111) 6x6 reconstructed surface. The hexagonal unit cell with a=2.3 nm is indicated in black; in red: pentagonal arrangement of Au atoms around a threefold centre.
Fig. 1(b): Hysteresis of the solid-liquid-solid (s-l-s) transitions of the AuSi catalysts on the Si(111)6x6 and sqrt(3)xsqrt(3) surfaces . Note that the transition is accompanied by a chemical mixing (s-l) and de-mixing (l-s).

Enhanced relaxation and intermixing in Ge islands grown on pit-patterned Si(001) Substrates

T.U. Schülli, M.I. Richard, A. Malachias, G. Renaud, F. Uhlik, G. Vastola, F. Montalenti, G. Chen, L. Miglio, F. Schäffler, G. Bauer

Ordering, shape and size uniformity of epitaxial Ge (or SiGe) islands on Si(001) is very important whenever microelectronic applications based on such nanostructures are concerned . Island formation is known to follow the Stranski-Krastanow (SK) growth mode, allowing for partial elastic-energy relaxation. Since on flat substrates islands tend to nucleate randomly, substrate pre-patterning prior to growth can be used to achieve controlled positioning. A high degree of ordering was indeed obtained in, exploiting a suitably pit-patterned substrate. Remarkably, patterning was also shown to increase size uniformity, possibly because of a more regular distribution of capture areas. The possibility of controlling also the relaxation level of the islands by growth on patterned substrates appears extremely intriguing. we show that the presence of pits influences not only the average relaxation, but also the distribution of Ge within the islands. Pit-patterned substrates were prepared by lithography. 7 ML of Ge were deposited at 620℃ on a Si(001) substrate with a 900x900 µm² part of it being patterned with pits at a periodic spacing of 495 nm. The growth of a thick Si buffer prior to Ge-deposition leaves a periodically facetted surface with flat {1 1 10} pits with the shape of downward pyramids. AFM analysis showed that Ge islands nucleate at the bottom of these pits and form dome-shaped islands with identical facets as on the nominal part of the substrate. The average island density per surface unit area is 5 μm^{-2} for the patterned part and 20 μm^{-2} for the nominal one. The domes on the patterned (nominal) part have an average height of 28 nm (23 nm) and a diameter of 130 nm (110 nm).
The sample was then transferred under N_2 atmosphere and introduced in the UHV chamber at BM32. The islands were characterized in grazing incidence x-ray diffraction (GIXD) at an x-ray energy of 11.04 keV. The incident beam and the collimation on the detection side were

translated on the sample in order to select between the different regions. Reciprocal space maps in the vicinity of the 400 Bragg reflection were recorded as shown in Fig. 1 (a) and (b) together with corresponding AFM images as insets. The intensity distribution along the radial direction clearly extends to higher lattice parametres for the patterned region. In Fig. 2 (a) radial scans (corresponding to the full or dotted lines in Fig.1 (a) and (b) are plotted as a function of the lattice parameter, inferred from the radial momentum transfer. It is clearly visible that the nominal sample has its main lattice relaxation at lattice parameters around 5.46 Å whereas for the patterned part, the lattice-parameters are streched over a longer area in reciprocal space, showing a maximum at about 5.51 Å.

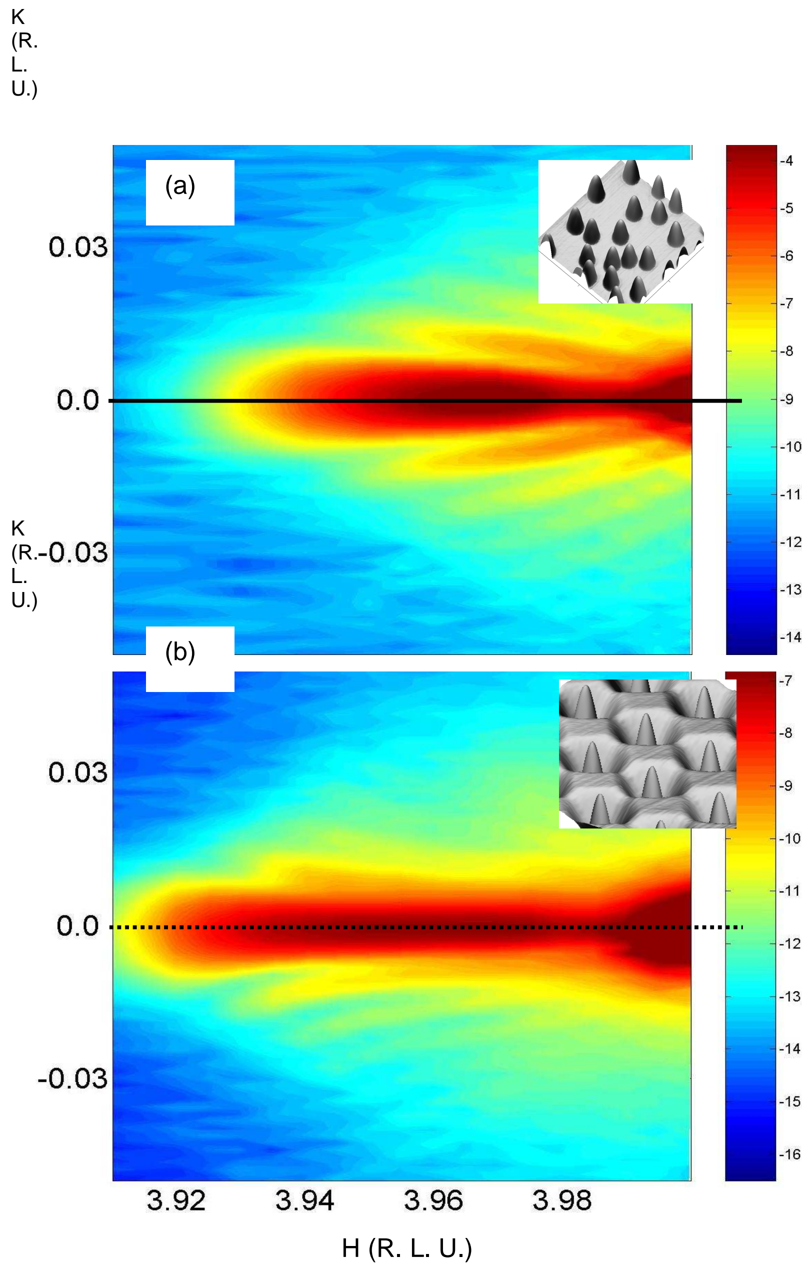

FIG. 1: (a) Reciprocal space map around the 400 Bragg reflection for the SK-grown sample on the nominal part. (b) The same region of reciprocal space shown in (a) but for the Ge-islands grown on the patterned part.

To better understand the reported difference, we related the lattice-parameter results to the local Ge content inside the islands by exploiting anomalous x-ray scattering. We recall that by monitoring the variation of the scattered intensity when varying the x-ray energy in the vicinity of the Ge K-edge (E_e=11.103 keV) at a fixed momentum tranfer Q, the corresponding average Ge concentration can be determined, so that lattice parameter vs Ge content (c) data are extracted, basically without any model assumption. A first key result came out: both for the nominal and for the pit-patterned region, the average Ge content turned out to be ~60% in both cases: the presence of the pit does not influence neither the shape (dome) nor the relative amount of Si and Ge atoms within the island. Let us see where, instead, differences exist. Figure 2 (b) shows Ge-concentration vs. the in-plane lattice parameter $a_{||}$ for the nominal (full lines) and the patterned region (dashed lines). A qualitative observation can be immediately made. By assuming the usual base-to-top lattice relaxation within islands, the flatness of the dashed curve indicates more uniform alloying within the pits in comparison to the nominal case. A possible explanation of this different behavior will be given after completing the presentation of the results. More insights can indeed be gained by extracting the actual 3D Ge distribution and the elastic-energy profile. Over the last ten years, x-ray methods have been developed, coupling lattice parameter with lateral size and chemical composition of an object, reconstructing a concentration profile inside nanostructures. These methods are limited however by model assumptions concerning the shape of the considered iso-strain regions. Instead, we have used a novel fitting procedure exploiting a FEM-based treatment of non-uniform concentration profiles, allowing us to determine the local Ge content without any constraint. After the island and substrate geometry is created based on AFM images, non-uniform concentration values are assigned on a discrete mesh. The elastic problem is then solved exploiting linear interpolation, ($c,a_{||}$) data are extracted, and the statistical $\square^2$ is evaluated by comparison with the corresponding x-rays data. Using an iterative procedure based on local concentration exchanges preserving the assigned experimental average concentration value, $\square^2$ is minimized. It is important to emphasize that particular care is required in assigning the correct statistical weight to the data. During the fit, indeed, (c, $a_{||}$) pairs were computed not only from the island interior, but also from a surrounding region in the substrate with a lateral extension inferred from the experimental island density, and a depth of 12nm, i.e. the estimated penetration depth of the x-rays in our set-up. This allowed us to filter out from the experimental data the substrate contribution which, as shown in Fig. 2(c) for the nominal case, causes a sudden drop of the average Ge content at low lattice parameters, hiding important data coming from the island interior. Another difficulty stems in the vanishing experimental scattering volume (see Fig. 2(c)) of the regions with lattice parameter close to bulk Ge.

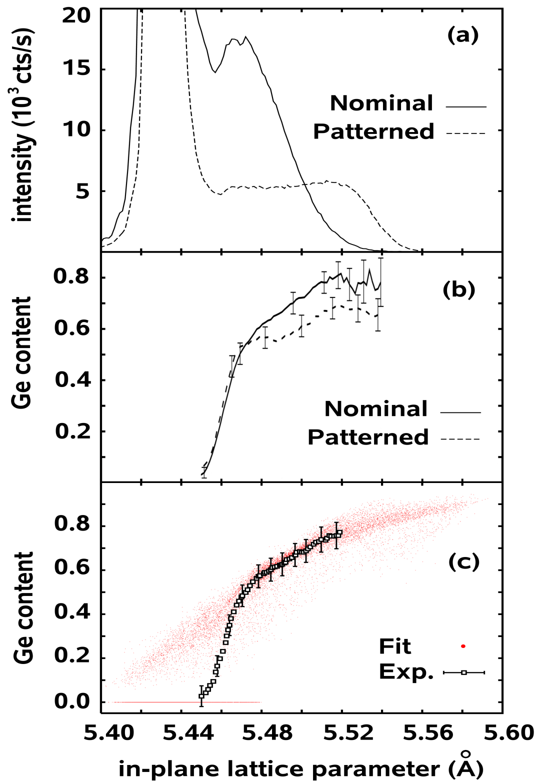

FIG. 2: (a) Radial intensity distribution as a function of lattice parameter for Ge-islands grown on the nominal part (full line) and on the prepartterned part (dashed line). (b) Germanium concentration inside the islands as a function of lattice parameter for growth on the nominal (full line) and on the patterned part (dashed line). (c) Experimental raw data, and fitted data after proper separation of the Si substrate contribution (nominal case).

In the fit their concentration value was extrapolated from experiments, assigning a large error bar in order not to bias the region where real data were present. Finally, a satisfactory fit (which required ≈10^4 iterations) is obtained, the full solution of the elastic problem being required at each step.

The 3D compositional maps for the nominal and the patterned substrate corresponding to our theoretical best fit are displayed in Fig. 3(a)-(d) together with their horizontally-averaged values (Fig. 3(e)), while the elastic energy per atom is reported in Fig. 3(f), where a comparison with the uniform composition case is also shown. In the nominal case - Fig. 3(a) and (b), an almost Si-pure region is found close to the base edges, a result fully compatible with selective-etching data. From Fig. 3(c) and (d) one sees that Si enrichment at the base is less evident in the pit case where the overall Ge distribution is more uniform, but for more localized irregularities. This is particularly evident from the horizontally averaged Ge content values displayed in Fig. 3(e). The above observations can be justified using both thermodynamic and kinetic arguments. The edges of the islands grown on flat substrates are the most compressed regions in case a uniform Ge distribution is considered, so that replacing Ge with smaller Si atoms produces significant relaxation. By comparing the energy per atom in flat vs. pit-patterned substrates (Fig. 3(f)) in the case of a uniform distribution, one sees that the driving force for Si segregation at the island base is weaker in pits, since the elastic-energy difference between base and top is smaller.

If pit pre-patterning is already seen as a powerful tool to control positioning and homogeneity of heteroepitaxial islands, in this Letter we have shown that it also allows one to control elastic-energy release. This opens up the possibility of tuning strain in the islands by selecting the shape of the pits in order to grow islands with the desired degree of relaxation. The kinetics of Si supply, however, seems to be also influenced by the presence of the pit, calling for further investigations for achieving full control.

FIG. 3: Cross-section map of the 3D-reconstructed Ge content profile for islands grown on nominal (a-b) and patterned (cd) samples. Sections are showed along the [100] (a,c) and the [110] (b,d) crystallographic directions. Islands lateral size is shown in nm. Panel (e) displays the average Ge content as a function of height. Panel (f) reports for the elastic energy profile correspoding to the fitted Ge distribution on flat (filled box) and patterned (empty box) substrates. Plots made for the case of uniform concentration are analogously displayed for flat (filled triangles) and pit (empty triangles) case.

- First stage of Fe growth on Pt(100)-hex reconstruction: seeking for chemically ordered FePt nanostructures (32-03-686)

and

- Growth, structure and magnetic properties of ultra-thin MnPt/FePt exchange-coupled bilayers on Pt(100). (32-03-684)

Marcio Soares, Maurizio De Santis, Helio Tolentino, Aline Ramos.

MCMF, Institut Néel, CNRS & UJF - BP166, 25 av. des Martyrs, 38042 Grenoble Cedex 9, France.

The overall scientific scope of our study is the understanding of the interaction between antiferromagnetic (AFM) and ferromagnetic (FM) materials at well-defined interfaces by combining structural, electronic and magnetic techniques using synchrotron light. We are particularly interested on the growth and structural properties of AFM layers (MnPt and CoO) exchanged coupled to a thin FM FePt film with perpendicular magnetic anisotropy (PMA) grown on Pt(001) single crystal.

Spin valve systems based on the exchange interaction between AFM and FM layers are widely investigated for their application in the future generations of magnetic heads for high-density hard-disk drives. The desired properties of the AFM are large exchange coupling, good resistance to corrosion and good thermal stability. One of the most interesting materials for such a kind of applications is MnPt [1]. This alloy displays better properties compared to most AFM materials in the ordered $L1_0$ phase (T_N ~ 900 K) [2] but it is non-magnetic in the fcc disordered phase. High exchange bias and thermal stability are difficult to maintain when reducing the thickness. It was shown that exchange coupling disappears in spin valves when the MnPt AF layer is thinner than 6-10 nm [3]. The origin of this critical thickness is controversial. It has been suggested that the critical thickness is that where the AFM becomes thermally unstable, owing to the finite-sized scaling of the Néel temperature (T_N) [4]. An alternative explanation relates the lack of exchange coupling with the fact that thin films are not chemically ordered [5], and hence not AFM. With few exceptions, all these studies were performed on polycrystalline films grown by sputtering and showing different degrees of texture. Epitaxial growth by molecular beam epitaxy followed in situ by surface x-ray diffraction allows a better control of the conditions to obtain a tetragonal phase and helps to understand the link between exchange coupling and structure.

The magnetic properties of our system are studied thanks to the exchange bias. The first step in our experiment was the growth of the FM layer. Magnetic ultra-thin films grown on non-magnetic substrates present quite distinct structural and magnetic properties compared to bulk materials [6]. In the case of deposition of Fe on Pt(100), He et al.[7] reported that, in the low coverage regime, atomic exchange takes place and Fe is buried under a Pt top layer, even at RT. For thickness between 2 to 5 monolayers, annealing up to 600 K results in the formation of ordered FePt alloys presenting perpendicular magnetic anisotropy (PMA). A change from higher to lower PMA was observed at about 3.3 ML and was related to a phase transformation from tetragonal $L1_0$ to $L1_2$ FePt phases. However, this structural aspect deserves confirmation. Our recent LEED experiments, aided by Auger spectroscopy, give results diverging from these authors.

In the first part of our *in situ* surface X-ray diffraction experiment, hold in September 2009 at BM32, we studied the deposition of Fe on Pt(100). We observed that a single layer of Fe deposited at temperature of about 500 K, generates a bilayer with Pt segregating on top of Fe. A high-chemically

---

[1] J. P. Nozières et al., J. Appl. Phys. **87**, 3920 (2000).
[2] H.Hama et al. J.Phys.:Condens. Matter **19** (2007) 176228.
[3] M. Rickart et al., Eur. Phys. J. B 45, 207 (2005); T.Sato et al., JMMM **240** (2002) 277.
[4] T. Ambrose et al., J. Appl. Phys. 83, 6822 (1998).
[5] M. F. Toney et al., Appl. Phys. Lett. **81**, 4565 (2002).
[6] C.A.F. Vaz, J.A.C. Bland and G. Lauhoff, *Rep. Prog. Phys.* **71** (2008), 056501
[7] K. He, L.J. Zhang, X.C. Ma, J.F. Jia Q.K. Xue, and Z.Q. Qiu, *Phys. Rev. B* **72** (2005) 155432.

ordered $L1_0$ phase was then obtained by alternated deposition of Fe and Pt monoatomic layers (ML) at a substrate temperature of about 570 K. Fig.1 shows the (1 1) rod (indexed taking a tetragonal surface cell with $a=a_{Pt}/\sqrt{2}$) of the film obtained after deposition of 12 ML (6 ML of each kind of atom), compared with the substrate rod. The film is pseudomorphic and a high degree of order is obtained, as shown by the strong superstructure peak in between the fundamental Bragg reflections of the fcc lattice. The film shows a shorter c lattice parameter with respect to the $L1_0$ bulk phase.

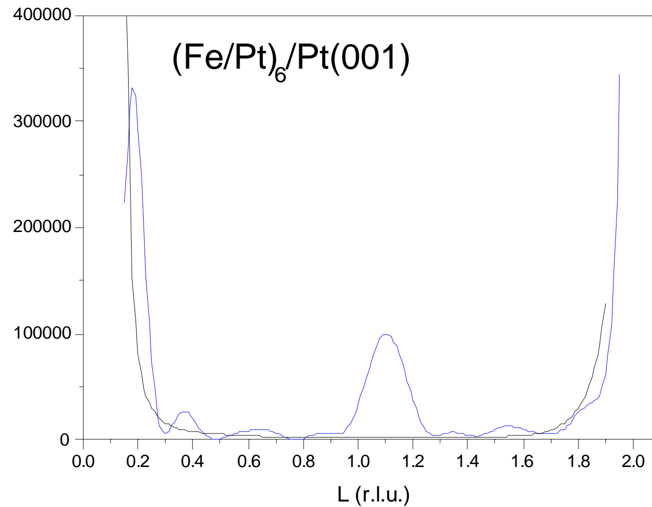

Fig.1: (1 1) rod of a film of 12 ML of PtFe on Pt(100) grown by alternated deposition of 1 ML of each kind of atoms at about 570 K (blue curve). The substrate rod is also shown.

No traces of $L1_2$ FePt phase were found. Such a FePt(001) surface layer is flat with large terraces and can be used as a starting point to study the growth of a CoO or MnPt layer directly on a FM surface. The proximity to a FM layer with PMA can play an important role in the spin orientation of the AFM layer.

In the second part of the experiment we started growing the PtMn alloy on Pt(100). In this case the ordered phase can be obtained in quite a narrow temperature range. We had already studied MnPt/Pt(100) films in the nanometric thickness range obtained by alternate Mn and Pt deposition, to mimic the chemical order of the FePt(001) alloy. Such films deposited at room temperature show no chemical order. Nevertheless, after post annealing to 770 K for 1 hour a diffuse scattering appears, indicating short-range order and incipient $L1_0$ domains. These $L1_0$ domains turned out to be oriented both out-of-plane and in-plane, with coherence lengths of about 1.6 nm.

In the actual experiment we succeeded in growing an ultra-thin layer of MnPt with $L1_0$ phase. The film was grown by alternate monoatomic deposition of Mn and Pt at about 570 K.

It was possible to follow at each step of the growing the evolution of ordering peak. This is shown in figure 1, where the scattered intensity along the (1 1) rod is plotted.

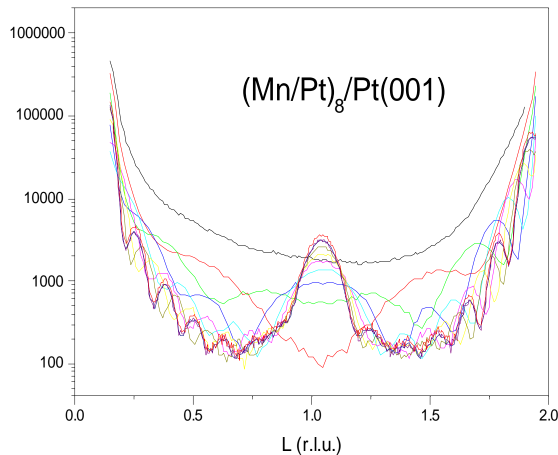

Fig.2: (1 1) rod measured at each step of the alternated atomic layer deposition of Mn and Pt on Pt(100) at about 570 K.

Fig.3. RT MOKE of $Pt_8/(Fe/Pt)_4(Mn/Pt)_8/Pt(100)$

One can observe a clear development of the order peak as the number of layers is increasing. The growth was stopped when 8 Mn/Pt bilayers were completed. The structure of this layer was studied by exploring the truncation rods in the reciprocal space for many reflections. After that a FePt film was deposited on top of the MnPt film. The FePt was composed of 4 Fe/Pt bilayers. The sample was covered by 8 ML of Pt for ex situ studies. Before taking the sample out, a complete structural study was performed in the whole film.

The room temperature perpendicular magnetic anisotropy associated to this sample has already been measured by ex-situ MOKE experiments (Fig. 3). The coercivity is found much smaller than for a typical FePt ordered thick layer. This could come either from the degree of order or from the thickness effect on the Curie temperature, which could impose an order below room temperature. Low temperature measurements are planned to study the magnetic properties of the MnPt layer and the exchange coupling.

The structural analysis to refine all the parameters for FePt, MnPt, and FePt/MnPt films is in progress.

Instrumental refurbishment project for 2008/2009 : New BM32 hutch and integration of a CBE gas injection system

The refurbishment project, supported by the RTRA « **Nanosciences aux limites de la nanoélectronique »** has made important progress in 2008/9. The new hutch has been built during a 6 months closure of the instrument, and a new sample preparation lab is now situated in close neighbourhood of the instrument. The integration of the gas injection system to combine solid source and gas source MBE has been ordered and will be supplied by the company VEGATEC in Winter 2009/2010.

Sketches of the new experimental hutch and the integration of the gas injection system:

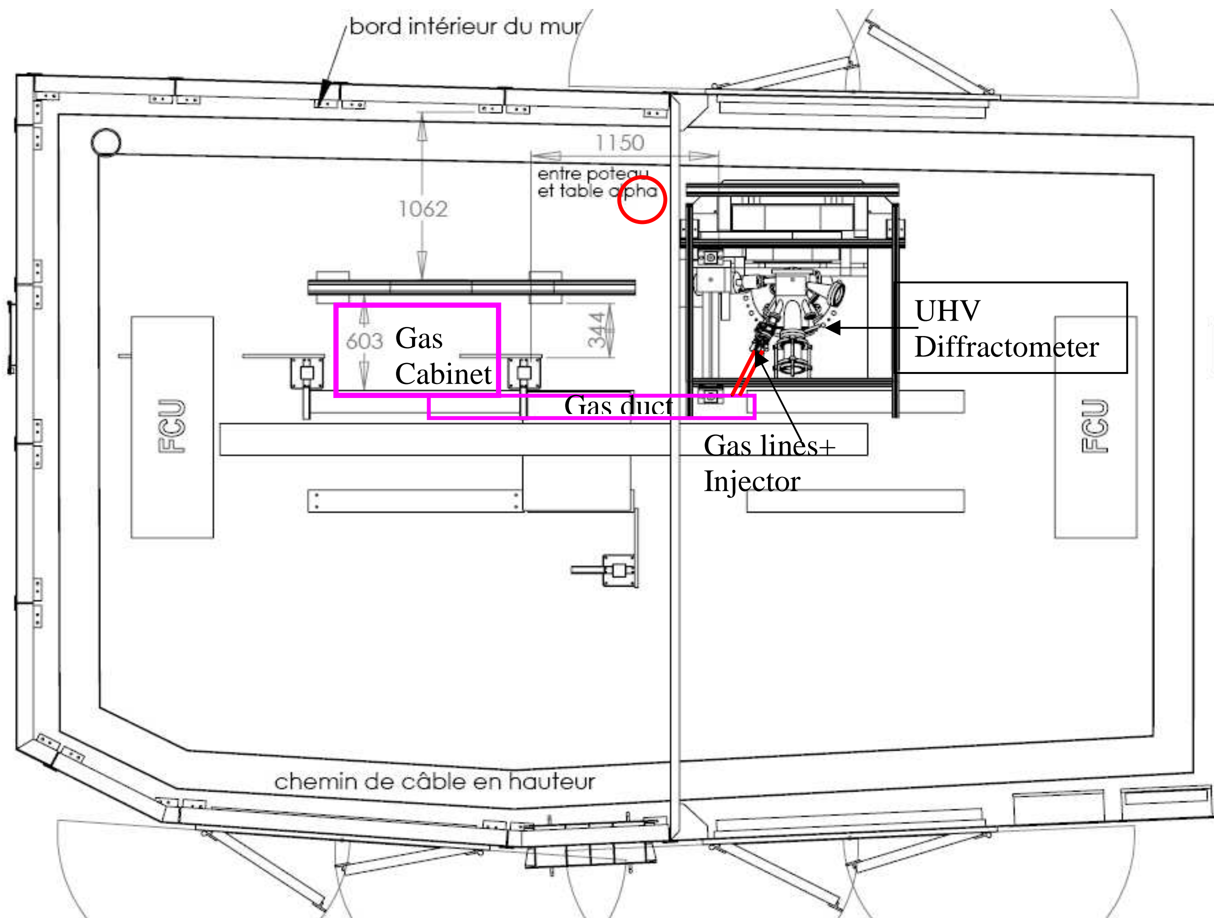

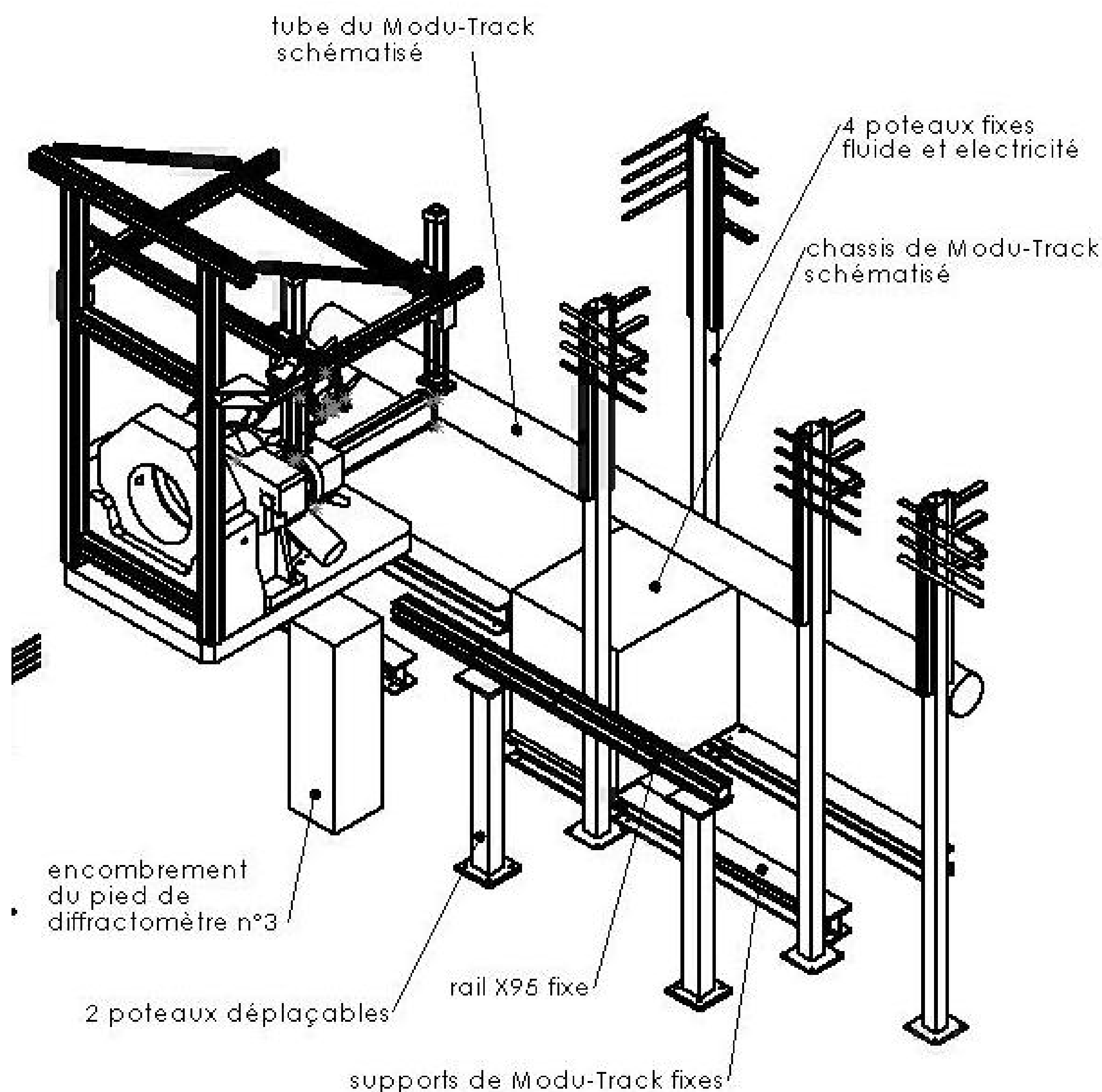

Sketch of the gas injection system with a technical representation of one of the four equivalent gas-distribution lines.

Marked in red are the parts already present on site: extraction, primary vacuum, CBE injector. The connection of the primary pump to the extraction as well as the N_2 flux at the exit of the primary pump has to be realized by the supplier of the gas cabinet, as well as the connection of the gas cabinet to the extraction (present on the ceiling of the experimental hutch).

Exhaust

Extraction (ATEX level)

Detection of air flux

D

I-4

N_2 Flux

Gas and Fire Detectors

Prrimary pump

P-26

Automatic safety pilot with pressure readouts, detectors output.
Controls valves, pumps, safety outputs.

Turbomolecular pump

M

Double walled line

P-29

UHV growth chamber

V2

V1

V5

F1

V3

V4

Vent-line from injector

P-25

GeH_4 open air detector

Turbomolecular pump

V1: bottle valve (Pinhole)
V2: pneumatic pressure reducing valve
V3-V5: pneumatic valves
F1: flow element

As a guide to the eye: location of the gas injector on the UHV-chamber:

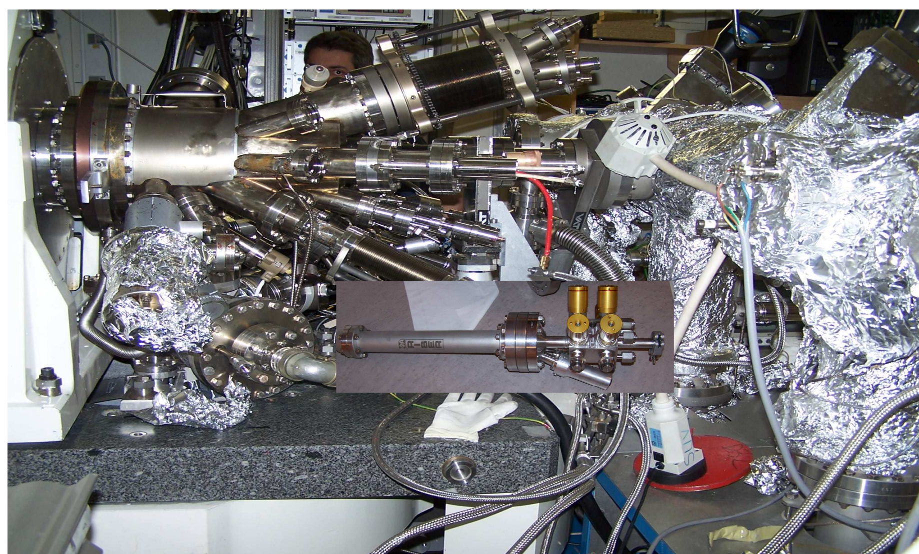

Liste des publications résultant de mesures sur la ligne IF publiés en 2007-2009 :

( ) : nombre de citation au 15 Octobre 2009 [ ] : facteur d'impact (selon web of science)

2009

Publications:

[12.8] "*Probing surface and interface morphology with Grazing Incidence Small Angle X-Ray Scattering* "
G. RENAUD, R. LAZZARI AND F. LEROY,
Surf. Sci. Rep. **64** (2009) pp. 255-380,

[7.18] "*Enhanced Relaxation and Intermixing in Ge Islands Grown on Pit-Patterned Si(001) Substrates* "
T. U. SCHÜLLI, G. VASTOLA, M.-I. RICHARD, A. MALACHIAS, G. RENAUD, F. UHLIK, F. MONTALENTI, G. CHEN, L. MIGLIO, F. SCHÄFFLER, G. BAUER,
Phys. Rev. Lett. **102**, 025502 (2009).

[3.73] "*Multiple scattering effects in strain and composition analysis of nanoislands by grazing incidence x-rays."*
M.-I. RICHARD, V. FAVRE-NICOLIN, G. RENAUD, T. SCHÜLLI, C. PRIESTER, Z. ZHONG, AND T.-H. METZGER
Appl. Phys. Lett. **94**, 013112 (2009).

[3.73] "X-ray measurements of the strain and shape of dielectric/metallic wrap-gated InAs nanowires"
J. EYMERY, V. FAVRE-NICOLIN, L. FROBERG, L. SAMUELSON
Appl. Phys. Lett. **94** 131911 (2009)

[3.73] « *A model of interface defect formation in silicon wafer bonding* »
S. VINCENT, I. RADU, D. LANDRU, F. LETERTRE, F. RIEUTORD
Appl. Phys. Lett. **94** (10) 101914 (2009)

[3.32] „*In situ x-ray scattering study on the evolution of Ge island morphology and relaxation for low growth rate: advanced transition to superdomes*
M.-I. RICHARD, T. U. SCHÜLLI, G. RENAUD, E. WINTERSBERGER, G. CHEN, G. BAUER, V. HOLY,
Phys. Rev. B 80, 045313 (2009).

[3.32] "*Defect-pinned nucleation, growth and dynamic coalescence of Ag islands on MgO(001): An in situ grazing-incidence small-angle x-ray scattering study*"
C. REVENANT, G. RENAUD, R. LAZZARI AND J. JUPILLE,
Phys. Rev. B **79**, 235424 (2009).

[3.32] «Adhesion of growing nanoparticles at a glance: Surface differential reflectivity spectroscopy and grazing incidence small angle x-ray scattering »
R. LAZZARI, G. RENAUD, C. REVENANT, J. JUPILLE, AND Y. BORENSZTEIN,
Phys. Rev. B **79**, 125428 (2009).

[2.44] "*Prebonding Thermal Treatment in Direct Si-Si Hydrophilic Wafer Bonding"*
C. VENTOSA, F. RIEUTORD, L. LIBRALESSO, F. FOURNEL, C. MORALES, H. MORICEAU, H
J. Electrochem. Soc. **156** (11) H818 (2009)

[2.20] "Elastic relaxation in patterned and implanted strained silicon on insulator"
S. BAUDOT, F. ANDRIEU, F. RIEUTORD, J. EYMERY
J. Appl. Phys. **105** (11) 114302 (2009)

[2.01] "Mechanism of Thermal Silicon Oxide Direct Wafer Bonding"

C. VENTOSA, C. MORALES, L. LIBRALESSO, F. FOURNEL, A.M. PAPON, D. LAFOND, H. MORICEAU, J.D. PENOT, F. RIEUTORD,
Electrochem. Solid State Lett. **12** (10) H373 (2009)

[0.69] "*Structural properties of Ge/Si(001) nano-islands by diffraction anomalous fine structure and multiwavelength anomalous diffraction* "
M.-I. RICHARD, N.A. KATCH, M.G. PROIETTI, H. RENEVIER, V. FAVRE-NICOLIN, Z. ZHONG, G. CHEN, M. STOFFEL, O. SCHMIDT, G. RENAUD, T.U. SCHÜLLI, AND G. BAUER,
Eur. Phys. J. Special Topics **167**, 3 (2009).

[0.69] "*Real-time icosahedral to fcc structure transition during CoPt nanoparticles formation*",
Penuelas J, Andreazza P, Andreazza-Vignolle C, Mottet C, De Santis M, Tolentino HCN. EUROPEAN PHYSICAL JOURNAL-SPECIAL TOPICS Volume: 167 Pages: 19-25, Feb. 2009

[0.51] *"Structure, morphology and magnetism of an ultra-thin [NiO/CoO]/PtCo bilayer with perpendicular exchange bias "*,
Helio C. N. Tolentino, Maurizio De Santis, Jean-Marc Tonnerre, Aline Y. Ramos, Veronique Langlais, Stephane Grenier, and Aude Bailly, Brazilian Journal of Physics, vol. 39, no. 1A, April, 2009

T. Charitat, S. Lecuyer, G. Fragneto,F*luctuations and destabilization of single phospholipid bilayers*, Biointerphases 3, Issue 2, pp. 3-15 (2008).

[31] *"Substrate enhanced supercooling in AuSi eutectic droplets",*
T. U. Schülli, R. Daudin, G. Renaud, A. Vaysset, O. Geaymond, A. Pasturel,
submitted to Nature, (October 2009)

C. Kirchlechner , D. Kiener , C. Motz, N. Vaxelaire, O. Perroud, J.-S. Micha, O.Ulrich, O. Thomas, G. Dehm, J. Keckes
submitted to Phil. Mag. "special edition"

L. Malaquin et al. "Supported bilayers: combined specular and diffuse x-ray scattering"
submitted to Eur. Phys. J. E
cond-matt http://arxiv.org/abs/0910.1275

Prix

J. Villanova
"Young scientist award", symposium R , E-MRS Strasbourg 2009

C.Ventosa
"Best student paper prize" ElectroChemical Society International Conference, Hawaii USA (Oct08).

R.Daudin
prix master de la SF2M Octobre 2009

Communications orales/ conférences invitées

«X-ray Microdiffraction on a single-crystalline copper micro-tensile sample »
C. KIRCHLECHNER, D. KIENER, C. MOTZ, N. VAXELAIRE, J.S. MICHA, O. ULRICH, O. THOMAS, J. KECKES, G. DEHM
EUROMAT 2009

" Residual stresses in SOFC"
J. VILLANOVA, O. SICARDY, R. FORTUNIER, J.-S. MICHA, C. MAURICE, P. BLEUET
International Fuel Cell Conference Lucern, Switzerland 29th June – 2nd July 2009

“Determination of global and local residual stresses in SOFC by X-ray diffraction”
J. VILLANOVA, O. SICARDY, R. FORTUNIER, J.-S. MICHA, P. BLEUET
spring E-MRS Strasbourg, France, 9-11th June 2009
à paraitre dans Nucl. Inst. Meth. B

" Towards synchrotron-based nanocharacterization "
P. Bleuet, L. Arnaud, X. Biquard, P. Cloetens, L. Doyen, P. Gergaud, P. Lamontagne, M. Lavayssière, J.-S. Micha, O. Renault, F. Rieutord, J. Susini, O. Ulrich
Proceeding of International Conference on Frontiers of Characterization and Metrology for Nanoelectronics (Albany, NY, 11-14th may 2009)
AIP Conf. Proc. 1173, 181 (2009)

Meeting of the French Crystallographic Association AFC in Rennes, France. Title: “Relaxation and Intermixing Behavior in SiGe Islands Grown on Prepatterned Si(001)”
T. Schülli et al.

X-top 2008, Linz, Austria: Enhanced Relaxation and Intermixing in Ge Islands Grown on Pit-Patterned Si(001) Substrates
T. Schülli et al.

Joint annual meeting of the Austrian and Swiss Physical Societies in Innsbruck, Austria. Title: “X-ray light on SiGe islands and new growth methods – results and challenges for in situ studies of nanostructures”
T. Schülli et al.

GISAS 2009 in Hamburg, Germany. Title: *“Investigation of the growth of Ge islands on nominal and patterned Si(001) substrates”*
T. Schülli et al.

“*Evolution of the composition and relaxation of Ge(Si) islands during their growth on nominal and patterned Si(001) substrates by in situ X-ray anomalous scattering*”
3S’09 (International Symposium on the Structure of Surfaces, 2009), St Moritz, 8-14 March 2009
G. Renaud et al.

« *Etudes in situ de la croissance de germanium sur silicium par diffusion des rayons X synchrotron en incidence rasante* ».
INSP (Institut des NanoSciences de Paris), March 26, 2009
G. Renaud et al.

J. Eymery et al "Embedded Buried Nitride" Technique. Accepted in ECS 2009 proceedings. 24-29 May 2009 - San Francisco-United States.

S. Baudot, J. Eymery , F. Andrieu, V. Vidal, F. Allain, L. Brévard, O. Faynot, Width and orientation effects in strained FDSOI MOSFETs: strain and device characterization. Accepted in ESSDERC 2009 proceedings. 14-18 September 2009 - Athens- Greece.

Study of Fluctuations and Destabilization of Single Phospholipidic Bilayer by Neutron and X-ray Scattering, 54th American Vacuum Society Meeting, Seattle, 14-19 Octobre 2007

Neutron and X-ray scattering to investigate supported bilayer's physical properties, Biological Physics at Large Facilities, Grenoble, 19-23 Octobre 2008

Fluctuations and Destabilization of a single bilayer, FNRS, Groupe de Contact Rayonnement Synchrotron, Bruxelles, 12 Décembre 2008

PhD-thesis – Habilitation à Diriger des Recherches

C. Ventosa "Etude des mécanismes mis en jeu dans le collage par adhésion moléculaire de surfaces hydrophiles " UJF 02/10/2009

S. Vincent "Etude du collage par adhesion moléculaire entrant dans le cadre de la réalisation de substrats composites par la technologie Smart-Cut™" INPG 25/09/2009

F. Fournel (HDR) "Le collage moléculaire et ses applications" UJF 14/09/2009

L. Malaquin "Interactions et destabilisation de membranes lipidiques supportées" 28/10/2009 Université de Stasbourg

P. Bleuet (HDR) "*X-Ray Nanoprobe*", soutenance prévue le 4 Décembre 2009

2008

Publications:

(13) [28,1] *"Shape Changes of Supported Rh Nanoparticles During Oxidation and Reduction Cycles"*,
P. NOLTE, A. STIERLE, N. Y. JIN-PHILLIPP, N. KASPER, T. U. SCHULLI, H. DOSCH,
Science **321**, 1654 (2008)

(4) [7,18] *"Depth Magnetization Profile of a Perpendicular Exchange Coupled System by Soft X-ray Resonant Magnetic Reflectivity",*
J. M. TONNERRE, M. DE SANTIS, S. GRENIER, H.C.N. TOLENTINO, V. LANGLAIS, E. BONTEMPI, M. GARCIA-FERNANDEZ, AND U. STAUB
Phys. Rev. Lett. **100**, 157202 (2008)

(4) [7,18] "*Controlling structure and morphology of CoPt nanoparticles through dynamical or static coalescence effects",*
J. PENUELAS, P. ANDREAZZA, C. ANDREAZZA-VIGNOLLE, H.C.N. TOLENTINO, M. DE SANTIS, AND C. MOTTET
Phys. Rev. Lett. **100**, 115502 (2008)

[3.73] "*Germanium oxynitride (GeOxNy) as a back interface passivation layer for Germanium-on-insulator substrates"*
T. SIGNAMARCHEIX, F. ALLIBERT, F. LETERTRE, T. CHEVOLLEAU, L. SANCHEZ, E. AUGENDRE, C. DEGUET, H. MORICEAU, L. CLAVELIER, F. RIEUTORD
Appl. Phys. Lett. **93**(2), 022109 (2008)

(7) [3.73] *"Spontaneous compliance of the InP/$SrTiO_3$ heterointerface"*
G. SAINT-GIRONS, C. PRIESTER, P. REGRENY, G. PATRIARCHE, L. LARGEAU, V. FAVRE-NICOLIN, G. XU, Y. ROBACH, M. GENDRY, GUY HOLLINGER
Appl. Phys. Lett. **92**, 241907 (2008)

[3.32*] «Structure and morphology of thin MgO films on Mo(001) «*
S. BENEDETTI, P. TORELLI, S. VALERI, H.M. BENIA, N. NILIUS, G. RENAUD
Phys. Rev. B **78**, 195411 (2008).

(4) [3.32] *"Kink ordering and organized growth of Co clusters on a stepped Au(111) surface: A combined GISAXS, GIXD and STM study"*
F. LEROY, G. RENAUD, A. LETOUBLON, A. ROHART, Y. GIRARD, V. REPAIN, S. ROUSSET, A. COATTI, Y. GARREAU

Phys. Rev. B **77**, 045430 (2008)

(2)[3.32] *"Growth of Co on Au(111) studied by multiwavelength anomalous grazing-incidence small-angle x-ray scattering: From ordered nanostructures to percolated thin films and nanopillars"*
F. LEROY, G. RENAUD, A. LETOUBLON, R. LAZZARI,
Phys. Rev. B **77**, 235429 (2008).

(2) [3.32] *"Self-organized growth of Ni clusters on a cobalt-oxide thin film induced by a buried misfit dislocation network"*
P. TORELLI, E.A. SOARES, G. RENAUD, L. GRAGNANIELLO, S. VALERI, X. GUO AND P. LUCHES,
Phys. Rev. B **77**, 081409(R) (2008)

[2,20] "Hydrophilic low temperature direct wafer bonding"
(3) C. VENTOSA, F. RIEUTORD, L. LIBRALESSO, C. MORALES, F. FOURNEL, H. MORICEAU,
J. Appl. Phys. **104** 123524 (2008)

[2,00] « Looking by grazing incidence small angle x-ray scattering at gold nanoparticles supported on rutile TiO2(110) during CO oxidation »
M.C. SAINT-LAGER, A. BAILLY, M. MANTILLA, S. GARAUDEE, R. LAZZARI, P. DOLLE, O. ROBACH, J. JUPILLE, I. LAOUFI, P. TAUNIER
Gold Bulletin **41**, 159 (2008)

(2) [1.9] *"Effects of thermal annealing on C/FePt granular multilayers: in situ and ex situ studies"*
D. BABONNEAU, G. ABADIAS, J. TOUDERT, T. GIRARDEAU, E. FONDA, J.-S. MICHA and F. PETROFF,
J. Phys : Cond. Mat. **20**, 035218 (2008)

(1) [1.73] *"Coalescence of domes and superdomes at a low growth rate or during annealing: Towards the formation of flat-top superdomes"*
M.-I. RICHARD, G. CHEN, T.U. SCHÜLLI, G. RENAUD, G. BAUER,
Surf Sci. **602**, 2157 (2008).

(2) [1.73] *"Structural investigation of silicon nanowires using GIXD and GISAXS: Evidence of complex saw-tooth faceting"*
T. DAVID, D. BUTTARD, T. SCHÜLLI, F. DALLHUIN, P. GENTILE
Surf. Sci **602**, 2675 (2008).

[1.58] *"Real time investigation of the growth ofsilicon carbide nanocrystals on Si(100) using synchrotron X-ray diffraction"*
S. MILITA, M. DE SANTIS, D. JONES, A. PARISINI, V. PALERMO,
Applied Surface Science **254**(7), 2162 (2008)

Book Chapters :

-"Chapter 10: Nanostructures in the light of synchrotron radiation: Surface sensitive x-ray techniques and anomalous scattering"
T. METZGER, V. FAVRE-NICOLIN, G. RENAUD, H. RENEVIER, T. SCHÜLLI
Chapitre de livre: « Characterization of Semiconductor Heterostructures and Nanostructures »
Edited by C. Lamberti, Elsevier 2008, p 361-403

PhD-thesis

M. I. Richard « "The growth of Ge islands on nominal and pre-patterned Si(001) surfaces: in situ and ex situ X-ray studies" Univ. Joseph Fourier, December 14, 2007.

B. Mallard (soutenance en attente) ILL-ENSAM (Metz) « Alliage CuBeAl à mémoire de forme »

Vincent Consonni « Mécanismes de structuration et de dopage au chlore dans le CdTe polycristallin. » 22 Octobre 2008
l'Institut polytechnique de Grenoble, spécialité Matériaux, Mécanique, Génie Civil, Electrochimie

Michel Eberlein « Contraintes locales induites par le procédé 'Shallow Trench Isolation' : Diffraction X haute résolution et simulation par éléments finis » 24 janvier 2008, Université Paul Cézanne, Marseille

Delphine Borivent « Interdiffusion réactive dans le système Ni-Si. » Physique et Sciences de la Matière, Université Paul Cézanne, Marseille
24 Juin 2008

Conférences :

- «*Monitoring growing nanoparticles with in Situ GISAXS and GIXD* »
  Catalysis workshop » ESRF Users's meeting 2008 Grenoble, Tuesday 5 February 2008
  G. Renaud et al.
- « *Relaxation and Intermixing of Ge Islands on nominal and pit-patterned Si(001) surfaces from kinetics to equilibrium thermodynamics* »
  ICSOS9 Brésil (International Conference on the Structure of Surfaces, Salvador, Août 2008, Brésil)
  G. Renaud et al.
- « *Evolution of the composition of Ge islands during their growth on Si(001) by in situ grazing incidence x-ray anomalous scattering*"
  ICSOS9 Brésil (International Conference on the Structure of Surfaces, Salvador, Août 2008, Brésil)
  G. Renaud et al.
- « *Combined in situ GISAXS and GIXD study of the growth of Ge islands on nominal and patterned Si(001) surfaces*"
  MRS Fall meeting 2008, Boston
  G. Renaud et al.
- « *Diffraction de surface: un aperçu* »
  3ième Ecole Française de Réflectivité, SAXS, GISAXS et Diffraction de Surface Giens, Mai 2008
  G. Renaud et al.
- « *Structure et morphologie des nano-objets par diffusion/diffraction des rayons X en incidence rasante*
  GISAXS / GIXD (/ EXAFS) »
  Cours : Ecole thématique CNRS « Nano-Objets », Villeneuve D'Ascq, 3-6 nov. 2008
  G. Renaud et al.
- « *The growth of nanoparticle on surfaces, organized or not, investigated by in situ GISAXS and GIXD in UHV* «
  Exposé invité au Institut für Hableiter-und Festkörperphysik de Johannes Kepler Universitât Linz, Austria, Décembre 2008.
  G. Renaud et al.

2007

Publications:

(13) [10,37] "Strain and shape of epitaxial InAs/InP nanowire superlattice measured by grazing incidence X-ray techniques"
J. EYMERY, F. RIEUTORD, V. FAVRE-NICOLIN, O. ROBACH, L. FRÖBERG, T. MÅRTENSSON, and L. SAMUELSON
Nano Letters **7** (2007) 2596–2601.

[4,10] “Unexpected stability of phospholipid langmuir monolayers deposited on triton X-100 aqueous solutions”
P. FONTAINE, M.C. FAURE, F. MULLER, M. POUJADE, J.S. MICHA, F. RIEUTORD, M. GOLDMANN
Langmuir **23**(26), 12959 (2007)

(9) [3.73] "Strain field in silicon on insulator lines using high resolution x-ray diffraction »
GAILHANOU M, LOUBENS A, MICHA JS, CHARLET B., MINKEVICH AA, FORTUNIER R., THOMAS O.
Appl. Phys. Lett. **90** (2007) 111914

(8) [3.32] « Self-similarity during growth of the Au/TiO2(110) model catalyst as seen by the scattering of x-rays at grazing-angle incidence “
R. LAZZARI, G. RENAUD, J. JUPILLE, AND F. LEROY
Phys. Rev. **B 76** (2007) 125412

(6) [3.32] “Grazing-incidence small-angle x-ray scattering from dense packing of islands on surfaces: Development of distorted wave Born approximation and correlation between particle sizes and spacing “
R. LAZZARI, F. LEROY, AND G. RENAUD
Phys. Rev. **B 76** (2007) 125411

(8) [3.32] “Size and temperature dependent epitaxy for a strong filmsubstrate mismatch : the case of Pt/MgO(001)”
J. OLANDER, R. LAZZARI, J. JUPILLE, B. MANGILI, J. GONIAKOWSKI, G. RENAUD
Phys. Rev. **B 76** (2007) 075409

(6) [3.32] "Inversion of the diffraction pattern from an inhomogeneously strained crystal using an iterative algorithm »
MINKEVICH AA, GAILHANOU M, MICHA JS, CHARLET B., CHAMARD V., THOMAS O.
Phys. Rev. **B 76** (2007) 104106

(1) [3.32] "*Structure and magnetic properties of Mn/Pt(110)-(1x2): a joint x-ray diffraction and theoretical study”*
M. DE SANTIS, Y. GAUTHIER, H. C. N. TOLENTINO, G. BIHLMAYER, S. BLÜGEL, V. LANGLAIS,
Phys. Rev. B **75**, 205432 (2007)

(1) [3.32] *"Role of hydrogen interaction in two-dimensional molecular packing with strong molecule-substrate bonding"*
V. LANGLAIS, X. TORRELLES, Y. GAUTHIER, M. DE SANTIS,
Phys. Rev. B **76**, 035433 (2007).

(0) [2.20] “Quantitative study of hydrogen-implantation-induced cavities in silicon by grazing incidence small angle x-ray scattering »
L. CAPELLO, F. RIEUTORD, A. TAUZIN, F. MAZEN
J. Appl. Phys. **102** (2007) 026106

(7) [1.73] “X-ray scattering from stepped and kinked surfaces: An approach with the paracrystal model »
LEROY F, LAZZARI R, RENAUD G
Surf. Sci. **601** (2007) 1915-1929

(4) [1.73] “Nanostructuration of a CoO film by misfit dislocations”
P. TORELLI, E. A. SOARES, G. RENAUD, S. VALERI, X. X. GUO AND P. LUCHES
Surf. Sci. **601** (2007) 2651-2655

(6) [1.73] “Structural and morphological evolution of Co on faceted Pt/W(111) surface upon thermal annealing”
C. REVENANT, F. LEROY, G. RENAUD, R. LAZZARI, A. LETOUBLON, T. MADEY
Surf. Sci. **601** (2007) 3431

(0) [1.73] *"Chlorine chemisorption on Cu(001) by surface X-ray diffraction: Geometry and substrate relaxation"*
H. C. N. TOLENTINO, M. DE SANTIS, Y. GAUTHIER, V. LANGLAIS,
Surf. Science **601** (2007) 2962-2966

(0) [1.86] *"Surface structure and composition of the missing-row reconstruction of $VC_{0.8}$(110): A LEED, GIXRD and photoemission study"*
Y. GAUTHIER, I. ZASADA, M. DE SANTIS, V. LANGLAIS, C. VIROJANADARA,
Surf. Science **601** (2007) 3383-3394

(2) [1.74] "*New reactor dedicated to in operando studies of model catalysts by means of surface x-ray diffraction and grazing incidence small angle x-ray scattering*"
M.-C. SAINT-LAGER, A. BAILLY, P. DOLLE, R. BAUDOING-SAVOIS, P. TAUNIER, S. GARAUDÉE, S. CUCCARO, S. DOUILLET, O. GEAYMOND, G. PERROUX, O. TISSOT, J.-S. MICHA, O. ULRICH, and F. RIEUTORD
Rev. Sci. Instrum. **78** (2007) 083902

(1) [1.45] "*Water penetration mechanisms in nuclear glasses by X-ray and neutron reflectometry*"
REBISCOUL D, RIEUTORD F, NE F, FRUGIER P,CUBITT R, GIN S
J. Non Cryst. Solids **353** (2007) 2221-2230

(4) [1.21] "Investigation by High Resolution X-ray Diffraction of the local strains induced in Si by periodic arrays of oxide filled trenches »
EBERLEIN M, ESCOUBAS S, GAILHANOU M, THOMAS O., MICHA JS, ROHR P., COPPARD R.
Phys. Stat. Sol.**A 204** (2007) 2542-2547

(0) "*Structure of the 3C-SiC(100)-5x2 Surface Reconstruction Investigated by Synchrotron Radiation Based Grazing Incidence X-ray Diffraction*"
M. SILLY, H. ENRIQUEZ, J. ROY, M. D'ANGELO, P. SOUKIASSIAN, T. SCHÜLLI, M. NOBLET AND G. RENAUD
Mater. Sci. Forum **556-557**, 533 (2007).

ESRF Highlights:

ESRF Highlights 2007: "Determination of the complete stress state of sub-micrometric Cu grains by microdiffraction", p 77
O. SICARDY, X. BIQUARD, J.S. MICHA, F. RIEUTORD, O. ROBACH, O. ULRICH, O. GEAYMOND, V. CARREAU

ESRF Highlights 2007: "From now to then: real-time studies, nanoscale surface faceting", p 79
C. REVENANT, F. LEROY, G. RENAUD, R. LAZZARI, A. LETOUBLON, T. MADEY

INAC Bulletin 2007 : « Laue back at work at ESRF », J.S. MICHA *et al* , August 2008

Brevet:

L. Libralesso, C. Morales, H. Moriceau, F. Rieutord,
Brevet Traitement de surface par plasma d'azote dans un procédé de collage direct

Conférences invités:

“Strain determination in nanostructures via X-ray scattering measurements”
O. Thomas et al.
SizeDepEn Workshop Size-dependent materials behaviour: Challenges in miniaturisation and materials characterisation - March 15th -16th 2007, Fraunhofer Institut für Werkstoffmechanik Freiburg (Allemagne)

“Local strains in micro and nanostructures using synchrotron radiation”
O. Thomas et al.
ICMCTF 2007, International Conference on Metallurgical Coatings and Thin Films, April 23-27, 2007 San Diego, USA

“Diffraction analysis of elastic strains in micro- and nano-structures (keynote lecture)”
O. Thomas et al.
Size&Strain V 2007, "Diffraction analysis of the microstructure of materials", October 7-9 2007, Garmisch-Partenkirschen (Allemagne).

4 lectures on: Deducing strains and stresses from X-ray diffraction
Advanced synchrotron techniques and small dimensions
O. Thomas et al.
CISM - International Centre for Mechanical Sciences -Mechanical Size-Effects of Materials: Processing, Characterization and Modeling - Udine, May 12 - 16, 2008.

“ La diffraction des rayons X et la mécanique des nano-objets : état de l'art et perspectives » (Conférence semi-plenière)
O. Thomas et al.
11ème Journées de la Matière Condensée - Strasbourg août 2008

« Strain measurements at the nanoscale: micro-beam Laue scattering and coherent x-ray diffraction »
O. Thomas et al.
EPDIC 11, European Powder Diffraction Conference, Varsovie, 18 septembre 2008

« Local strains in micro and nanostructures using synchrotron radiation »
O. Thomas et al.
NANOSTRESS school, Cargese, 29 septembre - 5 octobre 2008

« X-ray structural studies of nanowires »
. J. Eymery
3SN'2008, Summer School on Semiconductor Nanowires, GDR Nanofils Nanotubes Semiconducteurs, june 15-20, 2008, Roscoff, France

,« Guided growth on templates – Use of strain
J. Eymery
Nanostress, Cargese Summer School, CNRS-Max Planck-Fraunhofer-Carnot, 29 Sept. – 5 Oct. 2008 »

“Structure and dynamic of DNA confined between non cationic lipid membranes”
L. Navailles, E. Andreoli de Oliveira, F. Nallet, E. Grelet, A. Fevrier & J. Dobrindt
2nd French Brazilian Polymer Meeting FBPOL2008, 20-25 April 2008, Florianòpolis, Brazil.

“ Organization of DNA fragments between lipid bilayers”
E. Andreoli de Oliveira, L. Navailles, , F. Nallet, E. Grelet, A. Fevrier & J. Dobrindt
Workshop of application of synchrontron radiation on soft matter, fev. 2008, LNLS- Campinas –Brasil

“Study of Fluctuation and Destabilization of Single Phospholipidic Bilayer by
Neutron and X-ray Scattering”
T. Charitat et al
54th AVS Meeting,
Seattle, 14-19 Octobre 2007

“Neutron and X-ray scattering to investigate supported bilayer's physical
Properties”
T. Charitat et al
Biological Physics at Large Facilities, 19-23 Grenoble, Octobre 2008